Development of a Triple GEM Detector for the LHCb Experiment

Dissertation

zur

Erlangung der naturwissenschaftlichen Doktorwürde
(Dr. sc. nat.)

vorgelegt der

Mathematisch-naturwissenschaftlichen Fakultät

der

Universität Zürich

von

Marcus Ziegler

aus

Deutschland

Begutachtet von

Prof. Dr. Ulrich Straumann
Prof. Dr. Fabio Sauli

Zürich 2002

Die vorliegende Arbeit wurde von der Mathematisch-naturwissenschaftlichen Fakultät der Universität Zürich auf Antrag von Prof. Dr. U. Straumann und Prof. Dr. Peter Truöl als Dissertation angenommen.

Abstract

The LHCb experiment which will be operated at the LHC accelerator aims to measure systematically all observable CP violation effects and the rare decays of the B-mesons. The reconstruction of charged particle tracks close to the beampipe will be done by the Inner Tracking system. A spatial resolution of $\sigma < 200\,\mu$m and a small radiation length are required. At rates up to $2 \cdot 10^4 \mathrm{mm}^{-2}\mathrm{s}^{-1}$ the occupancy should not exceed a few percent to allow for efficient track reconstruction.
One possible technology for the LHCb Inner Tracker is the implementation of a gas detector using three GEM foils to achieve the necessary gas amplification (Triple GEM detector). For the first time full scale prototypes (three different designs) of Triple GEM detectors were built. Several new developments were implemented, for example a segmented GEM foil and a two dimensional readout. Different techniques for assembling the detectors were developed.
The timing resolution of the Triple GEM detector was investigated using a special amplifier. In several beam tests the performances in high rate hadron fluxes were studied including discharge probabilities and prevention of discharges.

Zusammenfassung

Das LHCb Experiment wird am LHC Beschleuniger durchgeführt und hat als Ziel, systematisch alle beobachtbaren CP verletzenden Effekte und seltene Zerfälle von B-Mesonen zu untersuchen. Die Rekonstruktion von Spuren geladener Teilchen in der unmittelbaren Nähe des Strahlrohres wird vom inneren Spurkammersystem durchgeführt. Hierfür wird eine räumliche Auflösung von $\sigma < 200\,\mu$m und eine kleine Strahlungslänge benötigt. Bei Teilchenraten von bis zu $2 \cdot 10^4 \mathrm{mm}^{-2}\mathrm{s}^{-1}$ dürfen höchstens ein paar Prozent der Auslesekanäle ansprechen, um eine effiziente Spurrekonstruktion zu gewährleisten.
Eine mögliche Technologie für das innere Spurkammersystem des LHCb Experimentes ist ein Gasdetektor, der drei GEM-Folien verwendet, um die nötige Gasverstärkung zu erreichen (Triple-GEM-Detektor). Zum erste Mal wurden große Triple-GEM-Detektorprototypen gebaut (drei verschiedene Konstruktionen). Hierbei wurden verschiedene neue Entwicklungen implementiert, wie zum Beispiel eine segmentierte GEM-Folie und eine zweidimensionale Auslesestruktur. Verschiedene Techniken für den Bau solcher Detektoren wurden entwickelt.
Die Zeitauflösung von Triple-GEM-Detektoren wurde mit Hilfe eines speziellen Verstärkers gemessen. In Tests mit einem intensiven Hadronenstrahl wurde die Leistungsfähigkeit der Detektoren untersucht. Dies beinhaltete auch Studien zur Wahrscheinlichkeit für das Auftreten von elektrischen Überschlägen und das Vermeiden solcher Überschläge.

Contents

Chapter 1

The LHCb experiment

LHCb is a second generation experiment on b-quark physics which will be operated at the LHC (Large Hadron Collider) at CERN. The goal of the experiment is to measure systematically all observable CP violation effects and the rare decays in the B-meson system with unprecedented precision. It will allow to improve the knowledge on standard model physics and look for new CP violation effects possibly induced from physics beyond the standard model.

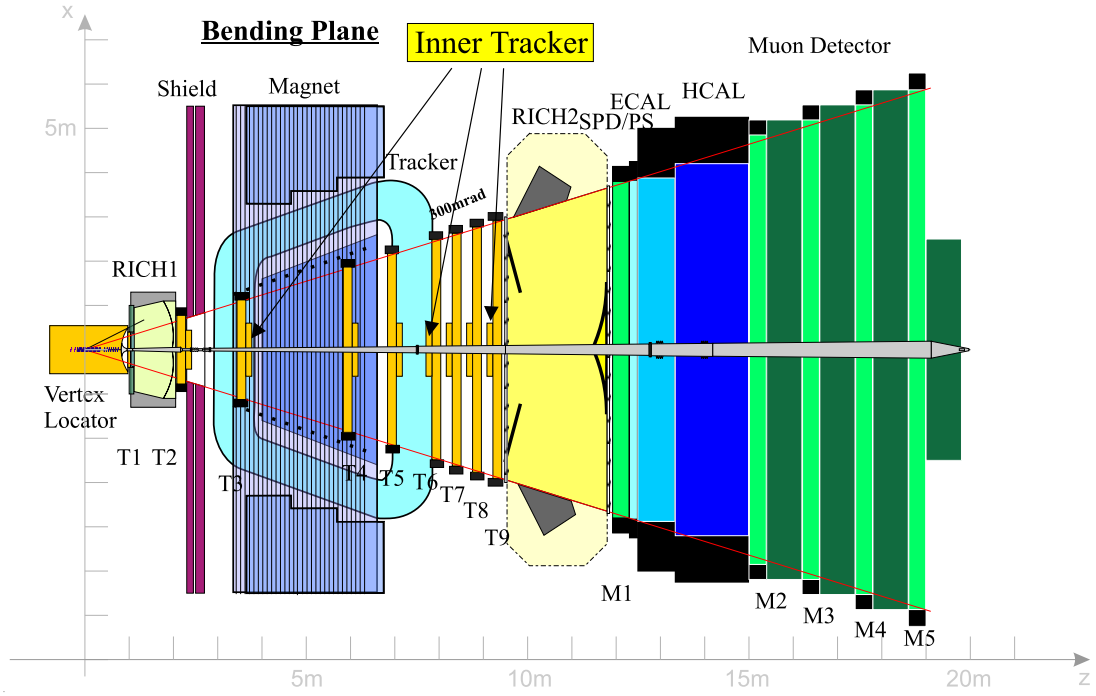

Figure 1.1: Top view of the LHCb detector.

The LHCb experiment is a single arm forward spectrometer (see figure 1.1). The detector consists of a micro-vertex detector system at the intersection point, a tracking system, aerogel and gas RICH counters, a large-gap dipole magnet, electromagnetic and hadronic calorimeters and a muon system. A forward geometry of the detector is adequate because B-meson pairs are predominantly produced at low angles with respect to the beam pipe [1].

1.1 CP violation

CP violation was first discovered in neutral kaon decays in 1964 [2]. The origin of CP violation is still one of the outstanding mysteries of elementary particle physics. The standard model of particle physics describes CP violation with a single complex phase in the quark mixing matrix V_{CKM} [3]. In the following the Wolfenstein parametrisation [4] will be used, in which η represents the imaginary CP violating component:

$$V_{\mathrm{CKM}} = \begin{pmatrix} V_{\mathrm{ud}} & V_{\mathrm{us}} & V_{\mathrm{ub}} \\ V_{\mathrm{cd}} & V_{\mathrm{cs}} & V_{\mathrm{cb}} \\ V_{\mathrm{td}} & V_{\mathrm{ts}} & V_{\mathrm{tb}} \end{pmatrix} = \begin{pmatrix} 1-\lambda^2/2 & \lambda & A\lambda^3(\rho - i\,\eta) \\ -\lambda & 1-\lambda^2/2 & A\lambda^2 \\ A\lambda^3(1-\rho-i\,\eta) & -A\lambda^2 & 1 \end{pmatrix} + \delta\, V_{\mathrm{CKM}} \tag{1.1}$$

The first part is accurate to third order in λ. Once the CP violation in the B system will be measured to an accuracy of order 2% or better, terms up to order λ^5 will have to be taken into account. This is also needed for the determination of the CP violation in the K system:

$$\delta\, V_{\mathrm{CKM}} = \begin{pmatrix} 0 & 0 & 0 \\ -i\,A^2\lambda^5\eta & 0 & 0 \\ A(\rho + i\,\eta)\lambda^5/2 & (1/2-\rho)A\lambda^4 - i\,A\lambda^4\eta & 0 \end{pmatrix} \tag{1.2}$$

Often the phases of the complex numbers are also quoted: $\beta := -\arg V_{\mathrm{td}}$, $\gamma := -\arg V_{\mathrm{ub}}$, $\delta\gamma := \arg V_{\mathrm{ts}} \approx 2\%$.

For CP violation, the relevant parameters are ρ and η and the complex phase angles γ and β. The unitarity relations of the V_{CKM} matrix are often displayed as triangles in the complex plane. Of special interest is the equation

$$V_{\mathrm{ud}}V_{\mathrm{ub}}^* + V_{\mathrm{cd}}V_{\mathrm{cb}}^* + V_{\mathrm{td}}V_{\mathrm{tb}}^* = 0 \tag{1.3}$$

Using the Wolfenstein parametrisation and dividing out the common factors $A\lambda^3$, it takes a very simple form. Two of its three angles are just the complex arguments of the components V_{td} and V_{ub} (see figure 1.2).

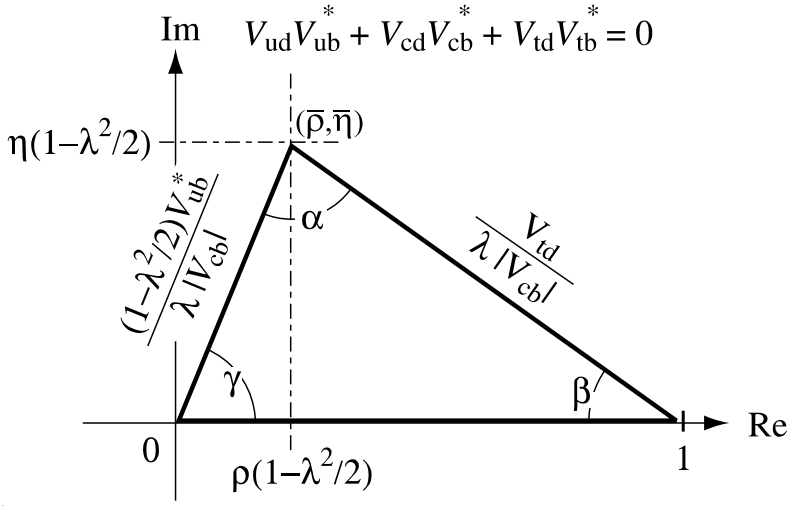

Figure 1.2: The unitarity triangle in the complex plane, representing equation 1.3 in the Wolfenstein parametrisation, using terms up to λ^5.

The area of this triangle (in this parametrisation it equals to $\bar{\eta}/2$) is independant of the selection of the parametrisation and is often referred to as the "size of CP violation". The coordinates of the tip of the triangle then become

$$\begin{aligned} \bar{\rho} &:= \rho\,(1-\tfrac{\lambda^2}{2}) \\ \bar{\eta} &:= \eta\,(1-\tfrac{\lambda^2}{2}) \end{aligned}$$

LHCb is a universal b-physics experiment. As examples, the expected performance in two typical decay channels to be studied will be described here. Both allow an accurate measurement of the angle γ:

$B_d^0 \to D^{*-}\pi^+$: The relevant SM diagrams are shown in figure 1.3. The decay with a D^* created by an external tree contains the vertex factor $V_{\rm ub}$, giving rise to an additional angle γ in the interference with the direct production of D^*. The asymmetry of the time dependant amplitude is thus proportional to $\sin(2\beta+\gamma)$. Since the production of the second diagram is suppressed by $|V_{\rm ub}|^2$, the oscillation amplitude is, however, very small (only about 1%), such that large statistics are necessary. LHCb will produce about 250'000 reconstructed and identified events per year, which allows the determination of the angle $2\beta+\gamma$ with an accuracy of 7° per year.

If we replace in these diagrams both d quarks by s quarks, we arrive at the reaction $B_s \to D_s^- K^+$. The strength of the two diagrams becomes now of similar magnitude, therefore the interference and the amplitude of the asymmetry become larger. The absolute rate is, however, smaller due to the smaller production rate of B_s and the smaller vertex factor $V_{\rm us}$ instead of $V_{\rm ud}$ in the upper diagram. The mixing diagram contains now $V_{\rm ts}$

instead of V_{td} and is thus sensitive to $\delta\gamma = \arg V_{\mathrm{ts}}$ instead of β. LHCb will produce about 2500 reconstructed and identified events per year, allowing to determine $\gamma - 2\delta\gamma$ with an accuracy of about 12° per year.

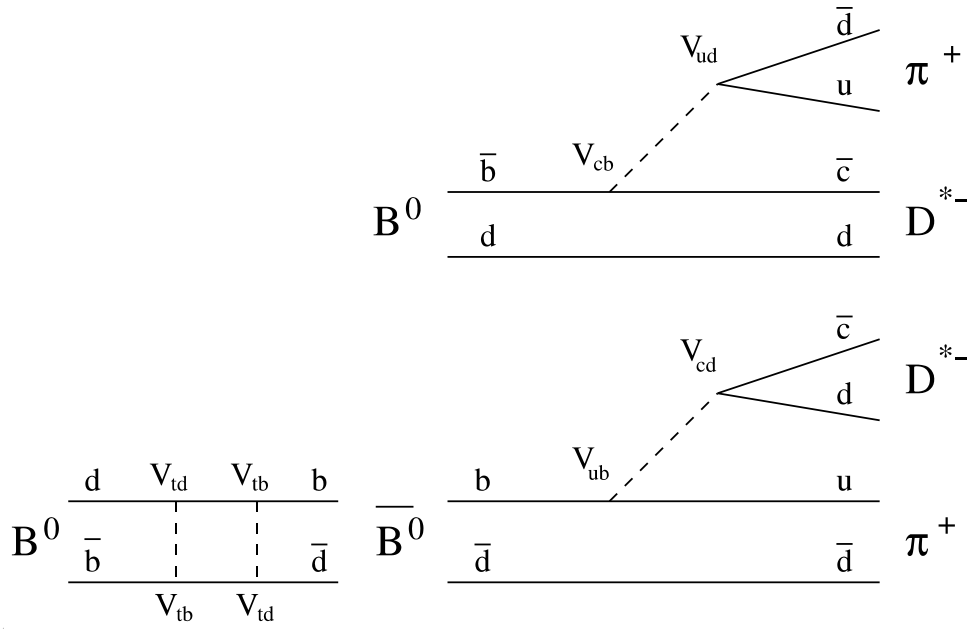

Figure 1.3: Standard model diagrams for the process $B_d^0 \to D^{*-}\pi^+$.

These accurate measurements of γ will complete the study of the unitarity triangle with high precision. This, and the direct comparison to various other methods to measure γ, will allow to observe even very small inconsistencies due to new physics.

1.2 Tracking

The principal task of the tracking system of the LHCb experiment is to provide efficient reconstruction of charged particle tracks and a precise measurement of their momenta. It also has to provide measurements of track directions in both x and y projections for reconstruction of Cherenkov rings in the RICH detectors. The main tracking system comprises nine tracking stations situated between the Vertex Detector vessel and the calorimeters. These are shown in figure 1.1 denoted as T1 - T9. The geometry of the tracking detectors and the choice of technologies are motivated by the requirement of low occupancies.

Most of the detector acceptance is exposed to a particle density which is low enough to use drift chambers with small cells. This Outer Tracker System consists of straw-tube-like chambers. The Inner Tracking System covers (in most stations) an area of about $60 \times 40\,\mathrm{cm}^2$ around the beampipe.

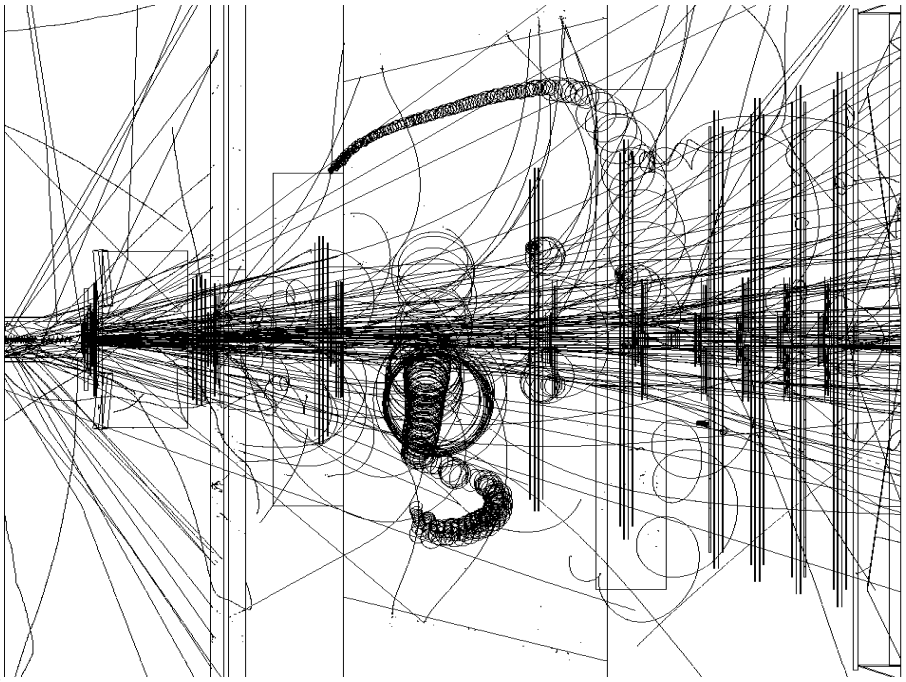

Figure 1.4: GEANT3 LHCb event displays. An example of a "medium mulitplicity" B event.

The tracking system provides precise particle trajectories in the bending plane of the spectrometer using near-vertical wires and strips. Three dimensional track reconstruction is achieved using small stereo angles of $\pm 5^\circ$ [5].

1.3 Requirements for the Inner Tracker

The Inner Tracking system consists of 9 stations mounted vertically around the beam axis. Momentum and invariant mass resolution require a position resolution of $\sigma < 200\,\mu$m, while the radiation length should be kept as small as possible (in the simulations so far a value of about 2% per station is assumed). A stereo angle of $\pm 5^\circ$ is needed and each station provides four measurements: x, u, v, x, where u and v denote the stereo layers. For an efficient pattern recognition the channel occupancy has to be kept below a few %, which also requires the time occupancy of the signals not to exceed two or three LHC bunch crossing of 25 ns.

Simulation of the LHCb interaction region, including the beam vacuum chamber, were performed to estimate the particle flux [6], using an average nominal luminosity of $2{\times}10^{32}$ cm^{-2}s^{-1}. The peak luminosity is assumed to be higher by a factor 2.5. The particle flux and its composition depends strongly on the position parallel to the beam axis z

and on the distance from the beam: the maximum charged hadron rate is expected to be 8×10^3 mm^{-2}s^{-1} and the maximum electron and positron rate (originating mostly from photon interaction with the beam pipe) might be as high as 5×10^4 mm^{-2}s^{-1}. A large fraction of the latter enters the detector under a large inclination angle (see figure 1.4). The total counting rate per station reaches between 200 and 1000 MHz, again depending on z. These rates correspond to a maximum total radiation dose of about 1.6 Mrad/year.

1.4 A gas detector for the Inner Tracker

In the LHCb technical proposal [5] three detector technologies were considered to meet the requirements for the Inner Tracker. A MSGC detector in combination with a GEM foil was chosen as the baseline solution. The well proven fall back solution, silicon strip detectors, was estimated to be significantly more expensive. To reduce costs also a new detector type, the Micro Cathode Strip Chamber (MCSC) was considered.

Further investigations of the Gas Electron Multiplier (GEM) showed that a sufficient gas gain to detect minimum ionizing particles can be obtained by using one GEM foil [18].

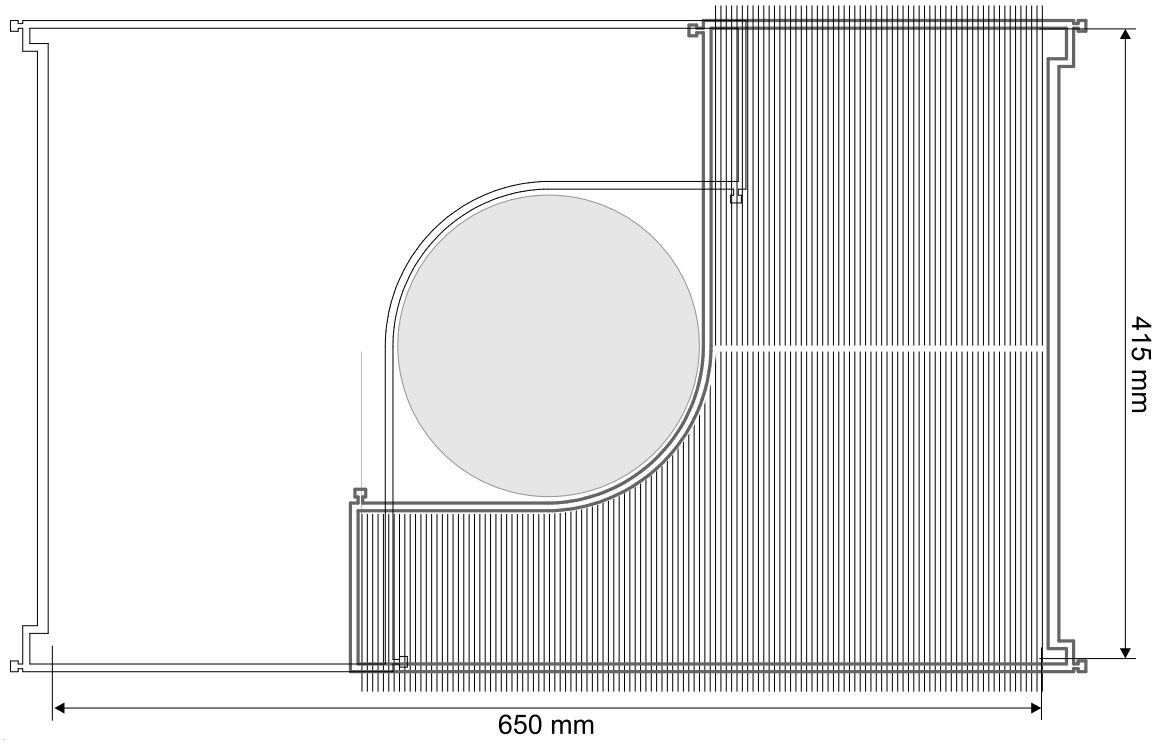

Figure 1.5: Two Triple GEM detectors (third prototype) mounted around the LHC beampipe. In one detector the anode wires are indicated as narrow lines.

However, a major problem of gas micropattern detectors comprises the fact, that very high primary ionisation can occur in hadronic particle beams from time to time. This may lead to high voltage breakdowns producing dead time, huge electronic noise to other detectors and even may damage the detector and the readout electronics. We require both, that the spark rate is limited to one per hour per tracking plane and that the detector should survive for several years of data taking. Taking into account the expected hadron particle flux it follows, that the discharge probability per incident particle must not exceed 10^{-12}.

It turns out that these conditions can only be met by cascading at least three GEM foils, the Triple GEM detector. The possible implementation of a Triple GEM detector as Inner Tracker is shown in figure 1.5.

1.5 The different prototypes

Within the scope of this work three different large prototypes of Triple GEM detectors were built. A summary of the main features of the different prototypes is given in the following table. A detailed description of the manufacturing processes is given in chapter 6.

feature	first prototype	second prototype	third prototype
size	23 cm × 25 cm	30 cm × 23 cm	45.0 cm × 41.5 cm
production place	Heidelberg	Zürich	Lausanne/Novosib.
outer shape	rectangular + radius	rectangular	L-shape
drift gap width	3.0 mm	3.0 mm	3.0 mm
transfer gap width	3.0 mm	1.0 mm	1.0 mm
collection gap width	3.0 mm	1.0 mm	1.0 mm
cylinder spacers	none	in transfer + collection	in all gaps
glue	Epo-Tek H72	Epo-Tek H72	Epo-Tek 302-3M
GEM dimensions [1)]	140/95/55	140/80/50	140/80/50
GEM copper thickness	7 μm	15 μm	5 μm
GEM segmentation	no segmentation	10 fold	100 fold
readout board type	one dim.	two dim./ straight str.	two dim./ Zig-Zag
readout pitch	500 μm	300 μm (per layer)	400 μm (per layer)
anode strip width	200 μm	60 μm / 250 μm	60 μm / 150 μm

[1)] Characteristic GEM dimensions in μm: pitch / copper hole diameter / Kapton hole diameter

Chapter 2

Physics of gas detectors

2.1 The ionization process in gases

As a fast charged particle passes through a gas it creates both excited molecules and ionized molecules along its path. After the ionization of a neutral, the resulting positive ion and free electron is called an ion pair and serves as the basic constituent of the electrical signal. Ion pairs can be formed either by direct interaction with the incident particle, or through a secondary process in which some of the particle energy is first transferred to an energetic electron or "delta ray". The momentum dependence of the mean energy loss is given by the Bethe-Bloch equation. The minimum energy losses $(dE/dx)_{min}$ at $p/m \approx 1$ for common gases are shown in table 2.1. The practical number of interest is the total number of ion pairs created along the track of the radiation. To calculate this number the average energy lost by the incident particle per created ion pair (the so called "W-Value")

gas	W (eV/Ion Pair)	de/dx (keV/cm)	$1/\lambda$ (clusters/cm)	t_{gg} (mm)
He	41	0.32	5	9.2
Ne	36	1.41	12	3.8
Ar	26	2.44	25	1.8
Kr	24	4.60		
Xe	22	6.76	46	1.0
CO_2	33	3.01	35	1.3
CH_4	28	2.21	27	1.7
C_4H_{10}	23	4.50		

Table 2.1: For various gases at STP: (a) W-value,(b) energy loss [8], (c) the yield of ionization encounters (clusters) produced by a m.i.p., and (d) t_{gg}: thickness of gas layer for 99% efficiency [9].

is used. Due to competing excitation processes the W-Value is always substantially greater than the ionization energy [7].

The number of free electrons per cm can be calculated by dividing the energy loss per cm by the energy which is needed to form an ion pair. To calculate the number of free electrons for a gas mixture these values have to be weighted with the percentage of the mixing ratio. Assuming a gas mixture of 70% Argon and 30% CO_2 (at atmospheric pressure) this leads to an average number of electrons created in a 3 mm thick volume of: $N_e \approx 0.3\,\mathrm{cm} \times (0.7\,\frac{2.44\mathrm{keV/cm}}{26\mathrm{eV/e^-}} + 0.3\,\frac{3.01\mathrm{keV/cm}}{33\mathrm{eV/e^-}}) = 28\mathrm{e^-}$. The primary electrons created from a charged particle traversing a gas volume are distributed over several clusters which contain a varying number of primary electrons. The yield $(1/\lambda)$ of ionization clusters per cm for a minimum ionization particle (m.i.p.) is given in table 2.1. The probability for a charged particle traversing a gas layer of thickness Δ to have at least one ionization encounter is $1-\exp(-\Delta/\lambda)$. The thickness of the gas layer which is needed to obtain 99% efficiency is $t_{gg} = 4.6\,\lambda$. Depending of the gas, some 65-80% of the clusters contain only one electron. The probability that a cluster contains more than five electrons is smaller than 10%.

2.2 Transport parameters

An external electrical field in the region where ions and electrons exist in the gas, will tend to move the charge away from their point of origin. This motion is a superposition of a random thermal velocity together with a mean drift velocity. For ions the drift velocity can be predicted from the relationship: $v = \mu\, p_0\, \frac{E}{p}$, where E is the electric field strength, p the gas pressure and p_0 the standard pressure. Typical values for the mobility μ are between 1 and $1.5 \cdot 10^{-4}\,\mathrm{m^2/Vs}$. In an electrical field of 3 kV/cm this leads to an ion drift velocity of about 25 μs/mm.

The lower mass of the electrons allows a greater acceleration between two impacts. The electron mobility is typically 1000 times greater than for ions. Furthermore there is a saturation effect for the drift velocity as shown in figure 2.1.

Ions and electrons created within the gas have a tendency to diffuse away from regions of high density. The diffusion has two terms, longitudinal and transverse to the field, and they will correspondingly disperse the cloud of electrons. The transversal diffusion of electrons drifting in parallel to an external electrical field E is described by a Gaussian distribution with a standard deviation $\sigma_x = \sigma_T\sqrt{d}$, where σ_T is the field dependent diffusion coefficient (see figure 2.2) perpendicular to E. The transverse diffusion coefficient σ_T plays the main role in the resolution and the cluster width.

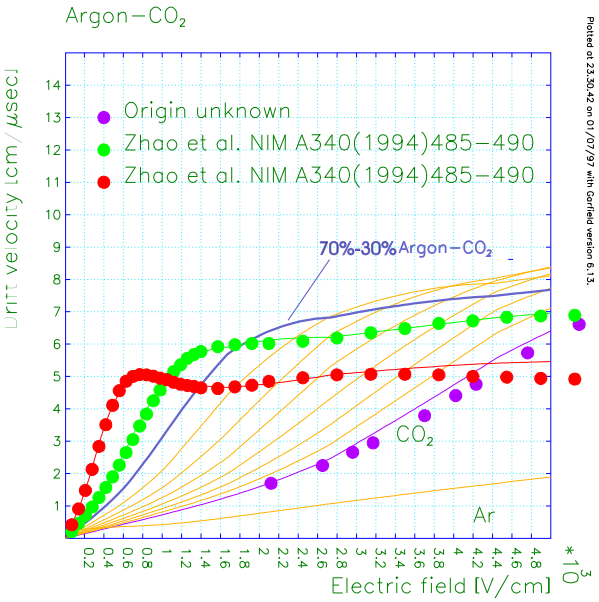

Figure 2.1: Drift velocity for Ar/CO_2 mixtures varying from pure Argon to pure CO_2 in steps of 10 % [10].

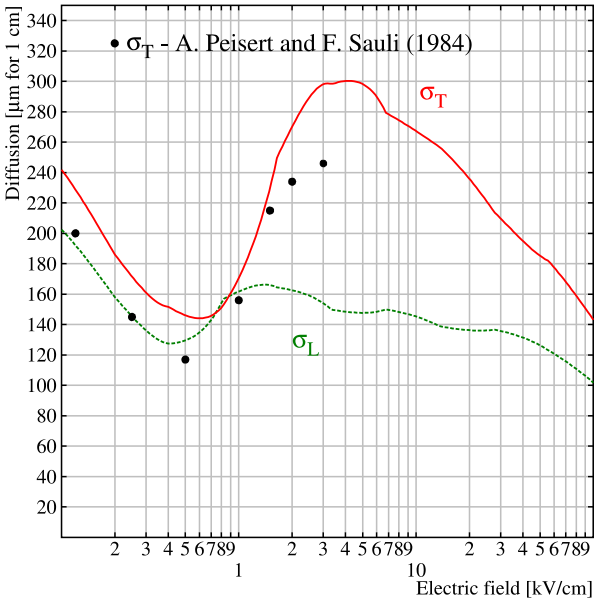

Figure 2.2: Longitudinal and transversal diffusion coefficients for Ar/CO_2 70/30 [11].

2.3 Amplification process

By further increasing the electrical field in the gas, free electrons can be accelerated to have enough kinetic energy to ionize other gas molecules. In typical gases at atmospheric pressure, the threshold field is of the order of 10^4 V/cm. The electron liberated by this secondary ionization process will also be accelerated and can create additional ionization. A so called Townsend avalanche is formed. The avalanche terminates, when all free electrons have been collected by the anode. Under proper conditions the number of secondary ionization events can be kept proportional to the total number of primary ion pairs.

2.4 Fill gases

In order to run the detector efficiently it is important that the drifting electrons are not captured by the gas molecules (attachment). Electronegative gases for example oxygen have to be avoided. The main constituent of a counting gas are noble gases. Noble gases and hydrocarbon gases are characterized by relatively low electron attachment coefficients.

Gas multiplication is based on collisions between electrons and neutral gas molecules. In addition to ionization, these collisions may also produce excitation of the gas molecules. The excited molecules may decay to their ground state through emission of a visible or

ultraviolet photon. These photons could produce elsewhere in the detector a free electron for example by photoeffect. This may result in additional electrons and loss of the proportionality of the signal with the primary ionization. A small amount of a polyatomic gas, such as Methane, will absorb these photons without further ionization (quencher).

Most good quenching gases are complex hydrocarbon molecules such as for example dimethylether and isobutane. However they tend to build polymers on the electrodes, when exposed to heavy ionisation (so called gas aging). In addition these gases are flammable, which demands a lot of safety infrastructure. Therefore in the following work all measurements were performed with an argon and carbon dioxide mixture.

2.5 Wire chambers

To use a gas detector as tracking device the multi-wire proportional chamber (MWPC) was invented [12]. It consists of a plane of parallel sense wires with spacing s. With digital readout, the resolution is $s/\sqrt{12}$, where s is typically 1-2 mm. A better resolution can be achieved by measuring the difference in time between the arrival of electrons at the wire and the traversal of the particle. In this case (drift chambers), the spatial resolution is limited by the diffusion of electrons during the drift and and by the fluctuations of the ionization process. Resolutions in the range 100-200 μm have been achieved. The spatial resolution cannot be improved by arbitrarily reducing the spacing of the wires, the electrostatic force between the wires balanced by the mechanical tension, cannot exceed a critical value [9] and the electrical field on the cathode surface would become too large.

2.6 Micro pattern gas detectors

The limitation in wire spacing can be overcome by means of lithographic techniques [13]. A series of thin metallic strips are precisely engraved on an isolating support producing a miniaturized version of a MWPC, the micro strip gas chamber (MSGC). With this technique the spacing of the anodes can be reduced to 0.1-0.2 mm improving spatial resolution, granularity and rate capability. However, the slow degradation under sustained irradiation (aging) [14] and the serious damages that can be produced by discharges make this detector technology not suitable for large scale particle physics applications [15]. Recently new types of detectors were introduced which aim at improving on these points; micro-dot, micromegas, gas electron multiplier are promising examples. They have in general higher reliability, and can be produced at lower costs [16].

Chapter 3

The Gas Electron Multiplier

The Gas Electron Multiplier (GEM) was introduced by F. Sauli [17] as a preamplifier for electrons in gas detectors. It was first used in combination with a MSGC (Micro Strip Gas Chamber), where the splitting of the total gas amplification into two steps reduced the probability to produce a discharge under hadronic irradiation. It was shown that a sufficient gas gain for detecting minimum ionizing particles can be obtained by using one GEM foil or cascading several GEM foils [18]. The gas amplification can be done without a MSGC.

3.1 Manufacturing of GEM foils

A GEM foil consists of two thin copper sheets separated by an insulating dielectric, usually Kapton. The typical thickness of the copper ranges from 5 to 15 μm, for the insulator it is 50 μm. Extensive studies by the Gas Detectors Development group at CERN provide

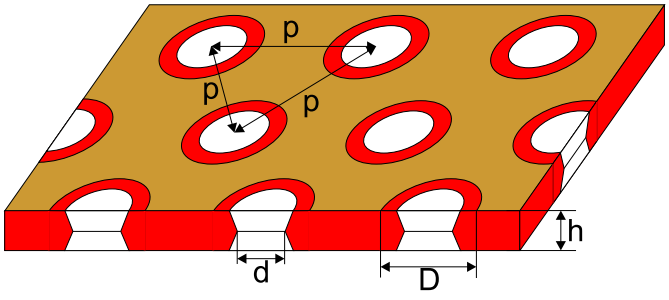

Figure 3.1: Characteristic dimensions for a GEM foil.

useful values for the parameters of the GEM holes [19]. A schematic drawing of a GEM foil is shown in figure 3.1. The standard GEM foil has holes arranged in a triangular pattern

with a pitch of p=140 μm, whereas the copper free region has a diameter of D=80 μm and the hole in the Kapton has a diameter of d=50 μm.

The production technique of GEM foils was invented by the printed circuit workshop of CERN [20] and can be briefly described as follows. The most common base material for etching a GEM foil is an adhesiveless laminate of a Kapton foil in-between of two copper layers [21]. This copper clad Kapton foil is coated with a photo sensitive film. Two identical masks with the wanted pattern are aligned and the cladded Kapton is inserted in-between. After exposure to UV-light and development, the copper holes are etched in conventional solvents. For the Kapton etching the remaining copper acts as the etching mask. A detailed description of the fabrication process can be found in [22].

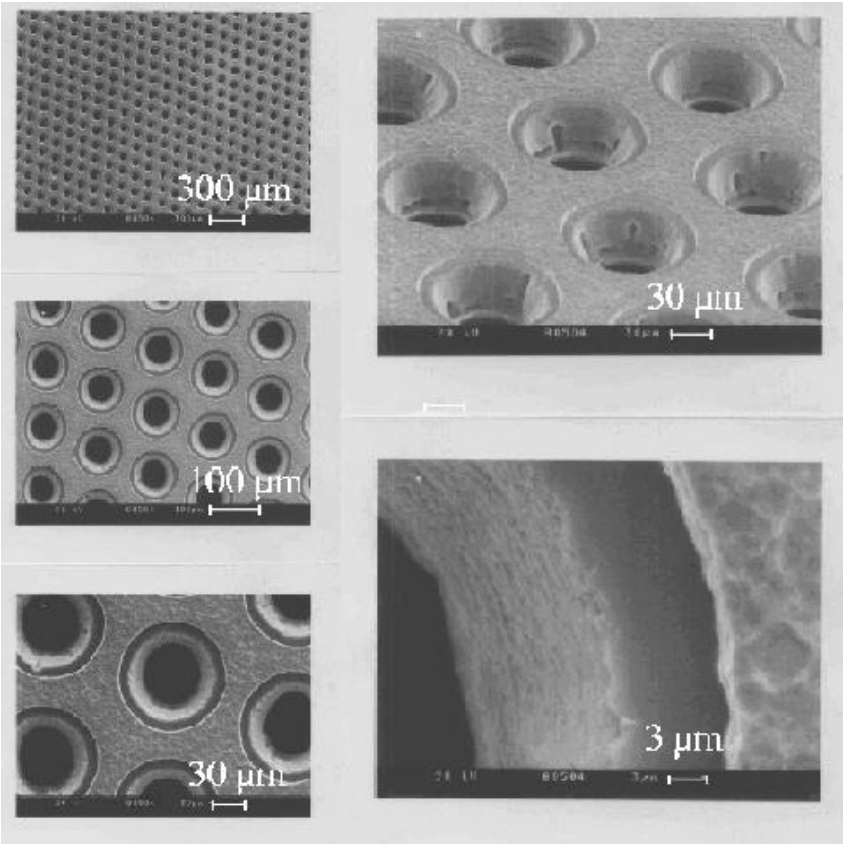

Figure 3.2: Photo of a GEM foil produced for the HERA-B experiment taken with an electron microscope.

A picture of a GEM foil produced for the HERA-B experiment is shown in figure 3.2. This GEM foil was produced with a second step of copper etching in order to remove sharp edges around the copper holes. This results in a better high voltage performance. Later advanced production techniques made this step unnecessary.

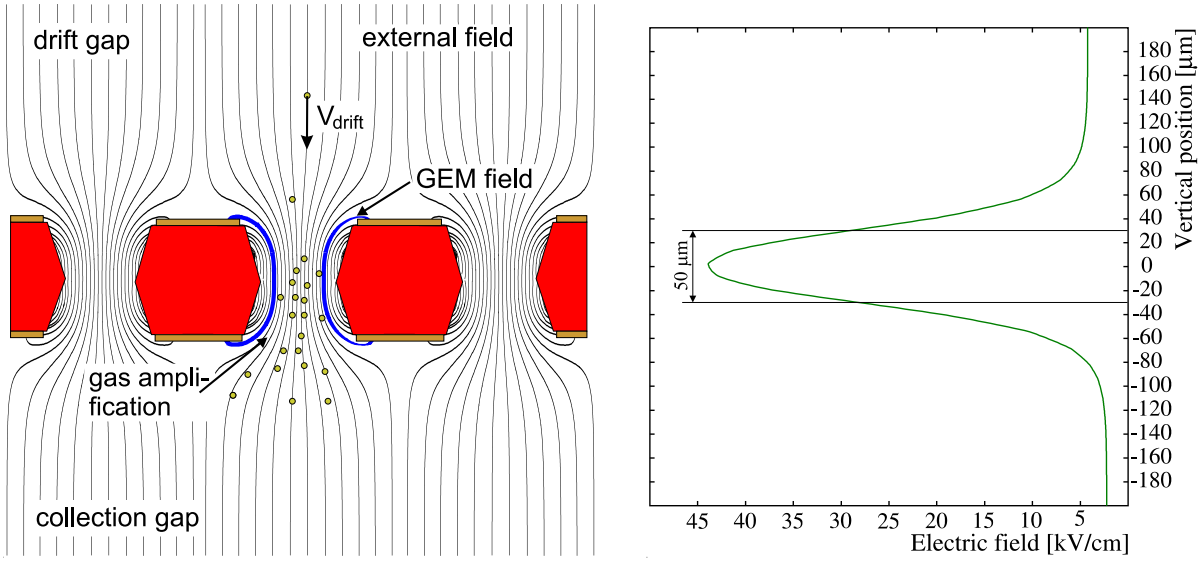

Figure 3.3: left: Principle drawing of the gas amplification process in a GEM foil. right: Electric field strength along the GEM hole axis at a GEM voltage of 360 V [11].

3.2 Operation principle of GEM foils

By applying a potential difference (typically 320 V to 450 V) between the two copper electrodes (the GEM voltage), a dipole field is generated in the GEM holes. When placing the GEM foil into an external electrical field, the field lines are guided through the GEM holes. Electrons drifting along the field lines will generate secondary electrons in the high electric field (see figure 3.3 left). A simulation of the field strength achieved along the GEM hole axis is shown in figure 3.3 (right).

For a better understanding the charge multiplication in the GEM foil can be divided into three parts: charge collection, amplification and transfer. The dependence of these parameters on the external electrical fields is described in the following sections.

3.2.1 Drift field

The drift field is applied between the upper GEM side and the drift electrode. This electrical field forces the electrons to drift towards the GEM foil. The drift field lines are either guided through the GEM holes or terminate on the upper side of the GEM foil as shown in figure 3.4 (1). The fraction of electrons that reaches the amplification region in the hole is called electrical transparency t_{el}.

The dependence of the transparency on the drift field was studied with a triple GEM detector in a high intensity particle beam (see chapter 9). The transparency was calculated

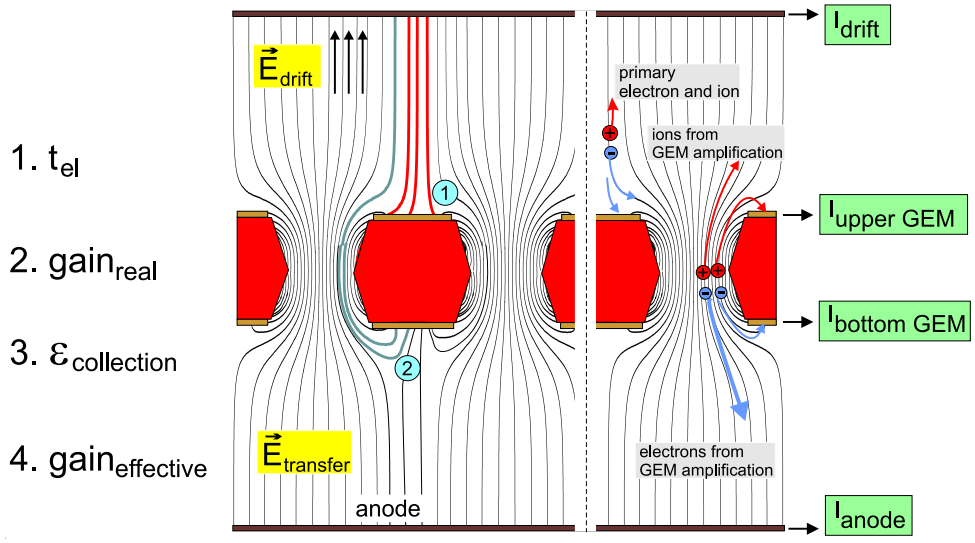

Figure 3.4: Field lines terminating on the upper GEM side (1), field lines from the GEM hole terminating on the bottom GEM side(2). Right part: origin of the currents created in a GEM foil.

using $t_{el} = I_{anode}/I_{anodemax}$, where $I_{anodemax}$ was the maximum anode current obtained during a scan of the drift field. However, this method does not give the absolute value of the transparency. But it indicates the extension of the plateau for higher GEM fields. A detailed measurement of the single electron transparency can be found in [23].

In figure 3.5 (left) the transparency as function of the drift field is shown. At small drift fields almost all field lines are guided through the GEM holes and the electrical transparency shows a plateau. At higher drift fields more electrons reach the upper GEM side and the transparency starts to decrease.

3.2.2 GEM voltage

The transparency is additionally influenced by the GEM voltage. An increased GEM voltage guides more electrons to the GEM holes and the plateau extends to higher drift fields as indicated in figure 3.5 (left).

Increasing the GEM voltage results in a higher electrical field strength in the GEM holes and a higher gas amplification. This is the main parameter for adjusting the gain of the GEM foil. It changes the "real gain" ($gain_{real}$). This quantity has to be introduced because of the fact, that not all electrons multiplied by the GEM foil reach the anode.

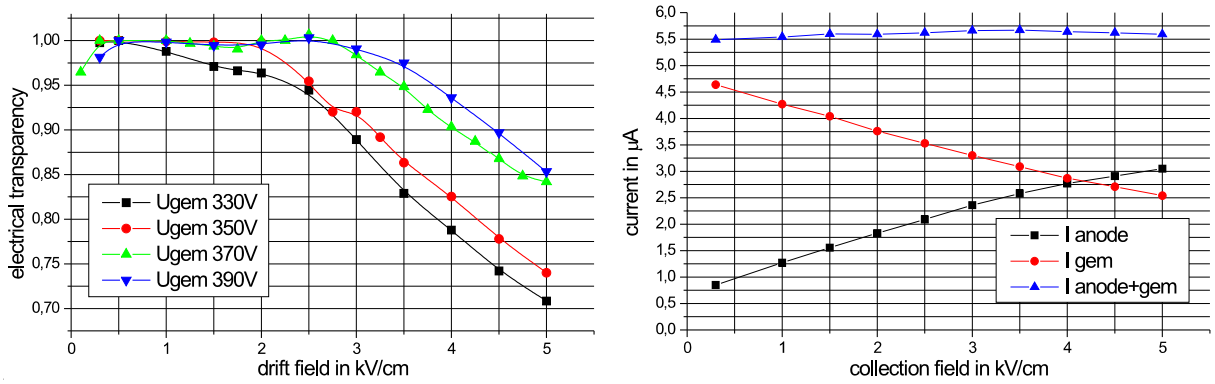

Figure 3.5: left: Transparency for different GEM voltages as a function of the drift field. right: Anode current (inverted) and current at the bottom GEM side (inverted) as function of the collection field.

3.2.3 Collection field

The collection field or induction field is applied between the bottom GEM side and the readout structure (anode). Increasing the collection field results in an increased current at the anode (see figure 3.5 right). Furthermore the current on the bottom GEM side decreases.

As indicated in figure 3.3 (2) field lines from the GEM holes terminate either on the bottom GEM side or on the anode. Also electrons originating from the GEM holes are shared between the anode and the bottom GEM side. By increasing the collection field more electrons are forced to drift towards the anode. The fraction of multiplied electrons which reach the anode is called collection efficiency $\epsilon_{\text{collection}}$.

Typical values for the collection field are in the range from 3 to 5 kV/cm. Higher electrical fields may result in a contact between the GEM foil and the readout anode due to the electrical force of attraction. A higher field also increases the probability to produce a "propagating discharge" (see chapter 10.5).

3.2.4 Effective gain

The "effective gain" of a GEM foil is the ratio between the charge arriving at the anode and the charge from the primary ionization. The effective gain can be calculated as: $\text{gain}_{\text{effective}} = \epsilon_{\text{col}} \cdot \text{gain}_{\text{real}} \cdot t_{\text{el}}$.

3.3 Multi GEM structures

Gas detectors used for particle tracking have to cope with a large dynamic range of the primary ionization. Large amounts of primary electrons may lead to a high voltage breakdown (see chapter 10). The probability to produce a discharge can be reduced by cascading several GEM foils. This is demonstrated in figure 3.6 where the discharge probability per incident alpha particle was determined.

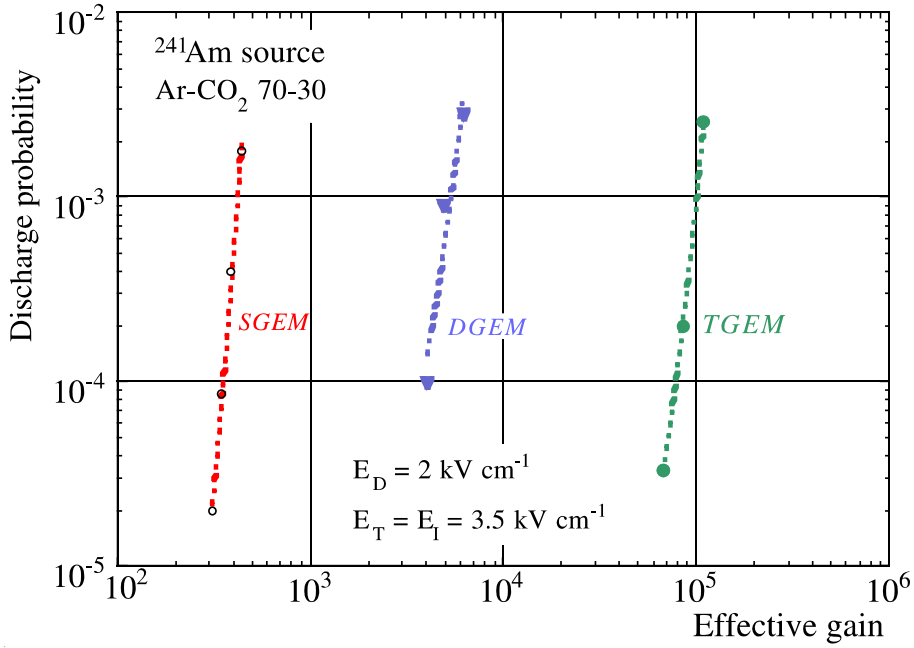

Figure 3.6: Discharge probability as a function of total effective gain for Single, Double and Triple GEM detectors [24].

The electrons released from the first GEM foil are multiplied again by the following GEM foil. The amplification process for the individual GEM foil is not changed by the presence of other GEM foils. The gap in-between the GEM foils is called transfer gap and the associated electrical field is called transfer field (see figure 3.7 left).

Increasing the transfer field extracts more electrons from the first GEM foil which drift towards the second GEM foil resulting in a raise of the anode current. At transfer fields above 3 kV/cm the transparency for the second GEM foil starts to decrease. More electrons from the first GEM foil terminate on the upper side of the second GEM foil and the anode current diminishes (see figure 3.7 right).

With a triple GEM detector almost a ten times higher gain can be achieved than with a double GEM detector. In view of high particle rates at LHC it was decided to build

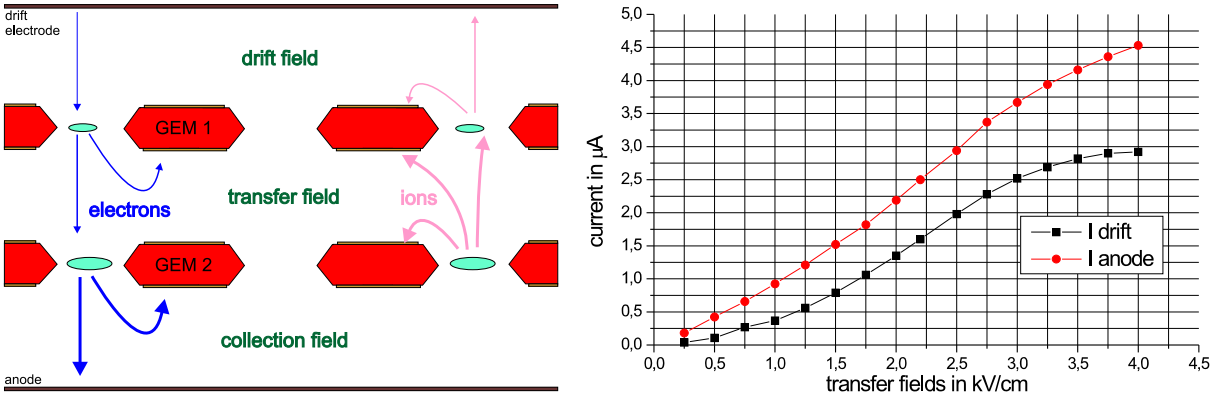

Figure 3.7: left: Flow of electron and ion currents in a double GEM detector. right: Anode current (inverted) and current at the drift electrode as function of the transfer fields. This measurement was performed using a triple GEM detector setting both transfer fields to the same electrical field strength.

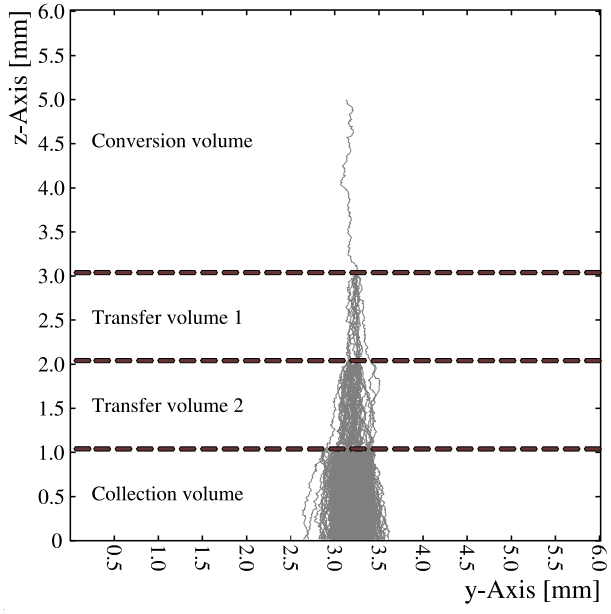

Figure 3.8: Avalanche in a Triple GEM detector resulting from a single electron released in the drift gap (conversion volume) [11].

prototype detectors with three GEM foils to ensure the operation stability in a high rate experiment. A simulation of an avalanche in a Triple GEM detector is shown in figure 3.8.

Chapter 4

Signal shape of detector pulses

At the LHC collider the bunch crossing time will be 25 ns. To avoid pile up of signals of consecutive bunch crossing, a fast signal shaping of the detector electronics is required. A specially developed amplifier was used to investigate the pulse shape of a Triple GEM detector. This information can also be used to optimize the response of the preamplifier to be used for such a detector. Recorded detector pulses were analyzed off line to simulate the effect of different shaping times.

4.1 Fast amplifier

For the exact investigation of the signal shape a amplifier with a very fast rise time was developed [25]. This amplifier (internal code VV61) has an input impedance of 50 Ω and a rise time of 0.5 ns. The electrical scheme is illustrated in figure 4.1.

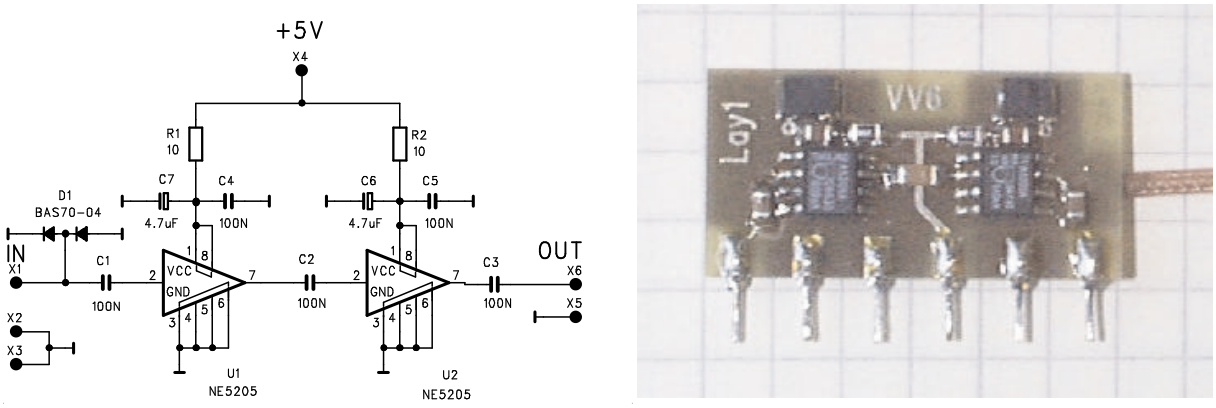

Figure 4.1: Electrical scheme and picture of the VV61 amplifier.

4.2 Signals induced by soft X-rays

For the visualization of signals induced by soft X-rays several anode strips were grouped and connected to one amplifier channel. The output of the VV61 amplifier was directly connected to a digital oscilloscope.

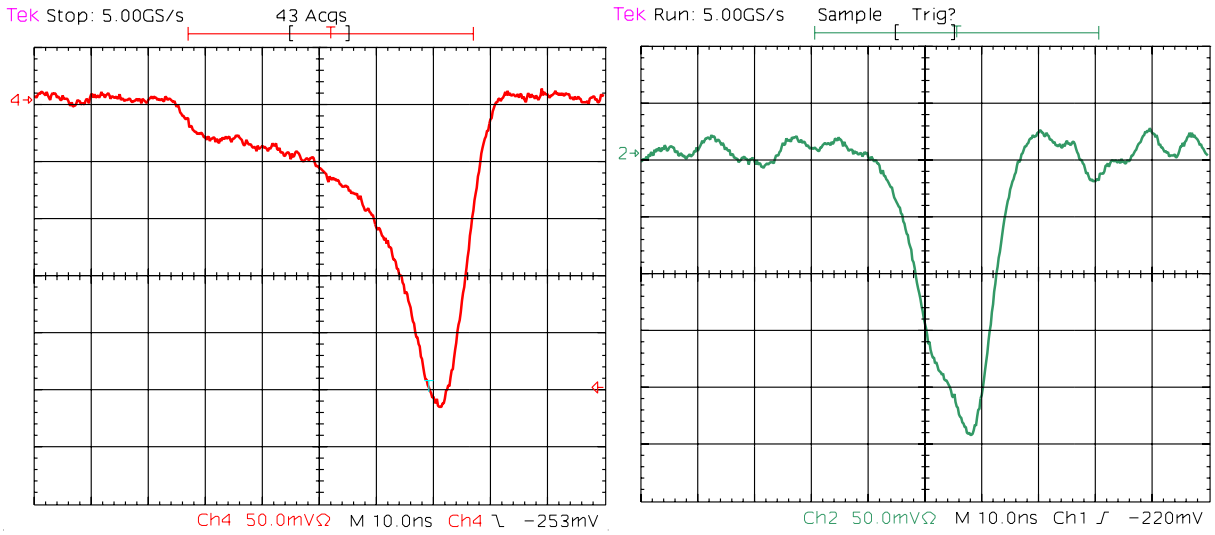

Figure 4.2: left: Signal shape of the first prototype with a 3 mm collection gap (5 strips connected together) right: Signal shape for the second prototype with 1 mm collection gap (8 strips connected together). Timescale 10 ns/div.

Signals obtained with this configuration from a ^{55}Fe source are shown in figure 4.2. The pulse shape can be understood by interpreting the signal as the induced current by the moving charge cluster in the gap between the lowest GEM foil and the readout board:

- The drift velocity in Ar/CO_2 (70%/30%) at 5 kV/cm is $\approx 7.5\,cm/\mu s$, what corresponds to a drift time of 40 ns in the 3 mm gap.
- The total current should remain constant during the drift of the charge cloud. Here a rising signal was observed due to the effect that the strips close to the center of the cloud see an increasing fraction of the total current, as the charge cloud moves closer to the readout board surface. This risetime approximates to the expected 40 ns.
- For the second prototype the risetime of the signal is barely visible (figure 4.2 right), since the drift time in the 1 mm gap is expected to be about 13 ns only.

In figure 4.3 (left) the signals of four adjacent anode strips are shown. At the beginning (t=70 ns) all anode strips show a negative signals. As the charge cloud moves closer to the readout board surface the center strips see an increasing negative signal were the

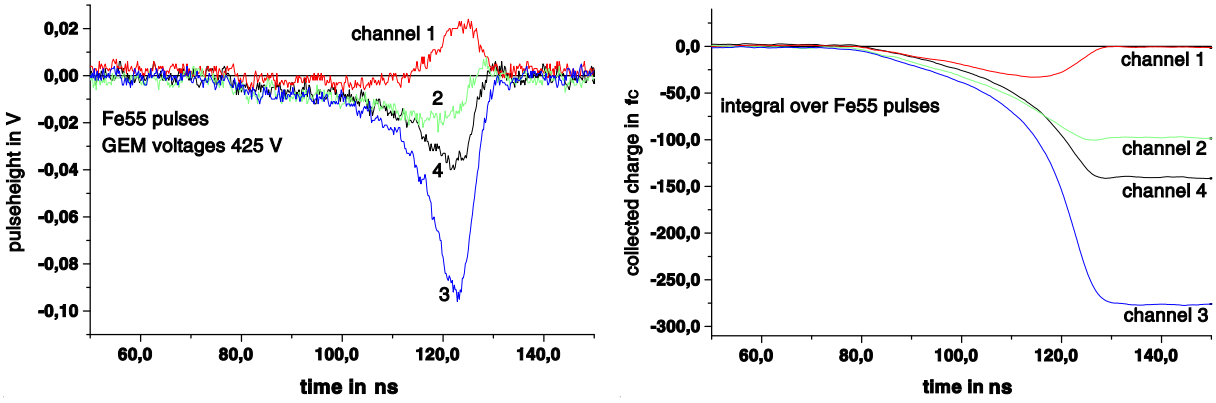

Figure 4.3: left: Photon signals from four adjacent anode strips obtained with the first detector prototype. right: Integrated charge collected on the strips (same event as on the left side)

outer anode strip (channel 1) changed to a positive signal. This outer channel sees an influenced signal. This is demonstrated in figure 4.3 (right), where the integrated signals of four adjacent strips from the same event are displayed separately. As expected the integral of the collected charge over longer time periods for the outer channels, which does not collect any charge directly from the moving electron cloud, vanishes.

4.3 Particle signals

During a test at the PSI [26] with the first detector prototype the signal shape of pulses obtained from pions was studied. The energy of the pion beam was adjustable and set to 350 MeV/c. At this energy pions are almost minimum ionizing particles (m.i.p.). To have a fixed timing between the particle crossing and the trigger of the oscilloscope, an external trigger was derived from the coincidence of two small scintillators.

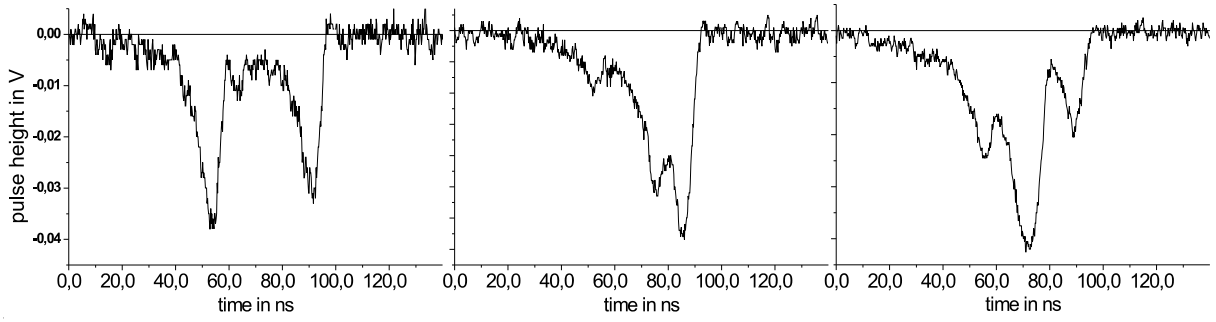

Figure 4.4: Three typical pulses observed from crossing particles. The signals were recorded with the first prototype. The photomultiplier pulse triggered the oscilloscope at t=0 ns.

Four neighboring anode strips were connected to separate amplifier channels. The remaining anode strips of the readout board were shorted to ground. The resulting signal shapes were read out by an oscilloscope and transferred to a PC via a GPIB interface. Some typical signals are displayed in figure 4.4.

In contrast to the ^{55}Fe signals they show several consecutive pulses. This can be explained by the different cluster sizes expected in the primary ionisation gap. The number of 28 primary electrons obtained from a m.i.p. crossing the 3 mm drift gap is the average number of electrons (see chapter 2.1). The primary electrons are distributed over several clusters with different size. The different primary clusters result in separate peaks in the pulse shape (see figure 4.4)

In fact all pulses appear within a time window of 40 ns, which agrees with the expected drift time dispersion of the primary charge in the drift gap.

4.4 Variation of the shaping time

One of the crucial parameters of the final readout electronics for the LHCb Inner Tracker is the integration and shaping time of the detector electronics. To study the system performance as a function of this parameter, a total of 200 events were recorded.

4.4.1 Filter function

The recorded waveforms (in the following called vectors) were folded offline with a Gaussian folding mask (as a simplification of a more realistic CRRC filter function for example).

The principle of the folding can be demonstrated for a small Gaussian mask (1/2/1):

```
old vector:          2  2  3  2  6  2  3  2
                              *  *  *
folding mask:                 1  2  1 => 2 + 12 + 2 = 16  16/4 = 4
                                 |
new vector:             2  3  3  4  3  3
```

The folding mask is multiplied at every point with the data vector, the three resulting values are added up and normalized by 1/4. The result is entered into a new data vector. In a computer program this function can be realized by:

```
do k=1, 254
     Vnew(k) = ( Vold(k-1) + 2*Vold(k) + Vold(k+1) )/4
enddo
```

The Gaussian folding mask can be obtained from the binomial coefficients:

```
 1                1
1/2             1   1
1/4           1   2   1          <= used for the example above
1/8         1   3   3   1
1/16      1   4   6   4   1
```

For the analysis the entries for the folding mask were calculated from a Gaussian function. The sigma of the Gaussian function (here called shaping time) was varied to simulate different shaping times.

4.4.2 Time resolution

The time resolution was studied as a function of the shaping time. The time of the maximum pulse height in each event with respect to the triggering scintillator signal was searched and filled into a histogram. Figure 4.5 (left) shows a histogram for a shaping time of 20 ns. The detection of the maximum pulseheight could be implemented in the final version of the electronics by a zero crossing discriminator. The resulting width of this time distribution is shown in figure 4.5 (right) as a function of the shaping time.

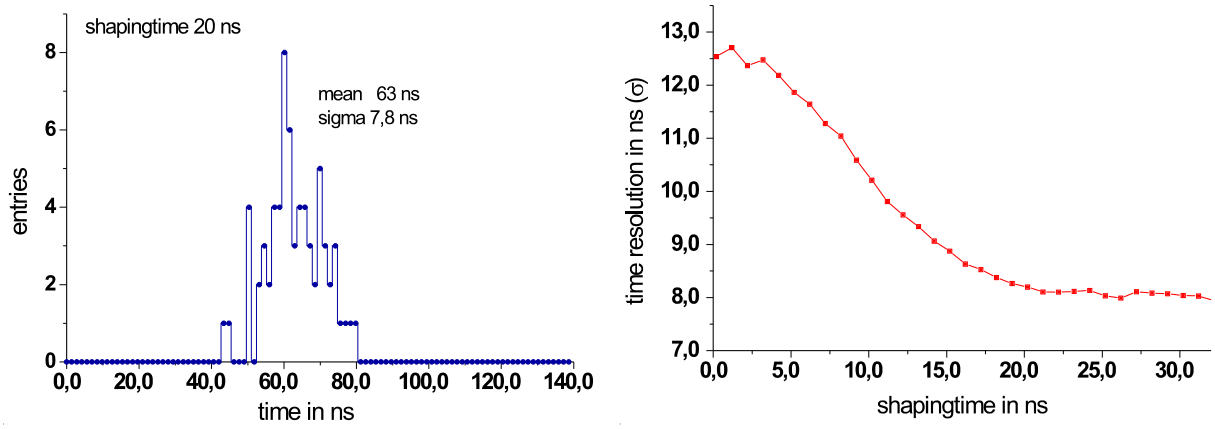

Figure 4.5: left: Histogram of the time when the maximum of the signal occurs. The sigma of this distribution defines the time resolution. right: Time resolution as a function of the shaping applied to the recorded signals.

With this method larger shaping times result in better time resolution. With a longer shaping more information about the clustering of the primary electrons is contained in the peak maximum. A resolution as small as 8 ns was reached.

Alternative methods for defining the particle crossing time could make use of the steep falling of the last cluster observed in the signal, requiring however a much better signal to noise ratio.

During the test at the PSI beam in April 1999 a group from the Petersburg Physics Institute made also studies on the time resolution of triple GEM detectors. They estimated a time resolution of rms $\approx$ 6 ns [27].

4.4.3 Cluster width

The maximum pulse height was between 60 ns and 70 ns after the trigger from the photomultiplier (see figure 4.5 left). A final electronic scheme would most probably sample the signal height at a fixed delay (sampling time) after the particle crossing. In the analysis this sampling time was set to 60 ns. From this point in time the cluster width was studied as a function of the shaping time. To illustrate the effect of the changing cluster width one event is shown in figure 4.6 with two different shaping times. The cluster width clearly decreases with larger a shaping time, since the influenced signals on the strips out of the center region are integrated out.

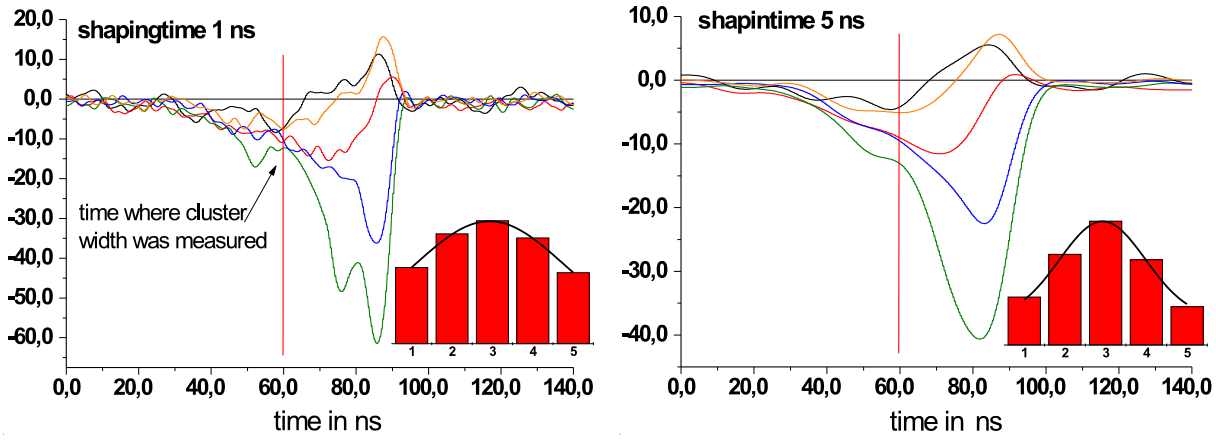

Figure 4.6: Signal of m.i.p. on five neighboring strips. In the offline analysis a shaping of 1 ns (left) and 5 ns (right) was applied. The inserted bar diagrams show the pulse height of each of the five recorded readout strips at the fixed sampling time of 60 ns.

In figure 4.7 the average cluster width (r.m.s.) as a function of the shaping time is illustrated. This shows clearly, that the optimal shaping time is in the order of 15 ns. This value would also fit the time resolution requirement. Longer shaping times increase the pulse length as shown in figure 4.8.

As a conclusion it is important to optimize the filter function and time determination of the electronic system very carefully using the observed pulseshape of the detector and the occupancy and timing accuracy requirements of the application.

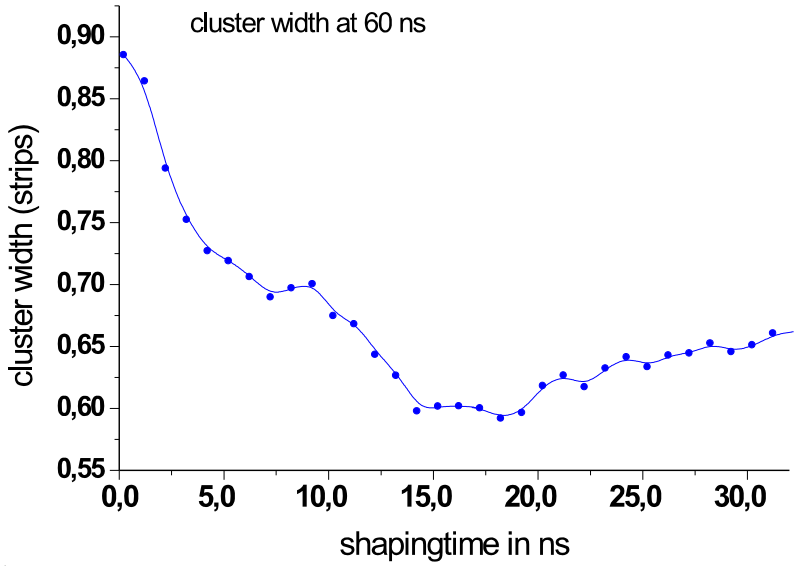

Figure 4.7: Cluster width in strips (σ) as function of the shaping time.

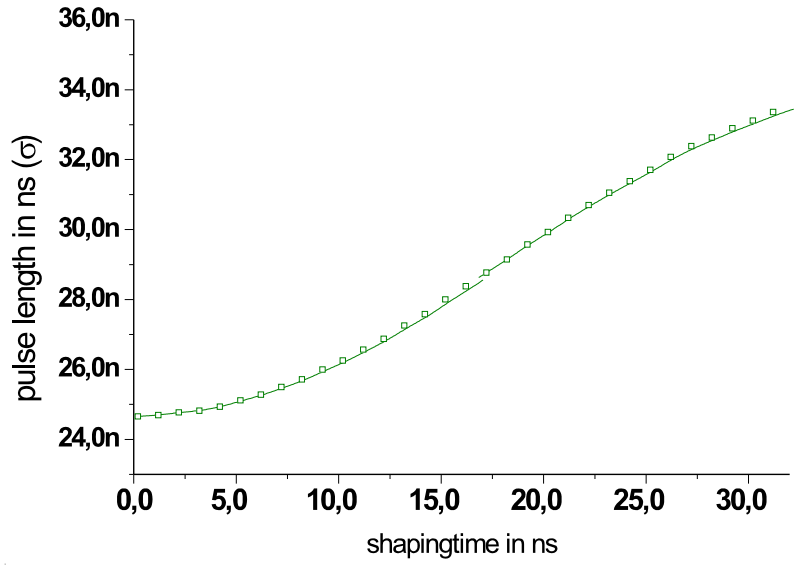

Figure 4.8: Pulse length in time as function of the shaping time.

Chapter 5

Gain calibration with photon pulses

In order to calibrate the detector with photon signals from a radioactive source it is convenient to use an amplifier with a long shaping time (typically 0.5 to 10 μs). With such long integration times (compared to the shaping times required in the LHCb experiment) the thermal and common mode noise are small enough to observe detector pulses without any further filtering stage on the signal. Also the readout trigger can be generated from the signal itself.

5.1 Amplifier calibration

Before measuring the gas gain of the detector the gain of the amplifier was calibrated. Here a Ortec 142 preamplifier and a Ortec 572 or Ortec 454 mainamplifier [28] were used.

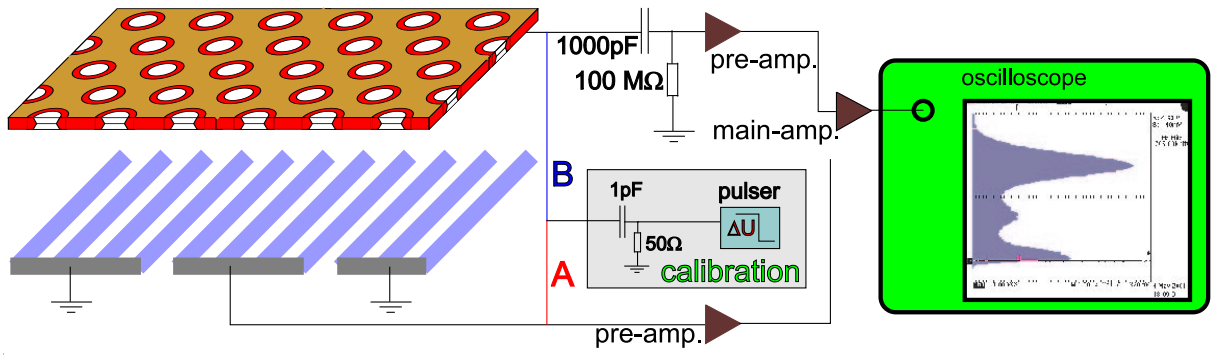

Figure 5.1: Readout scheme for gain calibration. The signal is obtained either from the anode strips or the GEM foil. Only the last of the three GEM foils from the Triple GEM detector is shown. The pulse for calibration of the amplifier was given to the anode (line A) or the bottom GEM side (line B) respectively.

With a pulse generator a square wave was given on a defined capacitance of 1 pF. For an amplitude $\Delta U = 100\,mV$ of the square wave the amount of charge deployed on the anode strips is $\Delta Q = C \cdot \Delta U = 1 \cdot 10^{-12}\,f \cdot 0.1\,V = 100\,fC$ (see figure 5.1 line A).

The amplifier returns a pulse height which linearly depends on the applied charge ΔQ. For a linearity check several points with different ΔU were taken resulting the calibration curve for the amplifier. Changing the capacitance of the anode, for example by grouping more anode strips together, changes the amplifier response and a new calibration has to be done.

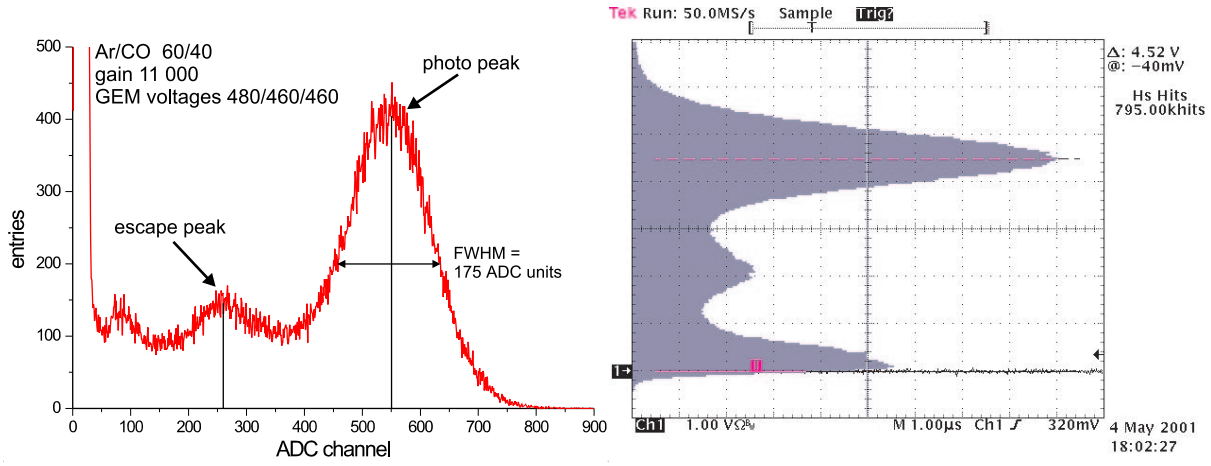

Figure 5.2: left: ^{55}Fe spectrum from the first prototype. The signal was taken from 10 grouped anode strips (histogramed with a peak ADC). right: Spectrum from the third prototype where the signal was obtained from the last GEM foil (histogramed with an oscilloscope, x-axes entries, y-axes pulse height).

A typical spectrum recorded with a ^{55}Fe source can be seen in figure 5.2. In the **photo peak** of the spectrum the complete energy of 5.9 keV from the ^{55}Fe photons was converted into electrons and amplified. This resulted in 220 primary electron-ion pairs. With the calibration curve of the amplifier and the position of the photo peak in the spectrum the charge collected by the anode was calculated. This charge divided by $220 \cdot 1.6 \cdot 10^{-19}$C (charge from the primary ionisation) gives the effective gain.

On a readout board with a typical pitch of 400 μm the signal is distributed over several anode strips as the typical cluster width is about $\sigma \approx 300\,\mu m$. To observe a photo peak at the correct position the complete charge has to be collected. For this reason several anode strips have to be grouped to collect the complete charge.

The detector gain as a function of the GEM voltage for the first prototype is shown in figure 5.3. Gain curves for the second and third prototype can be found in section 9.3.

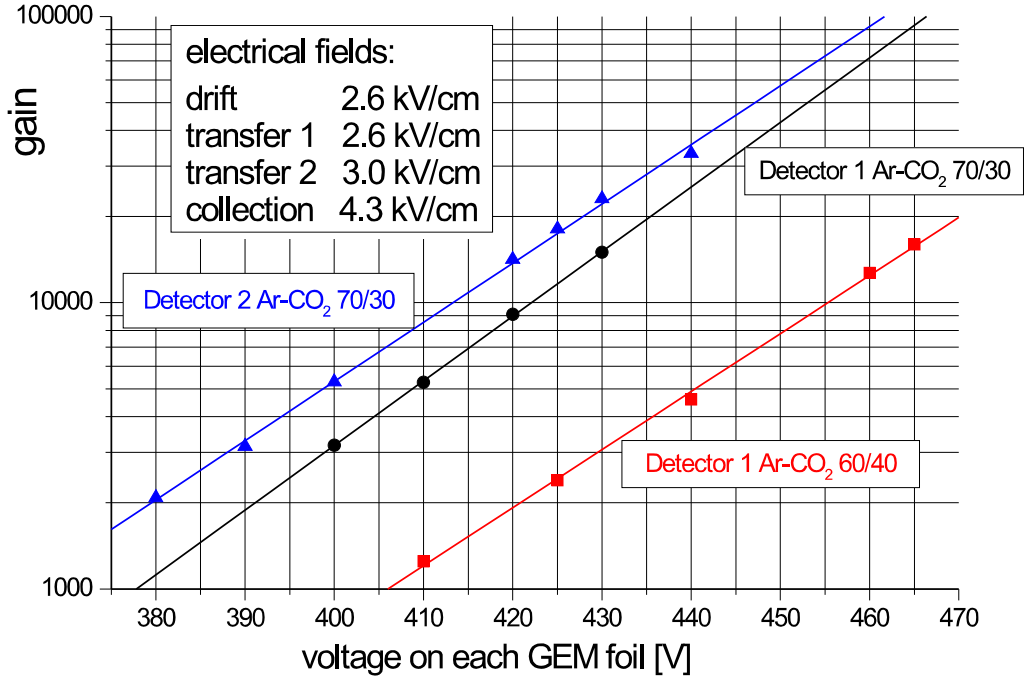

Figure 5.3: Gain curves for two detectors of the first prototype. Ar/CO_2 60/40 and 70/30 mixtures were used as counting gas. The signal was obtained from five grouped anode strips. GEM hole parameters: pitch 140 μm, copper hole 95 μm, Kapton hole 55 μm

5.2 Signals from the GEM foil

The signal on the anodes is induced by the moving charge from the last GEM foil. Alternatively the same signal with opposite polarity can also be observed on the GEM foil. For example in regions where already a different amplifier is connected to the anodes this can be a useful feature. Further the signal of the GEM foil can be used to trigger the readout electronic which is connected to the anodes (self triggering).

The electrical potential of the bottom GEM side was between -300 V and -500 V. To connect the bottom GEM side to an amplifier a AC-coupling was inserted, using a capacitance between the bottom GEM side and the amplifier input (see figure 5.1). The coupling capacitance has to be large compared to the parasitic capacitance between the GEM foil and the signal ground. The charge from the moving electrons is shared between the coupling capacitance and the parasitic capacitance. This has to be taken into account for the amplifier calibration. The defined charge pulse for the calibration has to be guided directly to the lower GEM side as indicated in figure 5.1 (line B).

5.3 Predicted ^{55}Fe spectrum

From the ^{55}Fe source the 5.90 keV photons and 6.49 keV Mn photons were used for the calibration signal. The 5.90 keV photons are 8.53 times as abundant as the 6.49 keV photons as shown in figure 5.4.

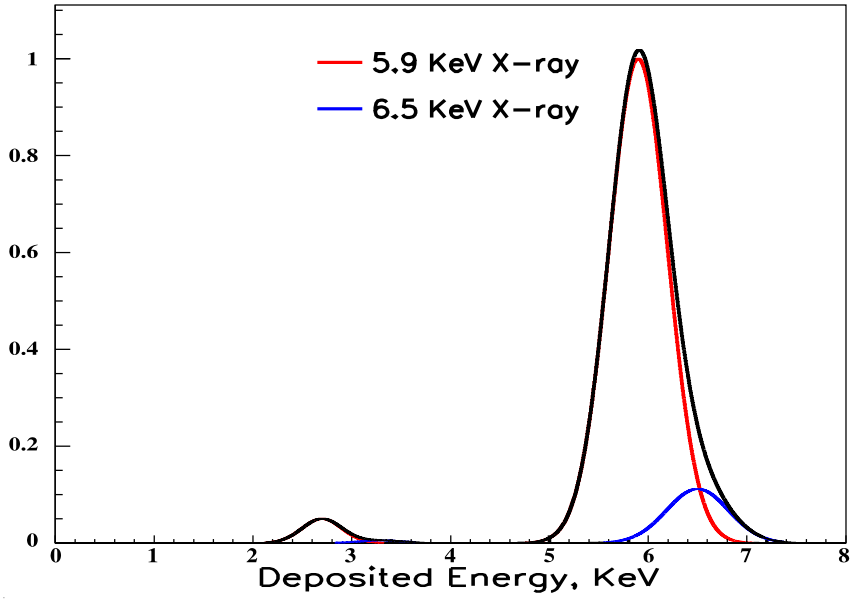

Figure 5.4: Predicted ^{55}Fe spectrum, assuming a statistical fluctuation of the primary ionization of 7% (200 electrons) [29].

In the photoelectric absorption process, a characteristic photon is emitted by the absorber atom in the counting gas (argon). The binding energy of the argon K-shell is 3.21 keV, so the ejected K-shell electron has 2.69 keV left after absorbing the 5.90 keV photon. The range of a 3 keV electron in the gas is about 200 μm.

The electron which wants to drop down and fill the K-shell can emit electrons (Auger Effect) or a photon. If this photon is absorbed near a detector surface it might escape and stay undetected. The energy deposited in the detector is decreased by the energy equal to the photon energy. Therefore a new peak, the **escape peak** will appear. It is located at a distance equal to the energy of the characteristic photon below the **photo peak** (see figure 5.4).

A common method to define the energy resolution is to divide the FWHM of the photo peak by the position of the photo peak. With the corresponding values of figure 5.2 one obtains an energy resolution of 32% for the first prototype and 30% for the third prototype.

5.4 Gain homogeneity

Local gain variations of the GEM foils can be caused by the manufacturing of the GEM foils. The etching masks for the holes on both sides of the GEM foils had to be aligned with a precision of some μm. Due to the large size of the GEM foils variations of the alignment and inhomogeneity in the Kapton hole diameter occurred.

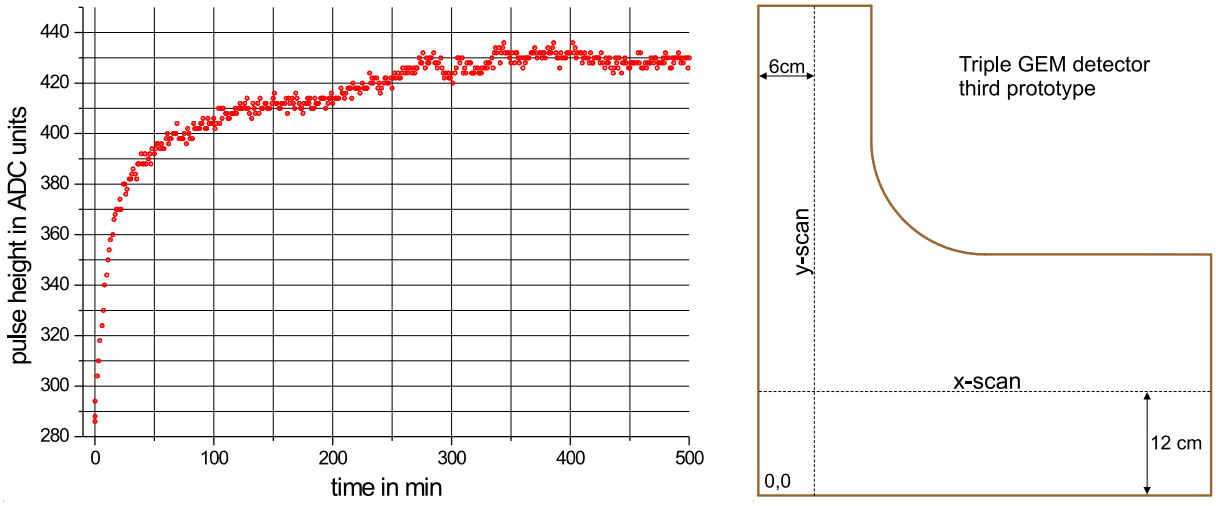

Figure 5.5: left: Increase of the gas gain during irradiation with photons from a ^{55}Fe source. The position of the photo peak as a function of time is plotted. right: The trace for the x and y scan on the detector.

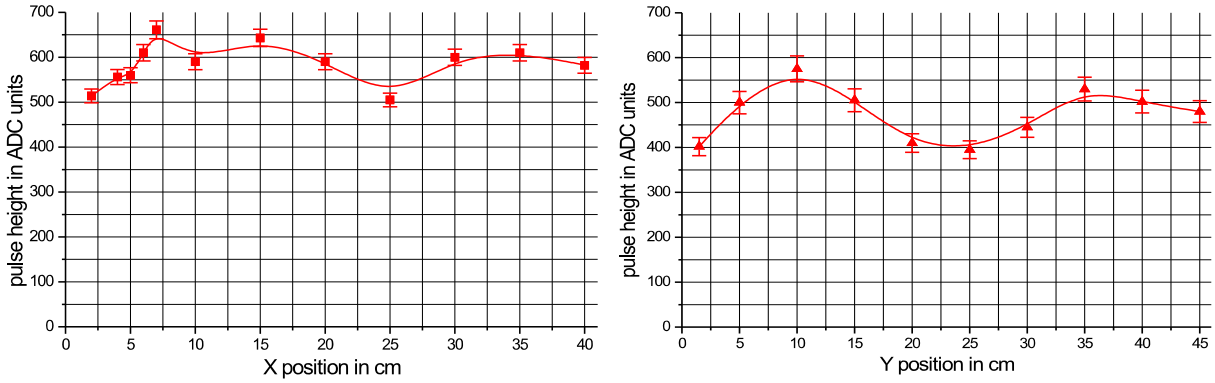

Figure 5.6: Homogenity scan in x and y direction over the third prototype.

To study the gain variation of the detector resulting from regional variations of the GEM hole parameters a homogeneity scan was performed with photons from a ^{55}Fe source. The detector pulses were obtained from the bottom GEM side as described in section 5.2.

The Kapton in the GEM holes charges up while the detector is operated. During the charging up an increase of the gas gain was observed. The time until a stable gas gain was achieved depended on the irradiation intensity. In the high intensity PSI beam, charging up times in the order of seconds were observed. With a low intensity photon source, charging up times of several hours occurred (see figure 5.5 left). It took several hours for every point of the homogeneity scan until a stable gas gain was achieved.

The result of the scan can be seen in figure 5.6. Gain variations of $\pm 30\%$ were observed. The position for the x and y scan on the detector is indicated in figure 5.5 (right).

Chapter 6

Construction of detector prototypes

Several types of triple GEM detectors were built and tested. A description of the manufacturing procedures including the gluing techniques are given in the following chapter.

6.1 Clean room

A careful handling and adequate environmental conditions during the manufacturing are mandatory for the running stability of the detector. The assembling of detectors was always done in a clean room (clean room class 100). Everyone who worked at the detector had to wear clean room clothes, gloves, mouth and hair protection.

All materials used for assembling were cleaned with acetone and alkohol using clean room cloth. Afterwards they were flushed with clean nitrogen. For the GEM foil it is important not to touch the sensitive area. Before assembling a GEM foil it has to be fixed on a frame and flushed intensively with nitrogen (gas pistol 5 bar) to remove dust from the transport.

6.2 HV test of GEM foils

To ensure that only functioning GEM foils were assembled in the detector the GEM foils had to pass a high voltage test. This test was performed in a plexiglass box that was flushed with nitrogen. The voltage applied to the foils was increased continuously during roughly two hours until sparking started somewhere between 580 V and 650 V. The GEM foils were kept sparking about twenty times before decreasing the voltage again. This was done in order to make sure that dust possibly trapped in the GEM holes would burn out without generating a short circuit between the GEM surfaces. The current at 500 V was typically below 10 nA.

6.3 Glues

All gluing were done using the following glues:

- **Epo-Tek 302-3M** is a two component epoxy that cures at room temperature within 10 hours. The pot live time is about 2 hours. The glue is clear and has a low viscosity. It has a low water absorption (0.075 %). The third prototype was completely glued with this glue.

  For the gluing of the spacers (see chapter 6.7) a good attachment between the spacer and the copper spot on the GEM foil was needed. With Epo-Tek 302-3M the best results were achieved. The attachment between the fiber glass epoxy frames and the Kapton of the GEM foil was just tolerable.

- **Epo-Tek H72** is a two component, electrically insulating epoxy. It is a smooth, free flowing paste. For curing it was put in the oven for 3 hours at 70 °C.

  The first and the second prototype were glued with Epo-Tek H72. Two Kapton foils glued together with this glue can not be torn apart [30].

6.4 First prototype

In the HERA-B experiment MSGCs with a GEM foil as preamplifier are used. For the first triple GEM prototype the GEM foils, frames, drift electrodes and the mechanical tooling were used that were designed for the HERA-B experiment. A schematic drawing of the first prototype detector is illustrated in figure 6.1.

The active area of the GEM foils was 23 cm × 25 cm. For this first prototype all gaps were set to 3 mm to avoid any contact between the foils. Due to the large gaps no additional spacers were required. The GEM foil parameters were: pitch 140 μm, copper hole diameter 95 μm, Kapton hole diameter 55 μm. The charge released from the last GEM foil was collected by a printed circuit board with strip pitch of 500 μm and a strip width of 300 μm.

The assembling was performed in the Physics Institute of the University Heidelberg. The glueing procedure started from the drift electrode which consisted of a single sided copper cladded Kapton foil (125 μm). The Kapton foil was glued to a 200 μm thick fiberglass epoxy sheet (FR4). This was done to ensure the mechanical stability of the drift electrode.

On the first frame the glue (Epo-Tek H72) was applied with a gluing machine [31]. The gluing machine had an injection needle which was moved on a XY-table. The amount of glue on the drift electrode was adjusted by the pressure in the needle, the needle diameter and the moving speed. This prevented that surplus glue could flow in the detector. After applying the glue on the first frame it was put onto the drift electrode.

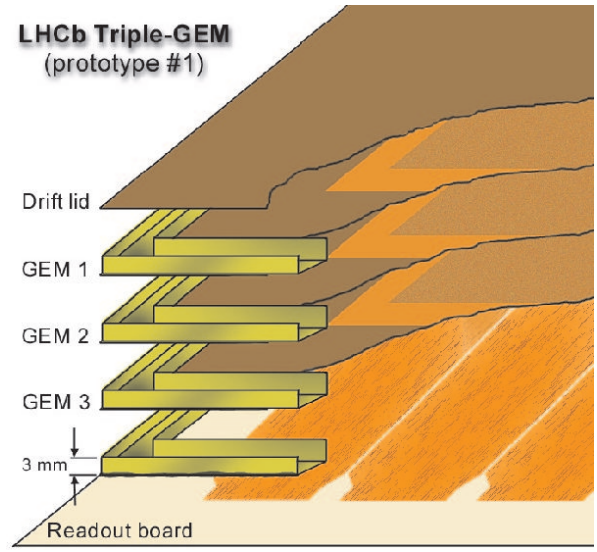

Figure 6.1: Schematic drawing of the first triple GEM detector. The four frames have grooves for the gas supply.

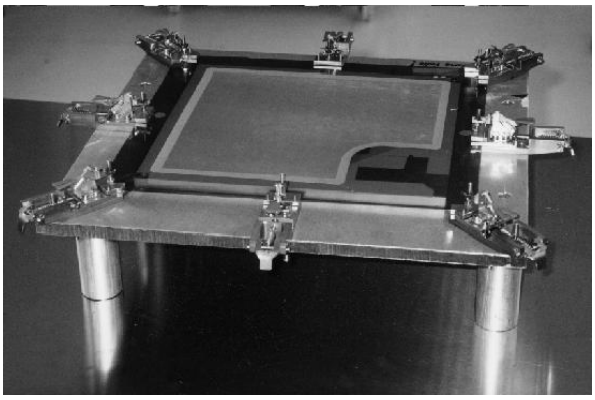

Figure 6.2: Picture of the HERA-B GEM stretching device. Eight clamps keep the GEM and stretch it with springs.

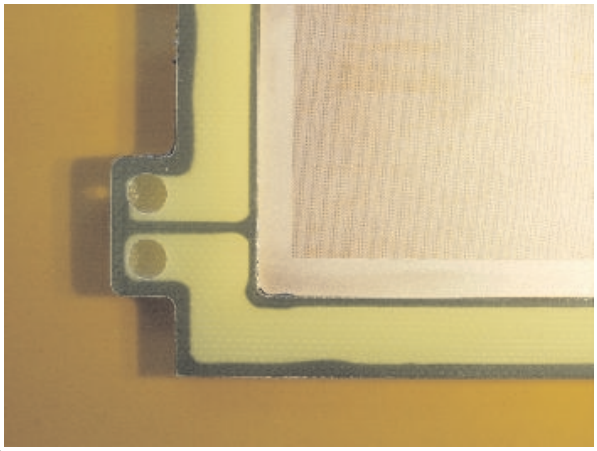

Figure 6.3: Detector frame which also provides the gas distribution. The two drills enable the gas flow between the frames.

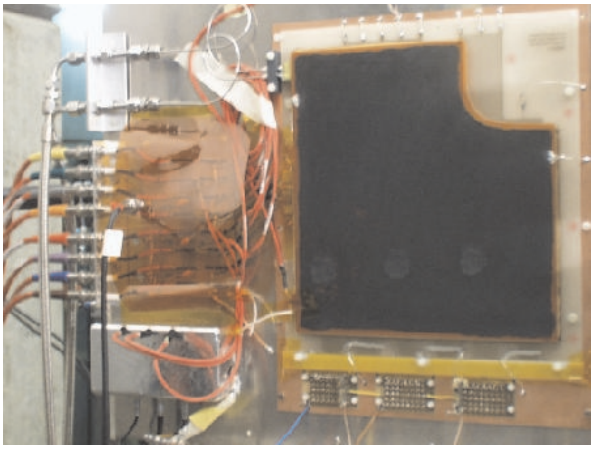

Figure 6.4: Picture of the first prototype. On the left side of the detector the high voltage and the gas distribution can be seen.

In the next step the glue was applied on the other side of this frame. The first GEM foil was stretched (see figure 6.2) and pressed on the frame. The GEM foil was aligned with respect to the frame with the help of alignment marks on the GEM foil. After hardening the first glued components in the oven the GEM foil had to pass again a high voltage test. The next two frames with the GEM foils were glued in the same way on top of the

first GEM foil. Finally the sandwich of three GEM foils and four frames was glued onto the readout board. The positioning was done by hand with the help of alignment marks on the readout board.

Small holes in the frame ensured the gas distribution. Each frame consisted of two parts, a U-profile and a top, building a channel for the gas flow. A picture of the frame can be seen in figure 6.3. Small holes in the inner side of the frame provided the gas flow into the detector. The gas channel in the frame was connected to a 2 mm stainless steal pipe for the gas supply. Two large drills in each frame enabled the gas flow between the frames.

For the first prototype GEM foils with a single unsegmented copper surface on each side were used. For the high voltage powering a 5 MΩ series resistor was connected to every GEM surface to limit the current in the case of a discharge. In total seven different voltages were needed to operate a triple GEM detector. All voltages were delivered by individual power supply channels. These power supplies are described in chapter 10.3.

A picture of the complete assembled detector with the external high voltage and gas distribution is shown in figure 6.4.

6.5 Second prototype

The second prototype had an active surface of 30 cm × 23 cm, whereas the anode strips had a length of 30 cm. The final shape and size of one Inner Tracker station of the LHCb experiment was not fixed at that time. However, in the Technical Design Report a maximum strip length of 30 cm was assumed for the LHCb Inner Tracker.

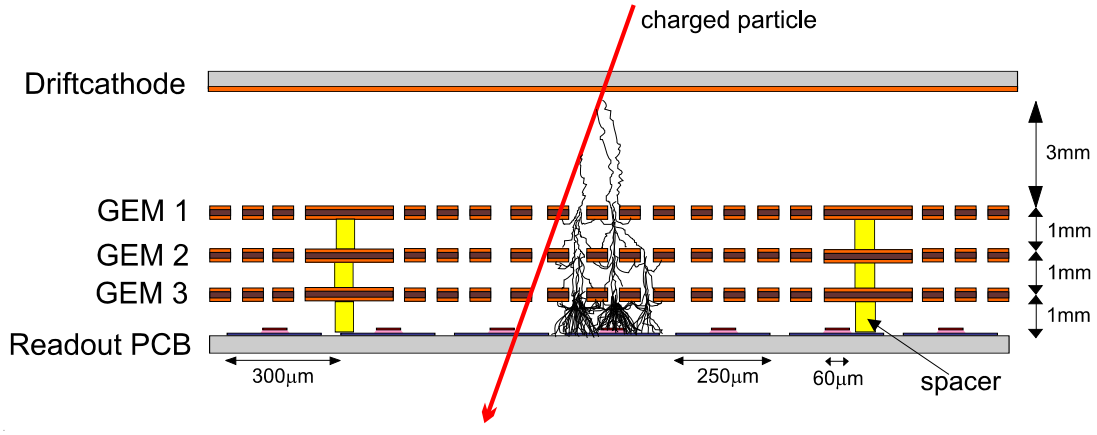

Figure 6.5: Schematic view of the detector with three GEM foils, which are separated by 1 mm gaps using spacers. Pitch and width of the strips on the two coordinate readout board are also shown.

The transversal diffusion of the electron cloud in the transfer gaps is the dominant contribution to the cluster size (see chapter 9.5). To minimize the occupancy in the detector a small cluster size is mandatory. To obtain small clusters the transfer gaps were reduced from 3.0 mm to 1.0 mm. This narrow gaps made it necessary to put spacers between the GEM foils to avoid a contact between the GEM foils due to electrostatic attraction. For the parameters of the GEM holes a standard GEM was used as described in section 3.1.

Furthermore a two dimensional readout structure and segmented GEM foils (see below) were implemented for the second prototype. A schematic drawing of this detector can be be seen in figure 6.5.

To build this detector 2 readout boards, 10 GEM foils, 4 drift electrodes and several frames were ordered. The material cost was 7'600 SFR.

The detector was assembled in the Physics Institute of the University Zürich. The gluing procedure started again from the drift electrode. The drift electrode consisted of a 50 μm thick Kapton foil covered with a layer of 15 μm thick copper. An aluminum frame was glued with Epo-Tek H72 onto the Kapton side and a 3 mm FR4 frame onto the copper side simultaneously. The aluminum frame was required to assure mechanical stability of the detector.

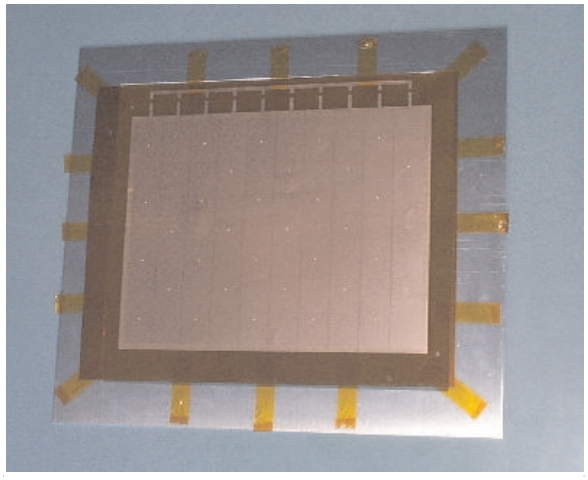

Figure 6.6: A GEM foil stretched with tape to a large auxiliary aluminum frame beforegluing.

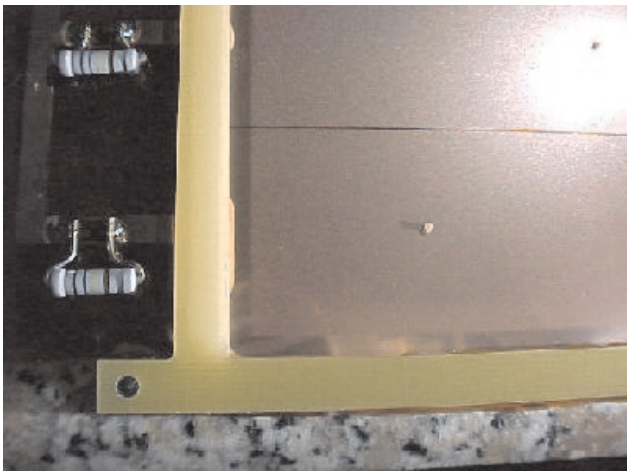

Figure 6.7: HV resistors connected to GEM segments, 1 mm G10 frame and spacer. The 4 mm copper surrounding of the GEM can also be seen.

The GEM foil was stretched by putting it onto a large aluminum frame and pulling it with tape to the sides (figure 6.6) with the spacers already in place. Each GEM foil was equipped with 35 spacers (see section 6.7). After passing a high voltage test the first GEM foil was simultaneously glued to the 3 mm FR4 frame on the drift electrode and the first 1 mm frame onto the other side of this GEM foil.

The glue was applied by hand with an injection needle. To avoid that glue flows into the GEM holes at the edge of the GEM foil, the GEM foil had a copper border of 4 mm without GEM holes. The next two GEM foils were stretched, tested and glued in the same way. A photograph of the detector in this state is shown in figure 6.7. The alignment of the frames and GEM foils was done through dedicated holes in the frame. With two alignment pins in the corner of each frame the components were accurately placed. Finally the sandwich structure was glued to the readout board.

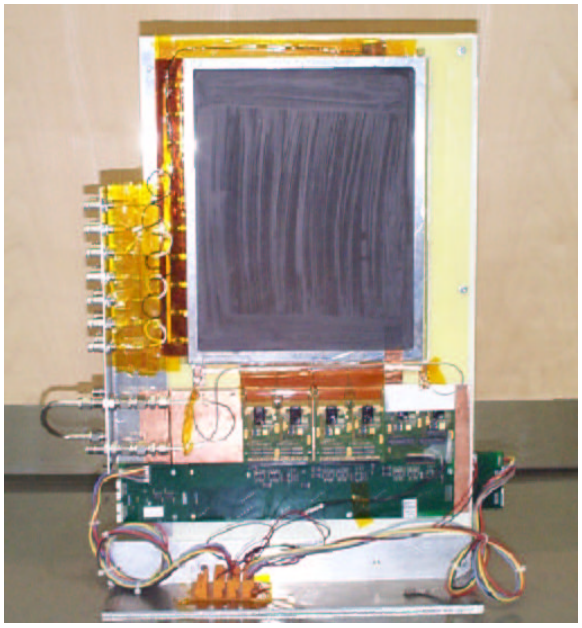

Figure 6.8: Foto of the complete detector with high voltage distribution and readout electronics.

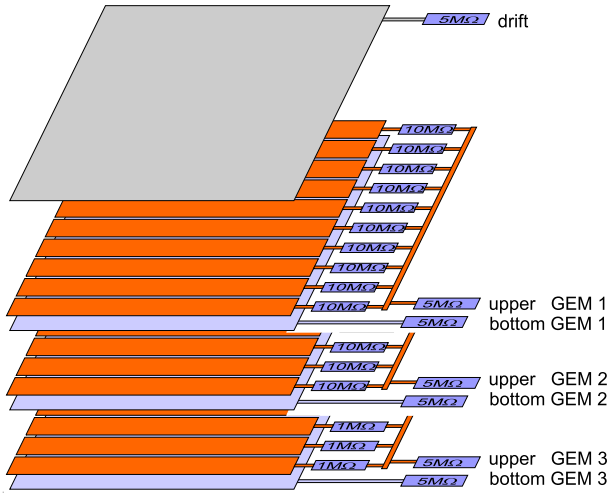

Figure 6.9: HV-schema, each of the seven voltages is delivered by individually controllable power supply channels.

The capacitance between the two sides of a GEM foil was about 30 nF for the first prototype. To reduce the total charge released in a possible high voltage breakdown the GEM electrode was divided on one side into 10 rectangular segments, which were separated by copper free gaps of 200 μm width (see chapter 10.6.4). Each segment was powered through an individual HV-resistor of 10 MΩ and 1 MΩ resistor for the first two and the last GEM foil respectively outside the detector. The segmentation has the additional advantage, that only a small fraction of the detector would fail in the unlikely case of a high voltage breakdown causing a permanent short.

6.6 Third prototype

Detectors of this type were manufactured in IPHE, University of Lausanne and Budker Institute of Nuclear Physics Novosibirsk using the same base material. The main changes with respect to the second prototype were a different shape of the detector. This detector had a L-shape which was the result of an optimization of the detector acceptance to cover the inner most area around the LHC beampipe (see figure 1.5). The active are was 45.0 cm × 41.5 cm. To reduce the occupancy the anode strips were split in the middle. This resulted in a maximal strip length of 20.7 cm and the readout electronic had to be mounted on two sides of the detector. To reduce the strip capacitance a "Zig-Zag" geometry was chosen for the readout board (see chapter 7.3). A standard GEM was used where the number of GEM segments was increased to 100.

The L-shape is mechanical not as stable as a rectangular shape. The tension on the GEM foil leads to a deformation especially in the elbow of the frame. To reduce this deformation the drift electrode was glued on a honeycomb plate. The plate was fixed on a pumping table until the manufacturing of the hole detector was finished.

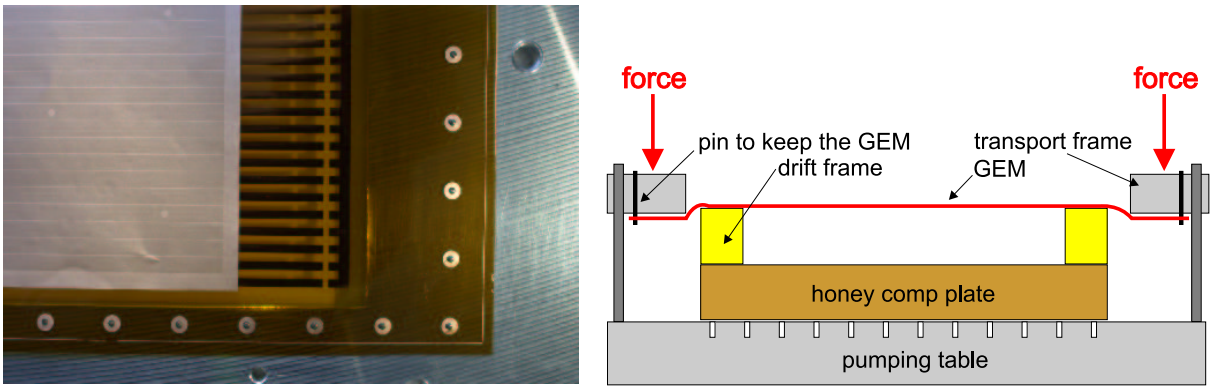

Figure 6.10: left: Aluminum transport frame. The GEM foil was carried by small metal pins in the frame. right: Tooling which was used to stretch and align the GEM foils.

The GEM foil was attached to a big aluminum transport frame. In the border of this transport frame small pins were inserted to carry the GEM foil (see figure 6.10 left). The first GEM foil had 3.0 mm spacers towards the drift gap and 1.0 mm spacers for the transfer gap. The stretching was done by applying force on the aluminum frame while the GEM foil was already positioned on the first frame. A schematic drawing of the stretching procedure can be seen in figure 6.10 (right).

To avoid a thermal deformation while hardening the glue in the oven, Epo-Tek 302-3M was chosen that hardens at room temperature. The size of the copper surrounding of the GEM foil was reduced from 4 mm to 2.5 mm. In this way the inactive area around the LHC beampipe is reduced.

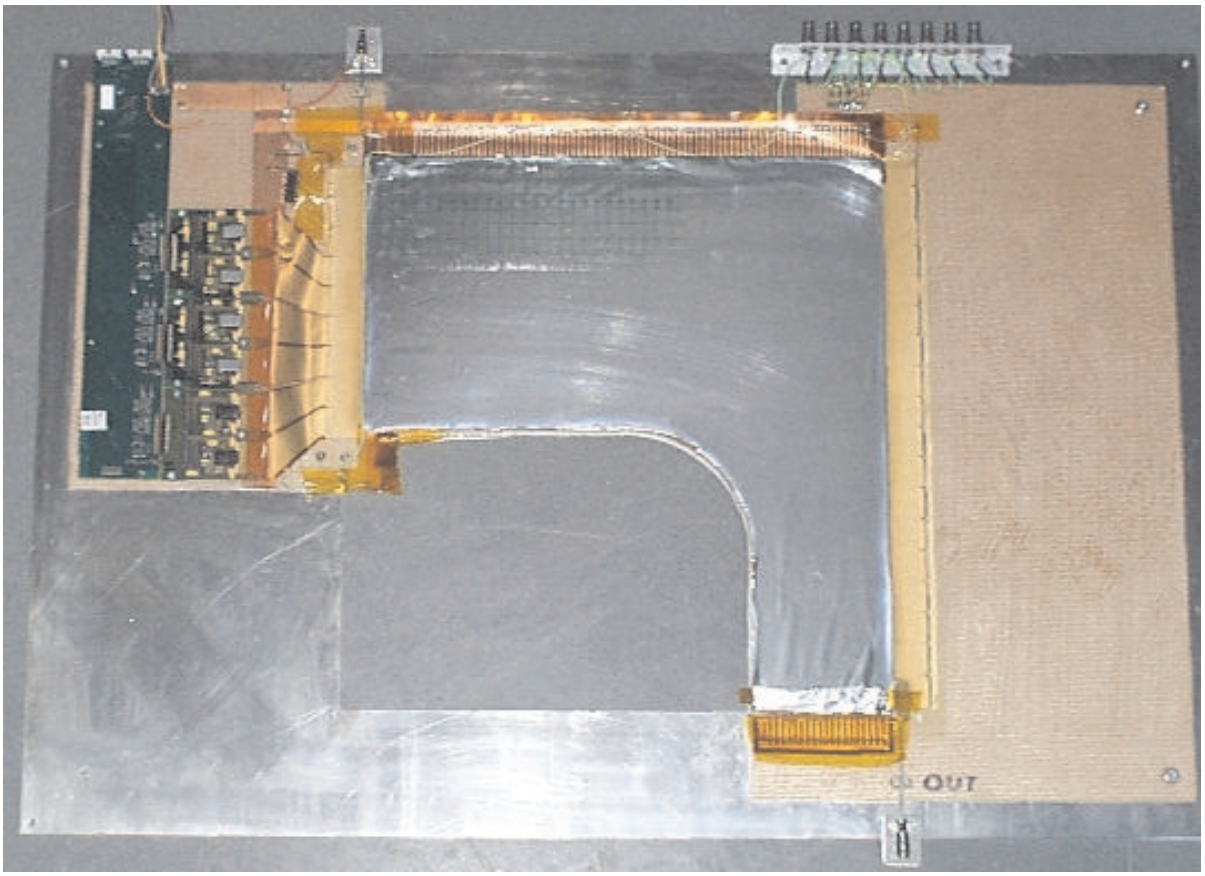

Figure 6.11: Picture of third prototype. On the left side the readout electronic can be seen.

The glue was applied using a pencil. Unfortunately as a consequence of this technique air bubbles remained between the GEM foil and the frame. With a gas leak hunter, leaks around the frame were detected. These gas leaks were sealed by applying additional glue around the detector with a pencil.

6.7 Spacers

Due to the electric field between the GEM foils they attract each other. An equal distance of the gaps between the GEM foils was therefore not guaranteed. Because of the very stiff copper layer on the GEM foil a high tension was needed to stretch the foil. For large detectors the frames were not stable enough to take the force. A more stable frame would increase the material budged and reduce the radiation length. To overcome this problem the GEM foil was stretched just to be flat and spacers were inserted between the GEM foils.

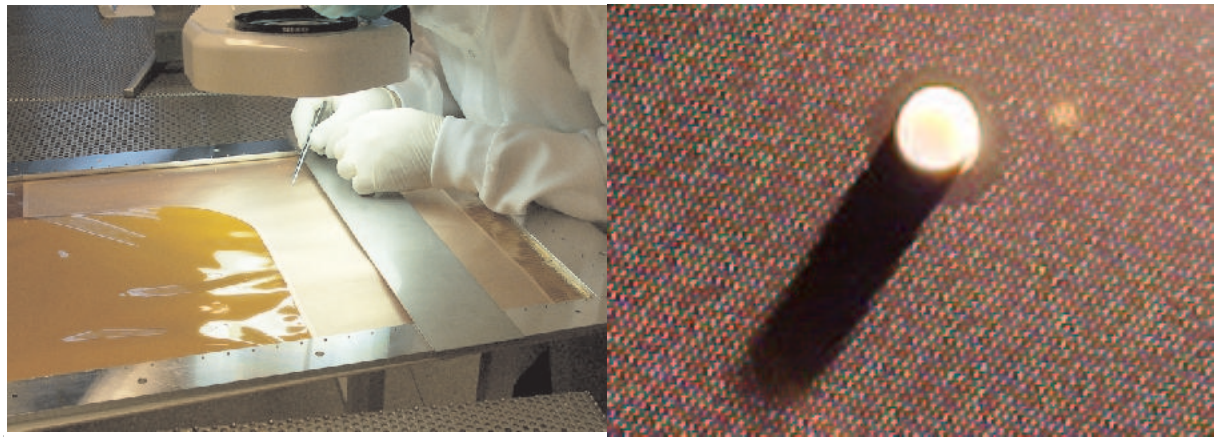

Figure 6.12: left: Positioning of the spacers in the clean room. right: A single spacer glued onto the GEM foil on the especially intended copper spot.

The spacers were small cylinders with 1.1 mm diameter and a height 1 mm of pure epoxy resin (Epo-Tek H72). They were produced in the mechanical workshop of the University Zürich. To produce spacers with a height of 1.0 mm an aluminum plate of 1.5 mm thickness was used as base material. An array of drills with a diameter of 1.1 mm was machined into this plate. On a table a smooth surface was prepared with a non adhesive paste. On this surface epoxy resin was applied and the aluminum plate with the drills was pressed into it. To get rid of air bubbles in the drills, the setup was exposed to vacuum for some minutes. After hardening both sides of the aluminum plate were milled to a remaining height of 1.0 mm. Unfortunately the filling epoxy Epo-Tek H72 contained ingredients which lead to a fast damage of the milling tools. Finally the aluminum was removed in a natrium hydroxide solvent.

The positioning of the spacers on the GEM foil was done by hand under a microscope. This procedure took about 1 hour per foil. Since HV breakdown problems may occur due to unintentionally deposited glue in the GEM holes, the GEM foils of the second and third prototype contained 2 mm diameter regions without holes for gluing the spacers (see figure 6.12).

The total fraction of inactive surface of the detector due to spacers was $1.6 \cdot 10^{-3}$, however the inefficiency introduced is expected to be even smaller, since typical charge cluster diameters resulting from particle tracks are of order 0.5 mm.

6.8 Remarks on the construction

The first and the second prototype were glued using the Epo-Tek H72 epoxy wich had to be hardened in the oven. During the positioning of the spacers on the GEM foil of the second prototype some glue dropped on the sensitive area of the GEM foil. However both detectors showed a low discharge probability (see chapter 10.8).

The third prototype was glued using Epo-Tek 302-3M. Also for this prototype some glue dropped on the sensitive area of the GEM foil. These detectors however showed an early breakdown in a hadronic environment. This difference in discharge probability might be attributed to the different types of glue.

Nearly all prototypes had gas leaks at the edges of the detectors. To realize an accurate and stable attachment of the GEM foil to the fiber glass epoxy frame, is still an unsolved and major problem of GEM detectors. In large scale applications the problem of assembling a GEM detector is often disregarded. The reliability of a GEM detector crucially depends on the accurate construction. In my opinion this is the reason why GEM detectors recently lost in favour of silicon strip detectors.

Chapter 7

Readout structures

The separation of the amplifying stage from the readout stage in GEM detectors allows to use any readout pattern that is appropriate for the application. The amplification takes place in the GEM foils while the readout board simply collects the charge. One and two dimensional readout boards were tested.

7.1 Stripline

The readout board of the first prototype (see chapter 6.4) had gold plated copper strips on a fiberglass laminate (0.22 mm G10). The manufacturing of the board is a well known standard technology in printed circuit board industry. Three different combinations of strip width and pitch have been fitted on one board. The simplest type was made of 200 μm wide strips and 500 μm pitch.

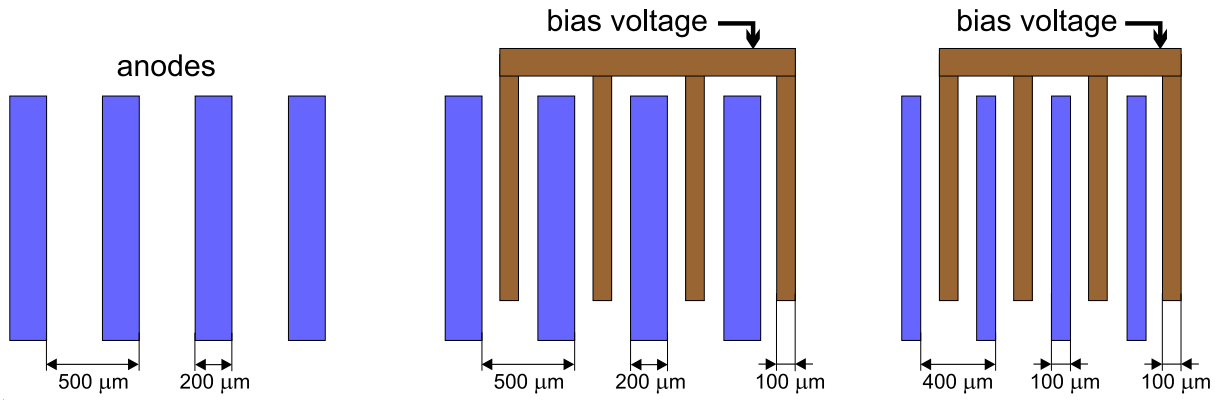

Figure 7.1: Schematic drawing of the three readout structures tested in the first prototype.

For the other two sections alternating anode cathode geometries were chosen in order to study the effect of guiding the electrons more efficiently to the anodes. A few ten volts between the anodes and the cathode strips were applied. However the pure anode structure proved to be sufficient. From an initial charging up of the insulating gap between two anodes a similar effect as from the guiding electrodes is expected.

7.2 Two dimensional readout

For the particle tracking in the LHCb experiment stereo views of $\pm 5^\circ$ are required (see chapter 1.3). This can be achieved by using either two detectors or one detector with a two dimensional readout board. A detector with two dimensional readout has the advantage that the total detector material is reduced and hence the radiation length is improved.

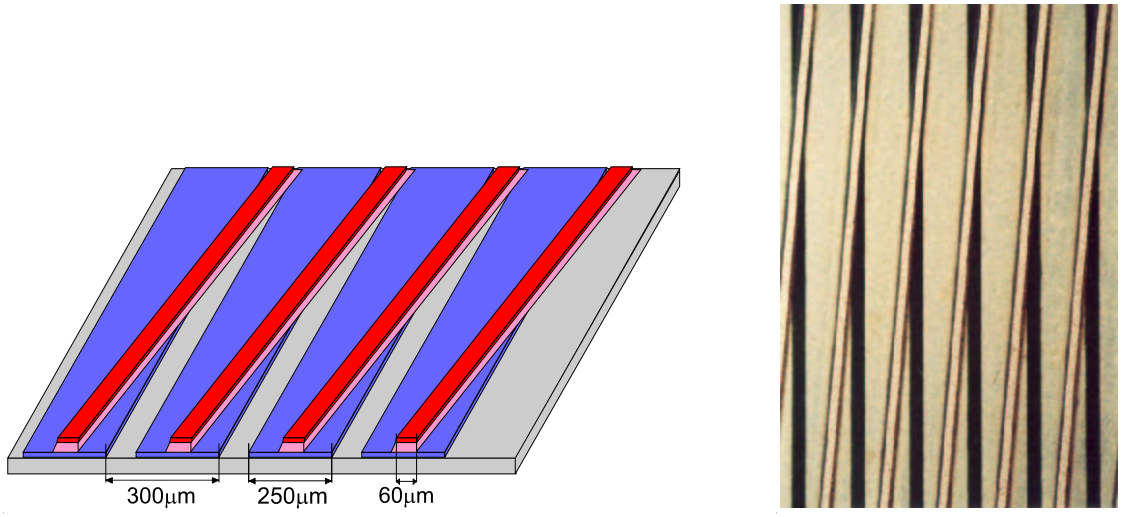

Figure 7.2: left: Schematic drawing of the readout board. Pitch 300 μm, upper strip width 60 μm, lower strip width 250 μm. right: Microscopic close up of the readout board.

Other groups already tested two dimensional readout boards [32][33]. For the second prototype a detector including a two dimensional readout board was built, with a stereo angle of 5° between two sets of parallel strips. The rotated strips on the top were separated by a 50 μm thick Kapton layer from the lower strips (see figure 7.2). This readout board was manufactured from copper cladded Kapton foil with the same etching technology as the GEM foils in the CERN workshop. It was glued to a 100 μm thick FR4 sheet to ensure a reasonable flatness. Below the readout board a 4 mm thick Rohacell plate was mounted covered with a grounded aluminum foil, which acts as an electrical shield.

The lower strips have to be wider than the upper strips in order to collect in average an equal amount of charge on both layers (charge sharing). To reduce the interstrip

capacitance the strips have to be made as narrow as possible. A natural limitation for the width is the feature size of the technology, that is about 50 μm. Thus the width of the top strips was chosen to be 60 μm. The bottom strips had a width of 250 μm. A pitch of 300 μm for each plane was chosen for practical reasons to connect the printed circuit board to a HELIX front end chip using an existing p.c.b. designed for a 300 μm pitch. The strip length was 30 cm.

7.2.1 Charge sharing

As top and bottom strips were separated by 50 μm and the signal is induced by the moving charge which drifts from the last GEM foil through the collection gap, the bottom strips were implemented wider than the top strips to obtain a well balanced charge sharing. In figure 7.3 the correlation between the pulse heights of the two readout coordinates is shown. The data were taken with the second prototype during a test beam at the PSI. In average the signals on the upper strips were ~ 1.05 times larger than those of the lower ones.

7.2.2 Capacitance of the two dimensional readout board

The capacitance of the ceramic fanin of the HELIX board was measured to be 2 pF (see chapter 8). The total capacitance of the fully mounted system of one strip to all its neighbor strips and the full electrical environment was measured by coupling a square wave pulse to the readout board (still connected to the HELIX) through a 1 kΩ serial resistor. From the observed rise time of this pulse ($t_{10\%-90\%} = 190$ ns) a strip capacitance of 86 pF was determined.

By coupling a well defined charge to a readout strip the HELIX gain was measured to be 880 electrons/mV in this configuration. The noise level of the HELIX chip was measured to be 4.8 mV corresponding to 4200 electrons. The procedure for estimating the noise level is described in chapter 8.4. From this information and the known dependence of the noise from the input capacity (taken from the HELIX data sheet) a total capacitance of the readout board of ≈ 100 pF was derived, which is consistent with the value above.

Such a high noise figures require a large gas gain in order to get a reasonable track efficiency. Also it increases the shaping time of the preamplifiers input due to limited currents in the first integration step of the preamplifier. Therefore every effort should be taken to reduce the capacitance of the readout board as much as possible.

7.3 Zig-Zag geometry

The two dimensional readout board of the second prototype had a capacitance of about 90 pF. This capacitance led to large noise and slow signals. The reason for this is shown

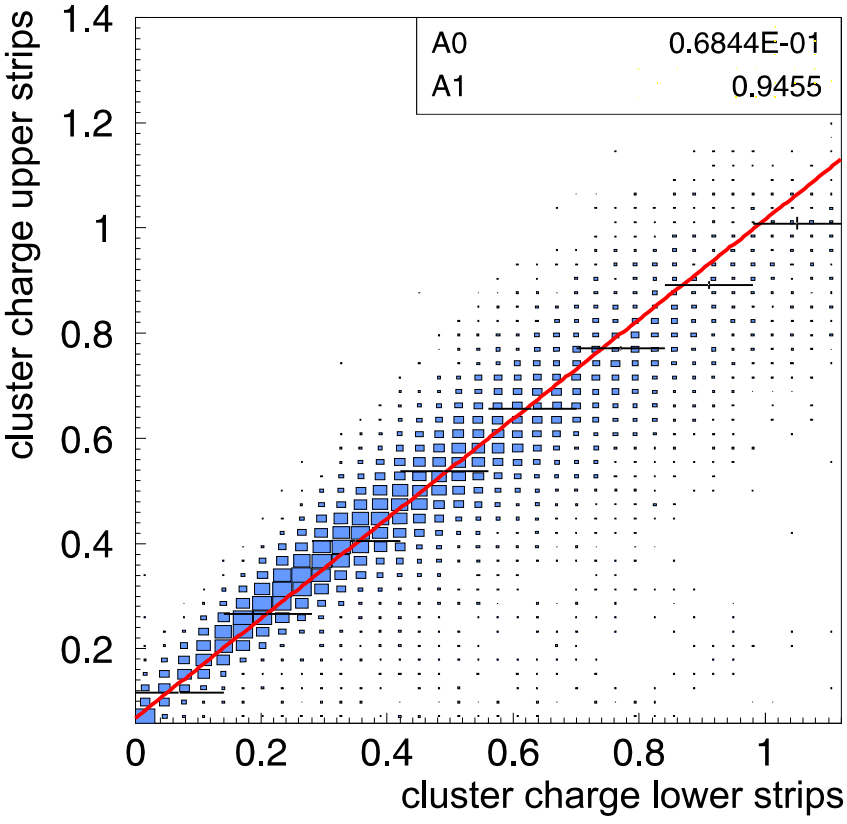

Figure 7.3: Correlation between pulse heights of the lower (U) and upper (V) strips for the second prototype.

in figure 7.2: The top strips run over long distances on top of the bottom strips causing a large coupling capacitance.

For the third prototype a readout board using a Zig-Zag geometry was tested. Here the 0° strips were at the top layer and the small angle stereo strips at the bottom layer. Figure 7.4 shows such a board. The bottom strips were made in short sections parallel to the top ones with narrow bridges connecting the sections belonging to one bottom strip.

In such a layout the area of overlapping regions between top and bottom metal layers is reduced, thus minimizing the interstrip capacitance. Moreover, as the bottom and top strips are mostly parallel, the sharing of induced charge between the layers will be constant and will not depend on the position along the strip. This was not the case for the layout with straight stereo strips.

The Zig-Zag readout board was designed by the Budker Institute of Nuclear Physics in Novosibirsk. A MAXWELL field calculating package was used to calculate the necessary ratio of widths and strip capacitances. In the calculations a ratio of the signals induced on bottom strips with respect to the top ones of 1.2 was required, in order to compensate

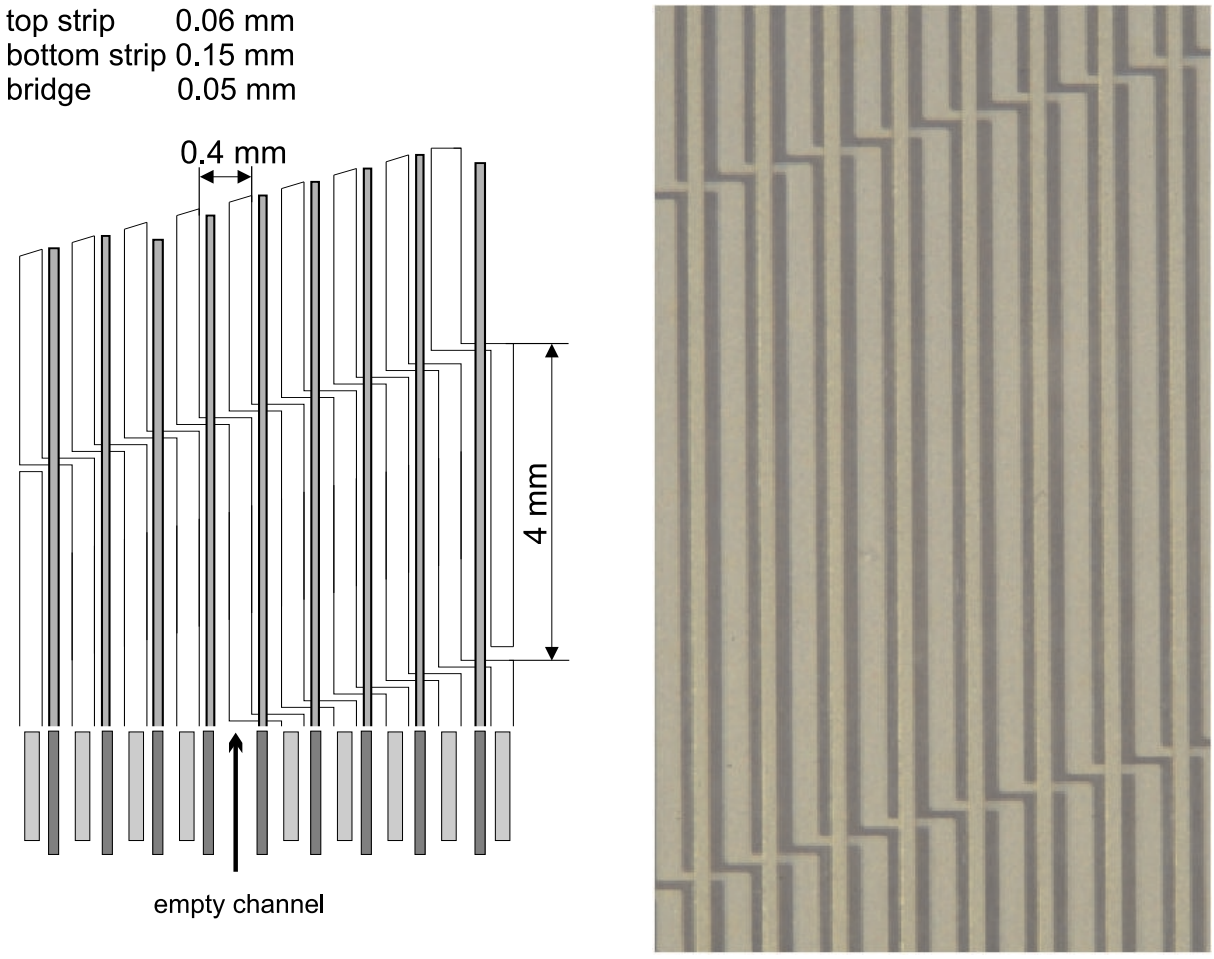

Figure 7.4: Schematic drawing and microscopic picture of a the Zig-Zag geometry readout board.

layer	strip width	pF/cm (calculation)	pF/cm (measurement)
bottom	150 μm	0.62	0.73
top	60 μm	0.32	0.54

Table 7.1: Strip widths and capacitances for the optimized readout board.

for larger capacitance of the bottom strips. The calculations were made for the strip pitch of 400 μm (see table 7.1). More details on the readout board can be found in [34].

A measurement with the third prototype in the PSI beam gave a ratio between signals in bottom and top layers of 1.12 (see figure 7.5). This comes close to the expected ratio bottom/top equals 1.2. The Novosibirsk group found a ratio of 1.0 with a preliminary test readout board [34].

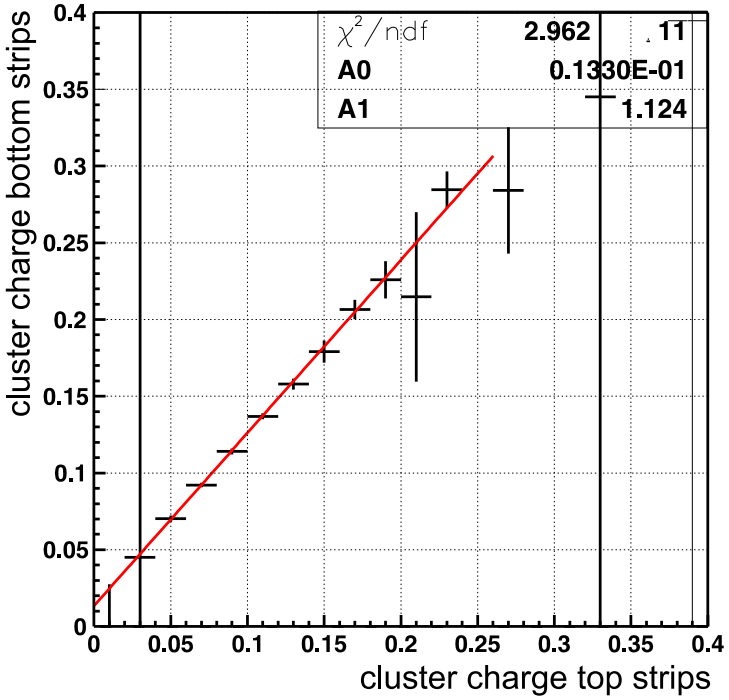

Figure 7.5: Correlation between pulse heights of the lower (U) and upper (V) strips for the third prototype (Zig-Zag geometry).

7.4 Crosstalk

In the LHCb Inner Tracker the readout electronic has to be mounted as far away from the beampipe as possible to reduce the amount of material close to areas with a high particle flux. Because of this reason both coordinates U and V were read out at the same side of the detector. When connecting the readout strips to the electronics, the strips were running some centimeter in parallel (6.5 cm for the second and 8.0 cm for the third prototype). Here cross talk between the two layers occurs. On the U-strips for example the true signal as well as the crosstalk from the V-strips can be observed (see figure 7.6 left). The size of the crosstalk is not influenced by the pattern of the anode structure it depends only on the layout of the connection to the readout electronics.

The relation between the real signal and the crosstalk signal is shown in figure 7.6 (right). The crosstalk signal was about 25% of the real signal. In a hitmap (see figure 7.7) the crosstalk signals show up as a second region of pulses.

As a conclusion, the design of the two dimensional readout boards has to be carefully optimized to minimize crosstalk specially at the connection to the readout electronic.

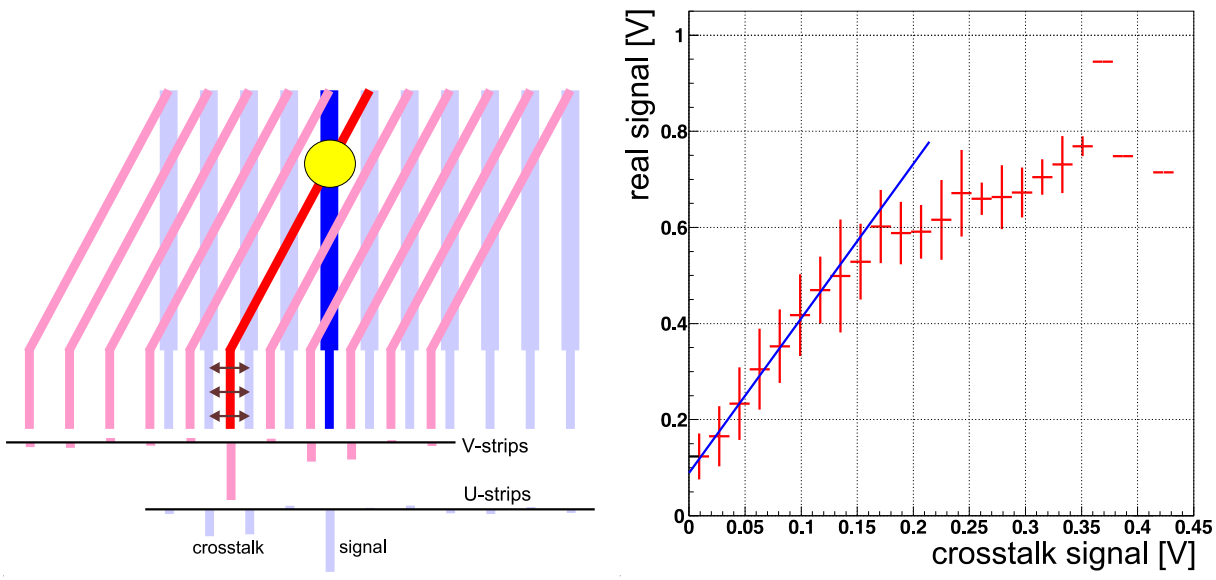

Figure 7.6: left: Schematic drawing of a two dimensional readout board and how the crosstalk signal was created. right: Real signal vs. crosstalk for the third prototype. Above 0.6 V the amplifier saturated.

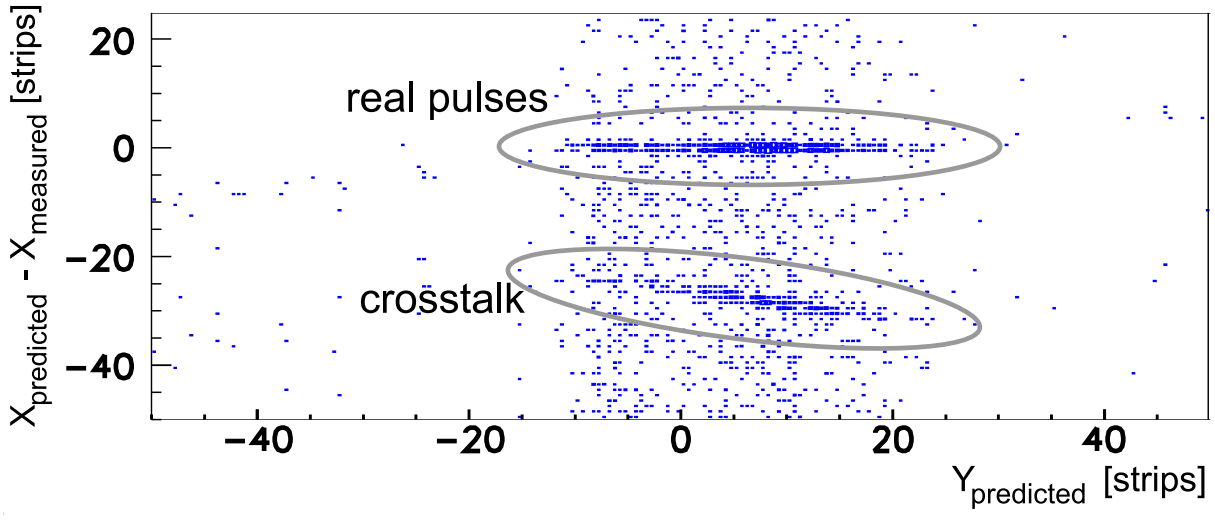

Figure 7.7: Hitmap for all pulses reconstructed in the third prototype.

Chapter 8

Readout with the HELIX chip

Studies on the tracking performance of the detectors were done with the HELIX 128-2.2 readout chip [35], which was originally developed for the HERA-B experiment. The HELIX closely approximates in its analog characteristics the Beetle chip, which will be used later in LHCb [36]. The shape of the preamplifier output of the HELIX depends on the capacitance of the detector connected to the input. For the second detector prototype the pulse shape had a FWHM of about 90 ns.

8.1 Connection to the readout chip

The HELIX analog input pads (pitch 41.4 μm) were wire bonded to a ceramic fan-out. This fan-out was made of thin film ceramics [37] and included a serial protection resistor of 600 Ω for every readout channel to avoid damage of the preamplifier input in case of discharges in the detector (optimized for the HERA-B MSGC operation). The fan-out was connected by a Kapton pitch adapter to the anode strips of the readout board.

Both coordinates of the two dimensional readout board of the second prototype were read out by separate HELIX chips. This is shown in figure 8.1 (left). The Kapton pitch adapter was bonded with Z-bond glue [38] to the anode strips. Z-bond glue [39] is an epoxy which contains nickel particles of 7 - 9 μm diameter size. By putting glue on the pitch adapter and pressing it to the anode strips, the nickel particles make an electrical connection between the strips of the pitch adapter and the readout board. As the interstrip gap on the pitch adapter is large compared to the nickel particle diameter no electrical shorts between adjacent strips are created.

On the third prototype both coordinates were read out by one readout chip. The Kapton pitch adapter was bonded by wire bonding to the anode strips as shown in figure 8.1 (right).

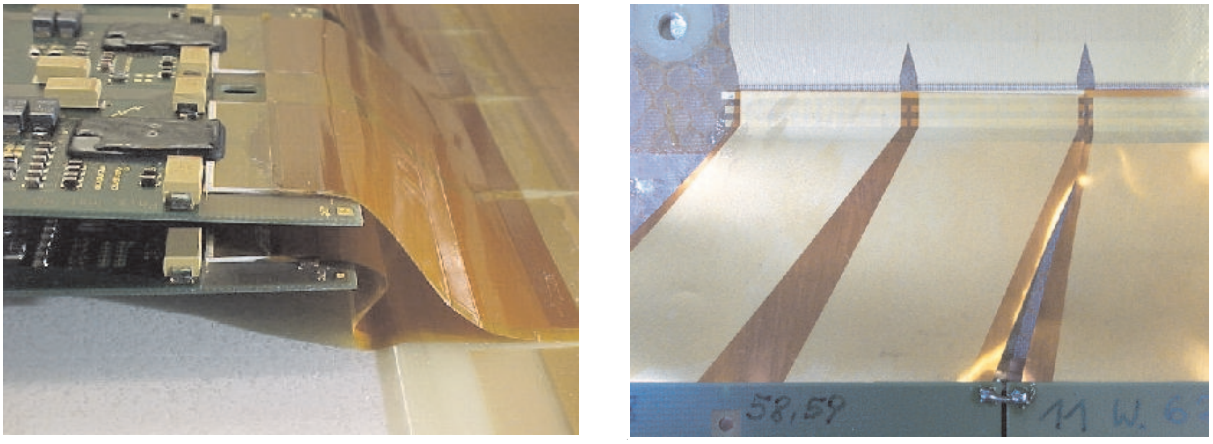

Figure 8.1: left: For the second prototype each layer of the two dimensional readout board was equipped with 4 HELIX chips (= 512 readout channels per layer). Two thirds of the active area of the detector could be read out this way. right: On the third prototype six HELIX chips were wire bonded to the readout board. The connection between the pitch adapter and the readout board is shown.

8.2 Readout chain

The HELIX chip contains programmable registers that have to be programmed. A data pattern containing the register values was generated with a PC. To transmit the data from the PC to the HELIX chip a TTL I/O card was used. The TTL signals were converted into Low Voltage Differential Signals (LVDS) which were needed for the input of the distribution board. For this level conversion (TTL-LVDS) a additional board was built ("Clock generator and Programming" board in figure 8.2).

The HELIX chip uses the same input lines for programming and running the chip. For example the trigger line is combined with the serial data line. For switching between the programming and running signals a Lattice FPGA chip [40] was used located on the clock generator and programming board. Furthermore the 10 MHz readout and sample clocks were generated with a quartz oszillator on the same board.

The HELIX chip samples the amplitudes of the detector signals with 10 MHz and stores the pulseheight of each readout channel in an analog pipeline, which is implemented in the HELIX chip. The 10 MHz sampling clock was not synchronized to the time when the particles traversed the detectors. To sample the signals at their maximum pulseheight the clock generator board sent pulses of 20 ns width and 10 MHz frequency. A coincidence between these pulses and the scintillator trigger was applied. Thus only particles with the correct timing with respect to the sampling clock were selected.

The HELIX chip was run with standard settings [35]. After a trigger signal each HELIX chip sends the analog value of all 128 channels multiplexed via one readout line (differential

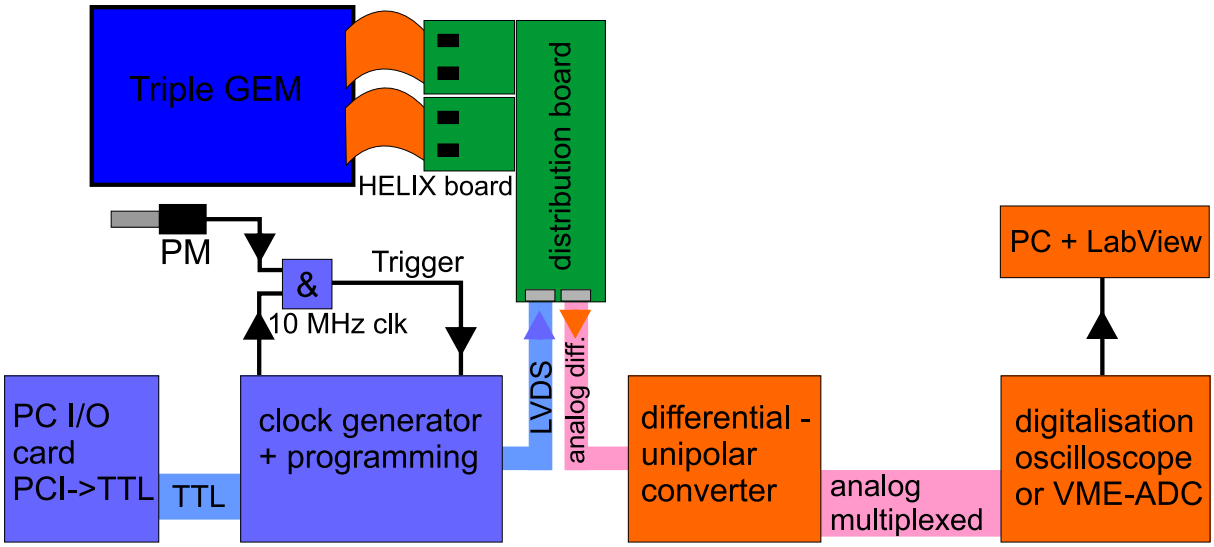

Figure 8.2: Readout scheme for the HELIX chips.

analog signal). This signal was converted by an additional board to an unipolar analog signal.

The analog signals were digitized by an oscilloscope that was connected to a PC via GPIB bus and controlled by LabView. The communication between the oscilloscope and the PC limited the readout speed to 0.5 Hz. For faster data taking the oscilloscope was replaced by VME ADC boards which provided a readout rate of up to 20 Hz.

Further information about the HELIX board and the programming procedure of the HELIX chip can be found in [41].

8.3 Noise filter

Each readout channel of the HELIX chip has a different offset on its baseline (pedestal). This can be seen in figure 8.3 (a) where the pulseheights of each readout channel for a single event are shown. To determine the pedestals a data file was recorded where the high voltage of the detector was switched off. While looping over all events from this file in an offline analysis the pulseheight of each readout channel was added up separately and divided afterwards by the number of events to derive the mean pedestal for each channel.

After subtracting the pedestals all readout channel show a common variation of the baseline (common mode noise) that was caused by electrical pick-up noise. To subtract the common mode noise from the data a high-pass filter was applied. In a first step a low-pass filter was applied on the data (see figure 8.3 b). After applying the low-pass filter the "low

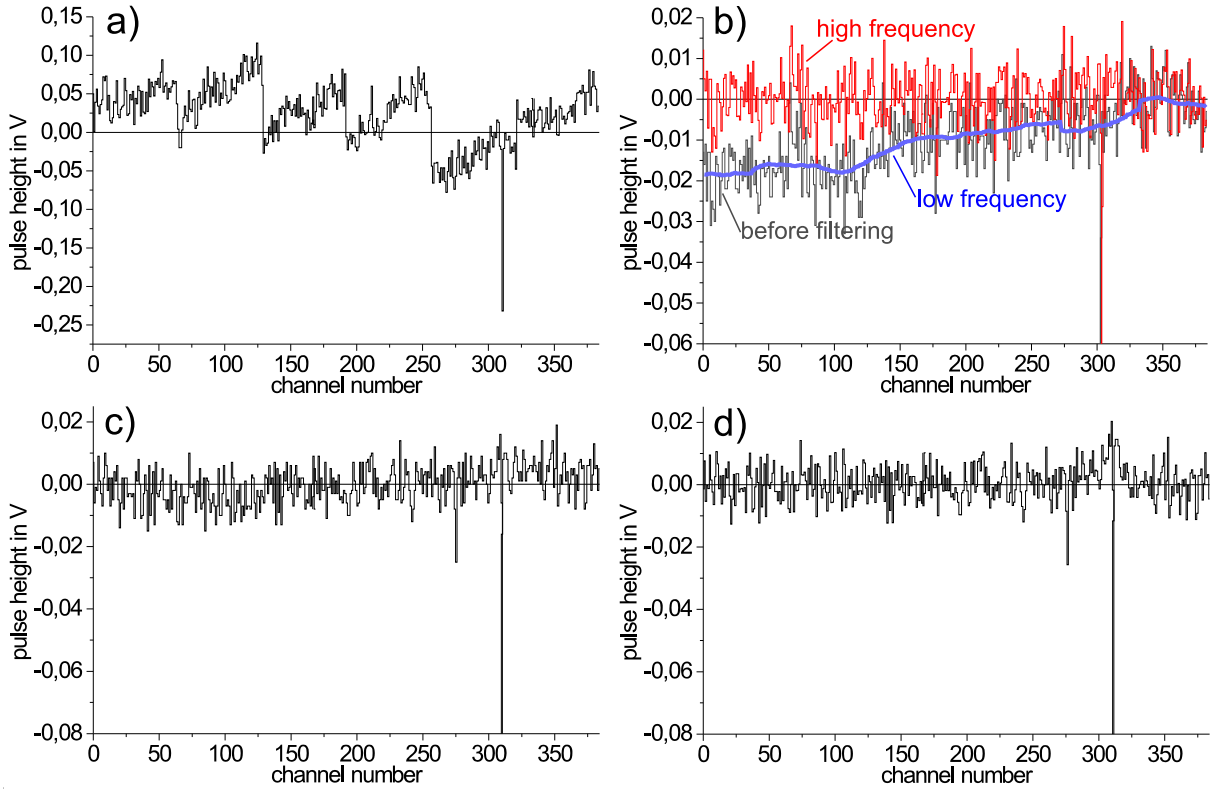

Figure 8.3: a) One event recorded with six HELIX chips before pedestal subtraction. Here only every second HELIX channel is shown as they are already sorted to upper and lower strips. b) The principle of the common mode noise filter is demonstrated. The pulseheight for each readout channel is shown for one event before filtering and after subtraction of the low frequency part. c) One event with a particle crossing the detector before and after d) common mode noise subtraction.

frequency" signal on the data remained which corresponds to the common mode noise. The low pass filtering was done by folding the data with a Gaussian mask as described in section 4.4.1.

After subtracting the common mode noise from the data "before filtering" (in figure 8.3 b) the "high frequency" part of the signal remained (using: $\text{highpass}_{(\text{signal})} = \text{signal} - \text{lowpass}_{(\text{signal})}$). The detector pulses had a typical cluster size of 2 - 3 channels which represent high frequency signals on the baseline. For this reason their pulseheight was not affected by the common mode noise subtraction. The pulse from a crossing m.i.p. can be seen in figure 8.3 before c) and after common mode noise subtraction d).

8.4 Hit finder

Clusters from the detector pulses were identified after pedestal and the common mode noise subtraction. First of all the thermal noise of each readout channel was determined. A data file was used with the high voltage of the detector switched off. The pulseheight of each readout channel was filled into a histogram. The sigma of the histograms corresponds to the noise of each readout channel (see figure 8.4 left).

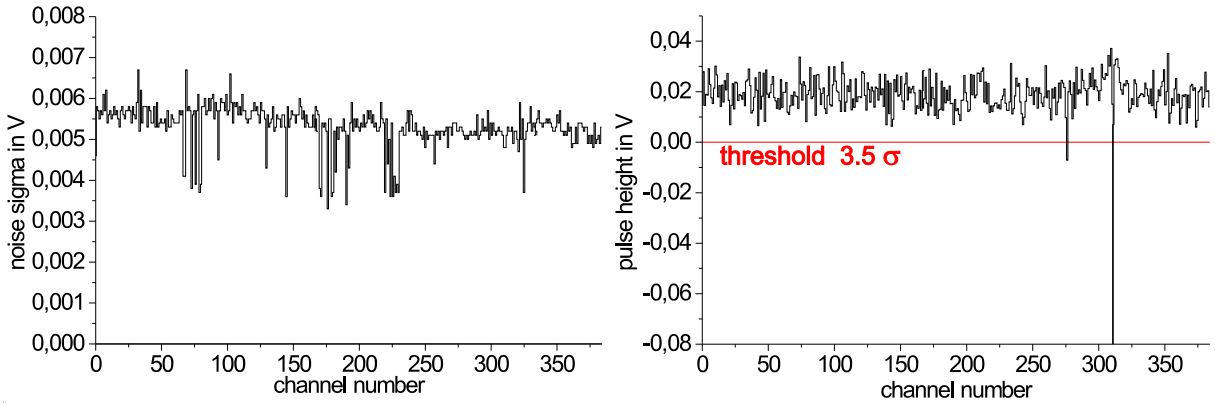

Figure 8.4: left: Noise distribution as a function of the readout channel in one layer of the third prototype. Channels with lower noise indicate broken wire bonds between the Kapton pitch adapter and the two dimensional readout board. right: The noise distribution multiplied by 3.5 and added to an event from a crossing particle. The two pulses below the threshold are identified as clusters.

A hit is accepted, if the pulseheight of a channel is below a threshold of 3.5 times the average noise. The sigma of the noise was multiplied by 3.5 and added to the signal (see figure 8.4 right). Pulses < 0 were identified as hits.

For all the clusters in the event the following properties were determined:

- number of clusters in each event
- position of the maximum peak of a cluster
- channels over threshold
- maximum pulse height
- area under the pulse
- rms of the cluster width
- mean pulse height

To demonstrate that the hits found by the method described above are correlated to particle tracks two Triple GEM detectors of the second prototype were mounted back to back as indicated in figure 9.2. With tracks from a 215 MeV π^- beam the differences of the position between the hits found in the two detectors are plotted in figure 8.5.

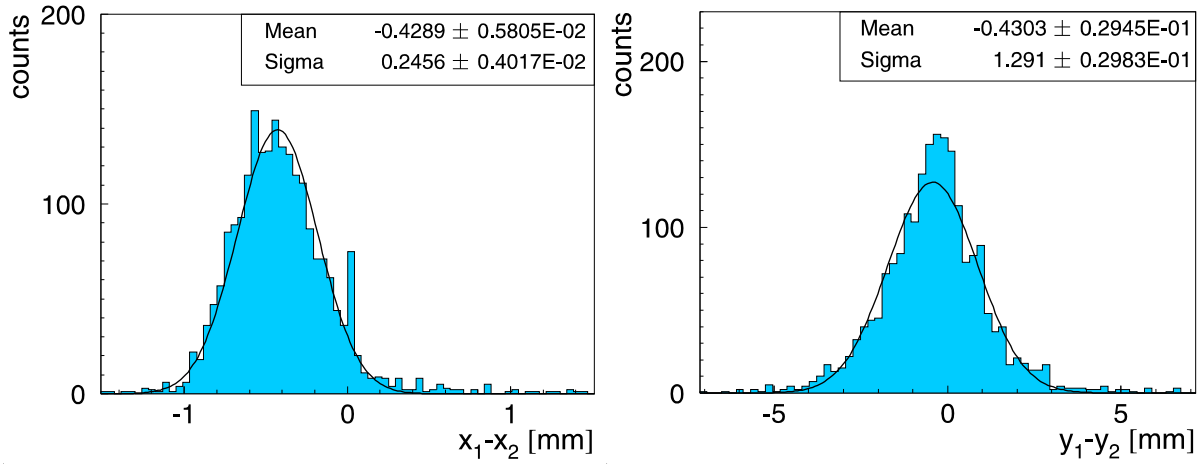

Figure 8.5: Difference between the x-coordinate (left) and the y-coordinate (right) of the hits detected in two Triple GEM detectors, measured at 370 V GEM voltage.

The sigma of the Gaussian fit had $\sigma_x \approx 0.25$ mm and $\sigma_y \approx 1.3$ mm, demonstrating that the hits are correlated to tracks from particles. The contribution of multiple scattering in the first detector was about 0.1 mm to these values, whereas the angular divergence of the beam was estimated to be below 20 mrad. An upper limit of its contribution was 0.36 mm indicating, that σ_x was dominated by the beam divergence.

Chapter 9

Detector performance

The tracking performance of the detector prototypes was studied in the laboratory and in several test beams. Most of the measurements were done with the second and third prototype and are summarized in the following chapter.

9.1 Tests at the PSI

At the LHCb experiment hadron fluxes in the inner tracker region up to $10^6\,\mathrm{cm}^{-2}\mathrm{s}^{-1}$ are expected. Detectors designed for LHCb have to be tested in an adequate environment. Therefore the hadronic beam at the Scherer Institute PSI [26] was used to study the detector performance.

9.1.1 The beam at PSI

In the πM1 area at the PSI a hadronic beam was available. The beam has its maximum intensity at 300 MeV/c for positive pions and protons. A 350 MeV/c π^+-beam was used to determine the discharge probability and operation stability of the detectors. A maximal rate of $20\,\mathrm{kHz/mm}^2$ and $60\,\mathrm{kHz/mm}^2$ could be reached for positive pions and protons respectively.

At an energy of 350 MeV/c the energy loss of a proton is five times higher than for a m.i.p. (see figure 9.1). To separate pions from protons an aluminum plate was inserted before the last dipole magnet of the beam transfer line. In this aluminum plate the protons lose more energy than the pions and after passing the last dipole magnet they were deflected to a region outside of the active detector area.

To determine the tracking performance of the detectors only a low beam intensity was necessary. Here a 215 MeV/c π^--beam was used with a intensity of $60\,\mathrm{Hz/mm}^2$. Figure 9.2 (left) shows a triple GEM prototype mounted in the PSI beam area.

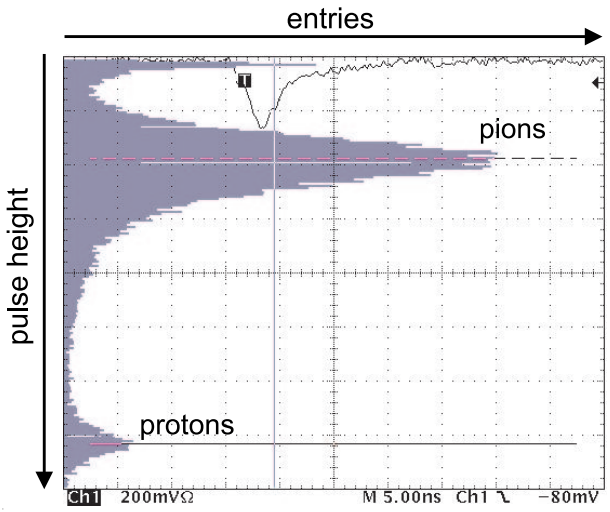

Figure 9.1: Pulse height spectrum from a scintillator. The pion and proton peaks are clearly visible. A 3 mm aluminum plate was inserted into the beam line to obtain this spectrum. With a 6 mm aluminum plate the protons were almost completely removed.

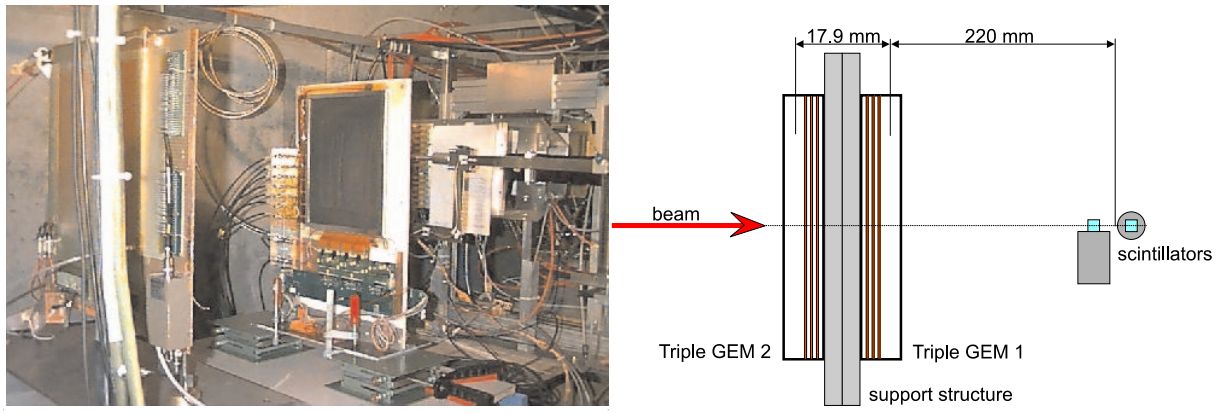

Figure 9.2: left: Setup at PSI in the πM1 area in December 1999. Four other groups tested their detectors simultaneously (CERN GDD group double GEM [42], University Lausanne and CEA/Saclay Micromegas [43], University Santiago de Compostela Microwire [44]). right: Schematic drawing of the Triple GEM detector arrangement (second prototype) and the scintillators.

9.1.2 Beam monitoring

Beam intensities and distributions were measured by a pair of $5\times5\,\mathrm{mm}^2$ scintillators mounted on a remotely movable table. A typical beam profile obtained from the PSI beam is shown in figure 9.3. The coincidence of the two scintillators provided also a trigger for the readout electronics of the chamber under test. The sensitive areas of the scintillators

were aligned to a maximal overlap. The percentage of the overlap was determined by the difference between the single counting rate and the coincidence rate of the scintillators. With a third $10 \times 10\,\mathrm{cm}^2$ scintillator the efficiency of the small scintillators was measured to be close to 100%.

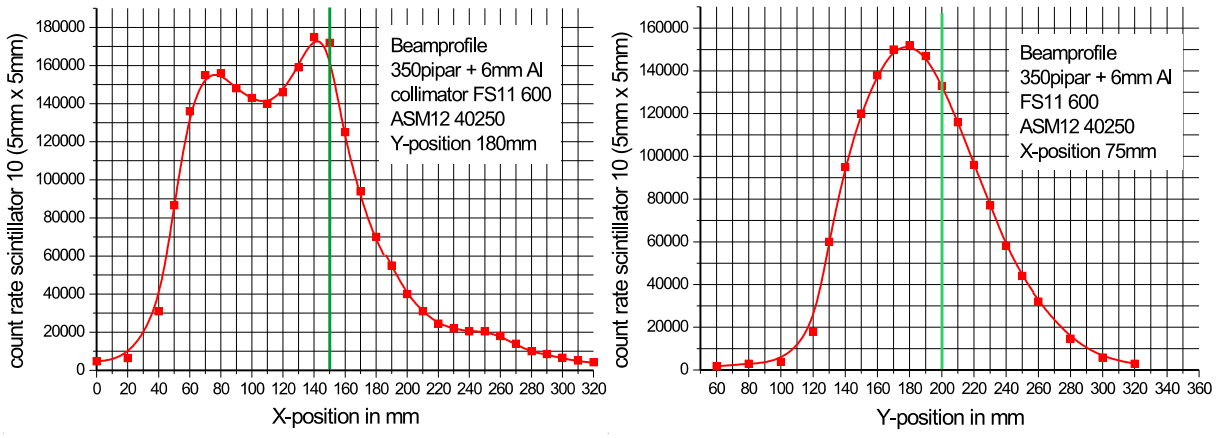

Figure 9.3: Beam profiles measured with a $5 \times 5\,\mathrm{mm}^2$ scintillator at maximum intensity (π^+ energie 350 Mev/c). A 6 mm aluminum plate was inserted into the beam line to separate protons from pions.

9.2 Charge distribution

The charge distribution measured with the second prototype is shown in figure 9.4. The measurement was performed at the PSI using a 215 MeV/c π^- beam. Pions of this momen-

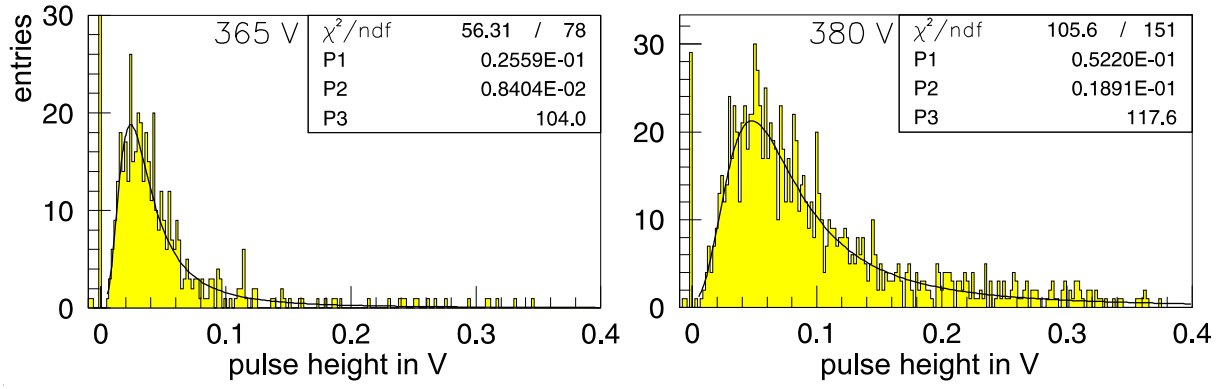

Figure 9.4: Pulse height distribution (charge of a cluster) measured at a GEM voltages of 365 V and 380 V. Events with no signal above the threshold are filled into the bin at zero.

tum are almost minimum ionizing particles. The trigger for the readout with the HELIX chip was defined by a coincidence of two scintillators.

The charge distribution can be well described by a Landau function reflecting the variations due to primary ionisation statistics.

9.3 Gain determination

In the following sections three different methods are described for estimating the gas gain using particles from a beam.

9.3.1 Gain determination from the Landau distribution

The mean of the Landau distribution is equivalent to 28 primary electrons (see chapter 2.1). With the knowledge of the HELIX chip gain the gas gain of the detector was determined (see figure 9.5).

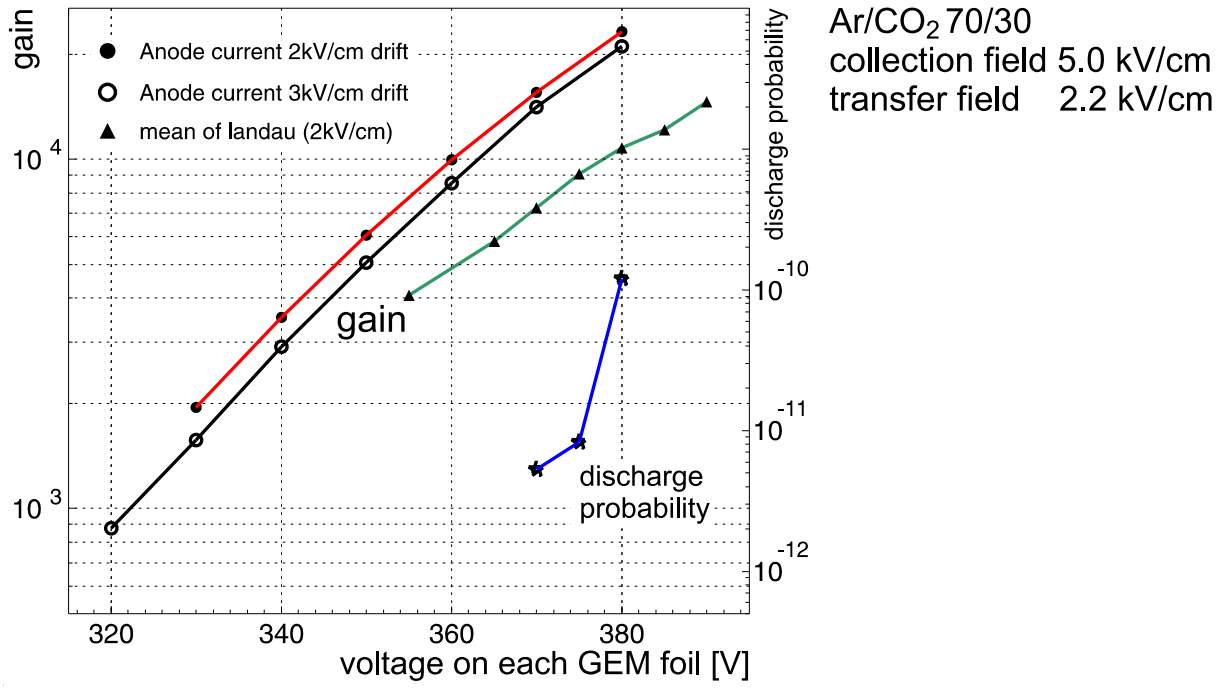

Figure 9.5: Gain determined with the second prototype from the anode currents and the mean value of the Landau distribution. Also shown the discharge probability per incident particle.

For the calibration of the HELIX gain a square wave was given to a capacitance of 1 pF which was connected to a single anode strip. In this way a defined amount of charge

was deployed on the anode strip. From the response of the HELIX chip the gain of the HELIX chip was estimated (similar procedure as the amplifier calibration described in section 5.1). The defined charge pulse was deployed within some ns to the anode. However, the charge collection time at the anode for particle pulses was about 40 ns. This leads to an underestimation of the detector gain using this method.

9.3.2 Gain determination using the beam profile

The current from the primary ionization process in the drift gap was calculated. The the total particle flux was derived by integrating the beam profiles obtained from a scan with small scintillators. Taking into account the average number of primary electrons (28 electrons for 3 mm Ar/CO_2) and $e = 1.6 \cdot 10^{-19}$ C the current $I_{primary}$ from the primary electrons was calculated.

The effective gain is defined by the anode current divided by $I_{primary}$ (see figure 9.5). This method of determining the detector gain depends crucial on the exact calculation of the total particle flux.

The detector gain derived from the Landau distribution was about a factor of two below the gain estimated with the help of total particle flux. This difference can be explained by the uncertainties in both methods.

9.3.3 Gain from the measured ionization current

The uncertainties in the estimation of the primary ionization current can be reduced by measuring the ionization current directly. The GEM side which was facing to the drift electrode was connected to ground via a current meter. After applying the drift voltage the ionization current was measured. A gain curve obtained with this method is shown in figure 9.6.

Because of a too large protection resistor in front of the last GEM foil, a significant voltage drop at high gains occurred. For this reason the curve obtained from the anode current taken at a high beam intensity saturated below the curves obtained with the ^{55}Fe calibration.

A typical number for the ionization current at a drift field of 3.0 kV/cm was 1.65 ± 0.05 nA. At a GEM voltage of 370 V an anode current of 3.78 μA was measured, resulting in a gas gain of 2850.

9.4 Efficiency plateau

To determine high voltage settings for an efficient particle detection a plateau curve was recorded. In the data a hit was identified when the pulseheight of one HELIX readout

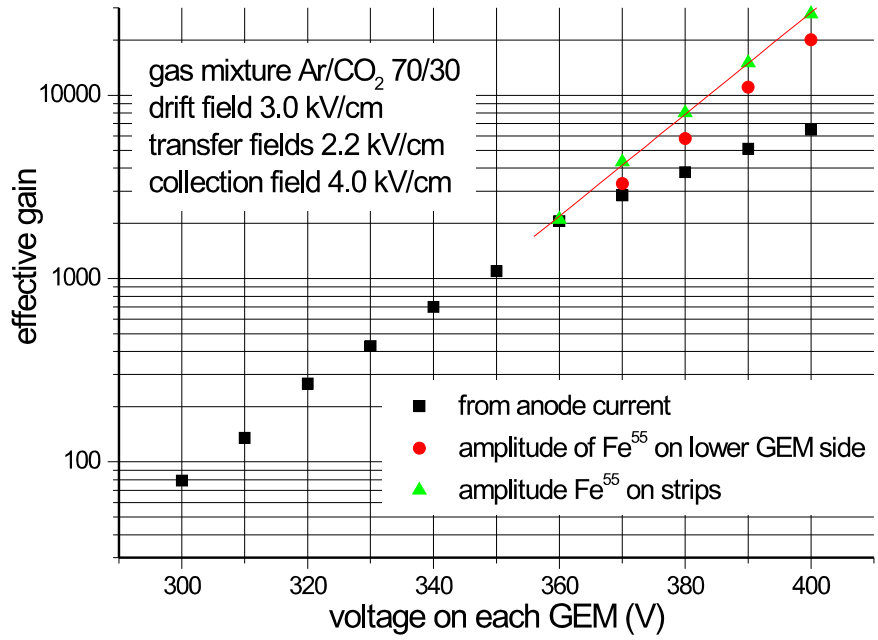

Figure 9.6: Gain curves obtained with three different methods (third prototype). Gain calculated from the ionization and anode current (squares). Gain obtained using a ^{55}Fe source. Here the pulses were taken from the anode strips (triangles) and from the lower GEM side (circles).

channel exceeded 3.5 times the average noise level. The efficiency as function of the GEM voltage is shown in figure 9.7.

For the second prototype the efficiency plateau was reached at a GEM voltage of 375 V. This corresponds to a gas gain of about 15'000. This large gas gain was necessary due to the high noise level caused by the large strip capacitance of about 100 pF.

9.5 Cluster size

The pulse width in space or the cluster size was studied as a function of the gas gain. In figure 9.8 (left) two different methods of determining the pulse width are compared. An often used definition uses the number of channels in the cluster, which have a signal larger than the noise threshold. This quantity clearly depends on the pulse height and as expected the average values rise with the gas gain.

A more physical definition of the cluster size uses the σ of a Gaussian fit to each pulse. Figure 9.8 shows, that this cluster size does in fact not depend on the gain of the detector. The value of 0.8 strip pitches (240 μm) is consistent with an estimation, which is based only on the transverse diffusion ($D_t \approx 300\,\mu m/\sqrt{cm}$) of the charged cloud along an average drift length of 4.5 mm.

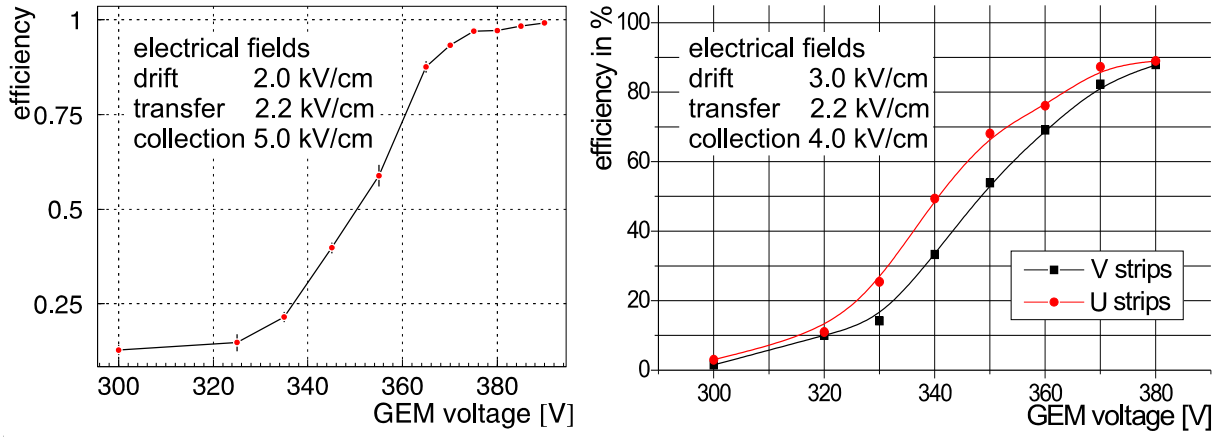

Figure 9.7: left: Efficiency as a function of the GEM voltage for the second prototype in one layer of the two dimensional readout board. right: Plateaucurve for the third prototype. Only about 300 events were used for the efficiency calculation.

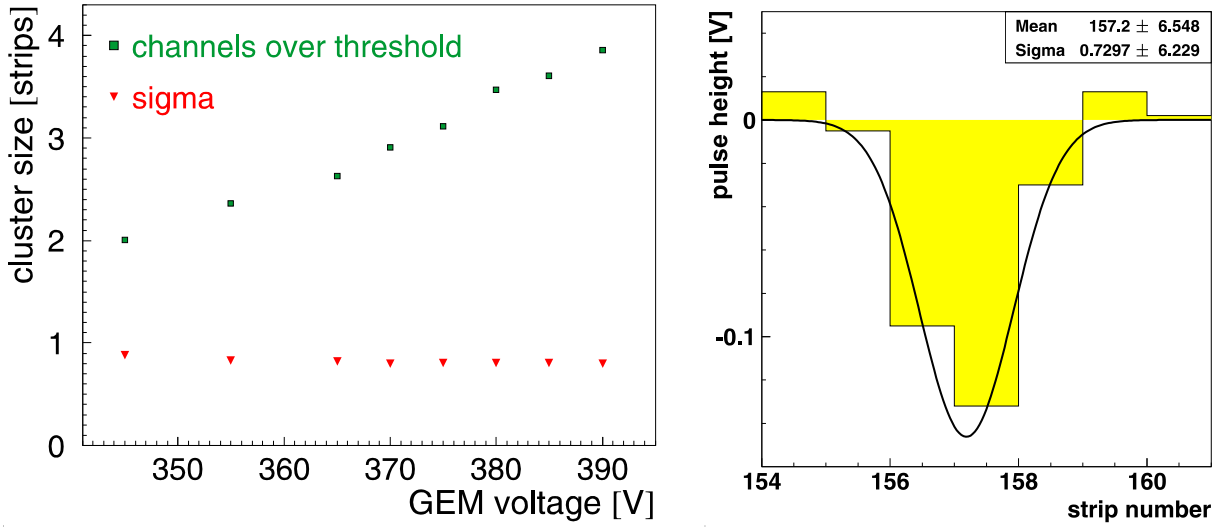

Figure 9.8: left: Cluster width as a function of detector gain, determined from the number of channels above the 3.5 sigma noise threshold (open squares) and from the width of a Gaussian fit to the pulse shape (triangles). right: Pulseheight on each anode strip for a m.i.p. together with a Gaussian fit to determine the cluster width.

In addition the cluster size (using the σ from the Gaussian fit) is correlated with the pulse height. A substantial electronic crosstalk between adjacent readout strips would manifest itself in an increasing width for larger pulses. Figure 9.9 indicates, that the pulsewidth is independent from the pulseheight.

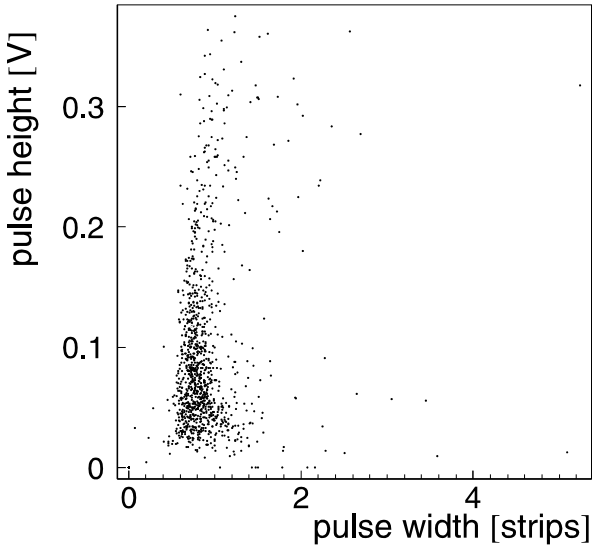

Figure 9.9: Correlation between pulse width and height. To determine the width of the signal a Gaussian fit was used.

9.6 Cosmic ray data

The limited readout speed of 0.5 Hz and the short beam time at the PSI made only runs with a low statistic possible. In the laboratory data with high statistic were taken using a cosmic ray setup.

9.6.1 Cosmic ray setup

Two identical detectors of the second prototype were mounted horizontally back to back. The trigger for the HELIX chip readout was given by a pair of $10\times10\,\mathrm{cm}^2$ scintillators below and above the detectors. To study the shape of clusters obtained from transversal tracks the detectors were operated at a higher gain than usually ($V_{GEM} = 390\,V$, gain 25'000).

Figure 9.10 shows the reconstructed hits of all recorded cosmic ray data. To cover a larger area of the detector the scintillators were moved gradually in y-direction. The distinct region with no hits corresponds to a disconnected GEM segment. Hot channels (masked off) or broken anodes are clearly recognized as lines without hits.

9.6.2 Track inclination

In the LHCb Inner Tracker the distribution of the inclination angle of the dominating background particles (mainly electrons and positrons) is expected to be very broad. It is

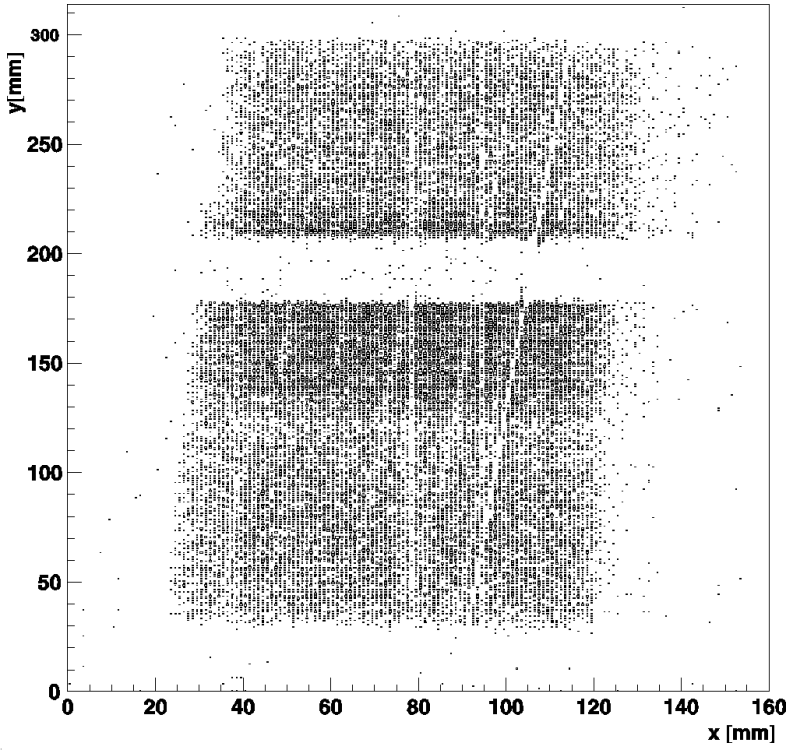

Figure 9.10: Hit map of recorded cosmic ray data in x and y direction. Broken strips are clearly visible.

therefore interesting to investigate the signal dependence on the polar angle of the incident particle.

From the hit position in the two detectors the inclination angle of the incoming cosmic particle was reconstructed, and the pulse shape was studied as a function of this angle. Figure 9.11 (left) shows the correlation between the cluster width and the inclination angle of the track. A calculation of the cluster width is shown in figure 9.11 (right), assuming an extension of the charge distribution in the drift gap of $\Delta x = \tan(\text{track angle}) \cdot d_{\text{driftgap}}$.

Figure 9.12 shows the signal of a cosmic ray event observed under an angle of about 45° compared with a vertical incidenting track. The signal height varies according to the primary ionisation statistics. Due to the smaller number of clusters for each cell the variation is much bigger than for a normal signal. This leads to the difficulty that from the signal alone it is impossible to decide whether the event originates from a single, inclined track or from several vertical particles. In a high rate application additional tracking information from other devices would be needed to analyze the data.

In principle it would be thinkable, that this feature could be used to suppress the low angle background already on the chamber level by cutting on the cluster width. In figure 9.13 the efficiency for tracks as a function of the inclination angle for different cuts on the

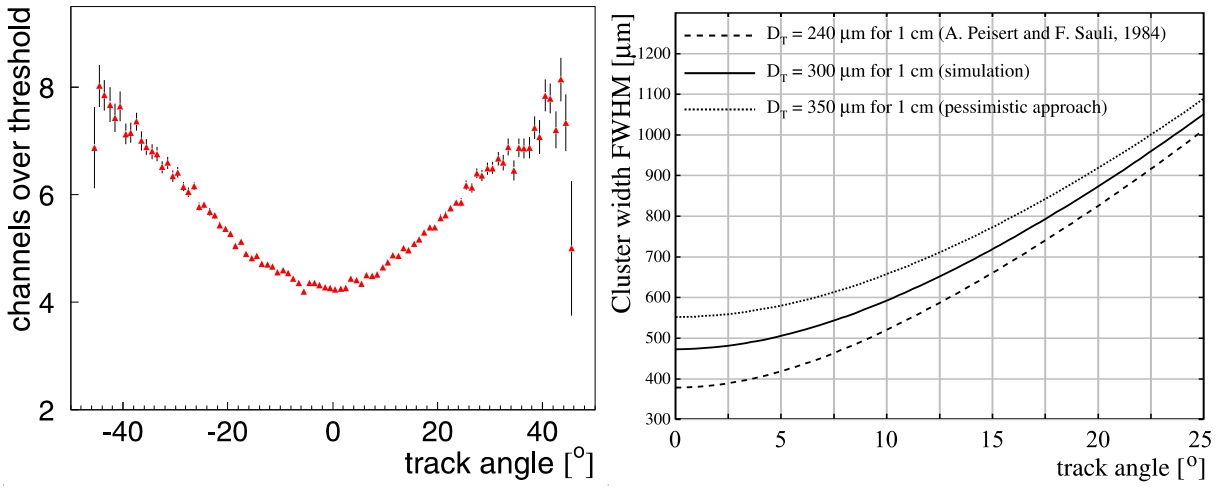

Figure 9.11: left: Cluster width as function of the inclination angle obtained with cosmic ray data (pitch of the readout board 300 μm). right: Calculation of the cluster width for three different transversal diffusion coefficients [11].

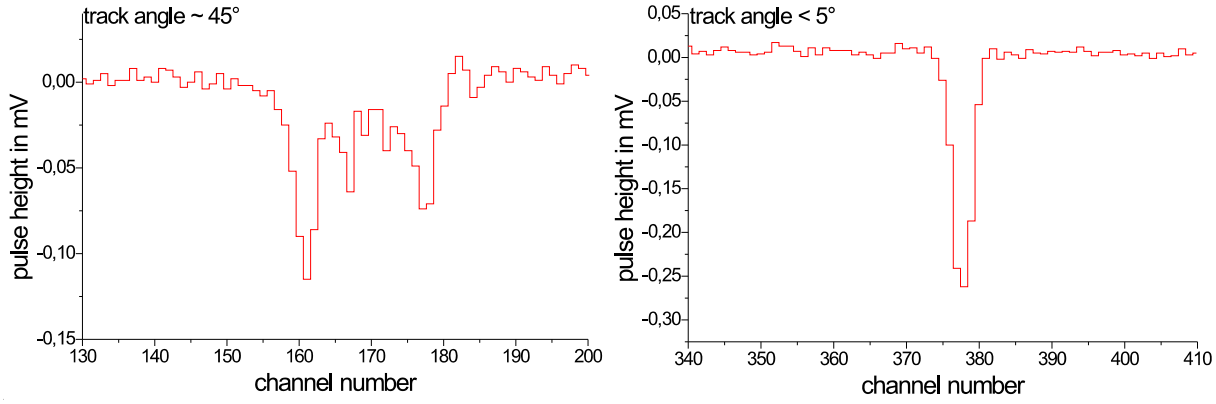

Figure 9.12: The signal shape as a function of strip position for a single cosmic ray event with an inclination angle of about 45° (left). For comparison the figure on the right shows a signal from a vertically incidenting track.

cluster width shows, that this method in principle works. By choosing a threshold of 7 the efficiency for tracks with an angle larger than 30° is reduced by a factor of three without loosing too much efficiency at the nominal inclination angle of 0°.

This feature depends critical on the cut value. Even small instabilities in the signal size of the detector would have big effects on the background acceptance or even on the efficiency of the nominal tracks.

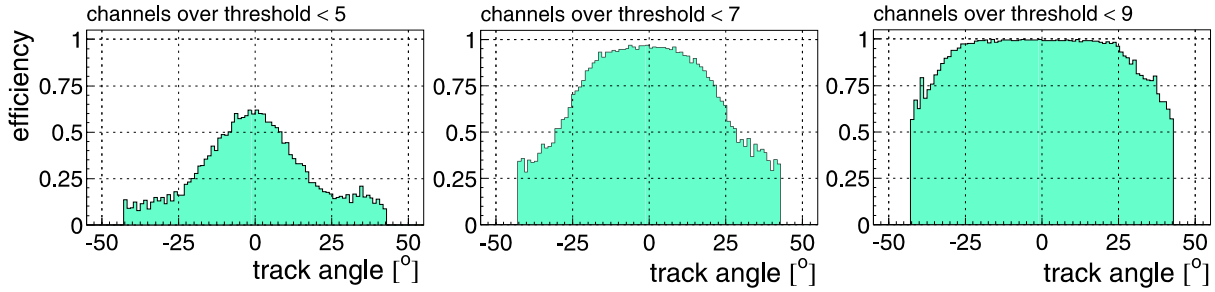

Figure 9.13: Efficiency for tracks as a function of the inclination angle for different cuts on the channels over threshold.

9.7 Tracking data from a 9 GeV π^- beam

An attempt was made to take some high energy track data at T7 beam line of the SPS accelerator at CERN using a 9 GeV π^- beam. Four double-sided silicon strip detectors provided by the HERA-B vertex detector group [45] served as a beam telescope. The complete read out chain of the HERA-B vertex detector was used, both for the beam telescope and for the Triple GEM detector.

To integrate the HELIX readout boards on the Triple GEM detector (originally intended for the HERA-B Inner Tracker) into the readout chain of the HERA-B vertex detectors an adapter board was designed. The test beam was performed together with the LHCb Inner Tracker silicon group [46]. A picture and a schematic drawing of the testbeam setup can be seen in figure 9.14.

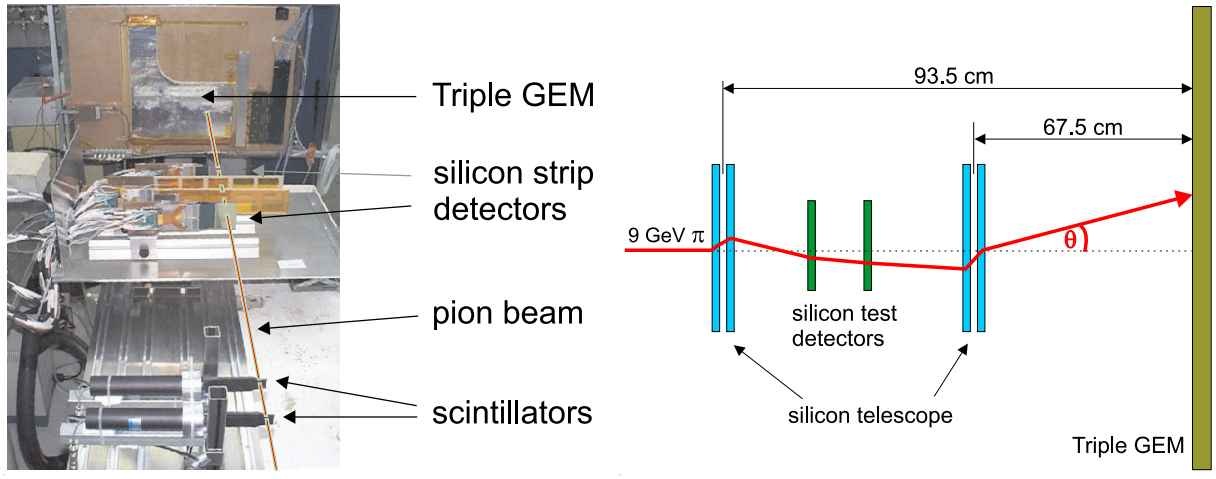

Figure 9.14: Foto and schematic drawing of the testbeam setup at CERN.

With the silicon telescope straight tracks were reconstructed and the impact point on the

Triple GEM detector was calculated. The difference between the measured track position and the predicted position from the silicon telescope is shown in figure 9.15. The width of the residual distributions times the strip pitch of 400 μm amounts to (x) 170 μm (straight anode strips) and (y) 220 μm (0.1 rad strips).

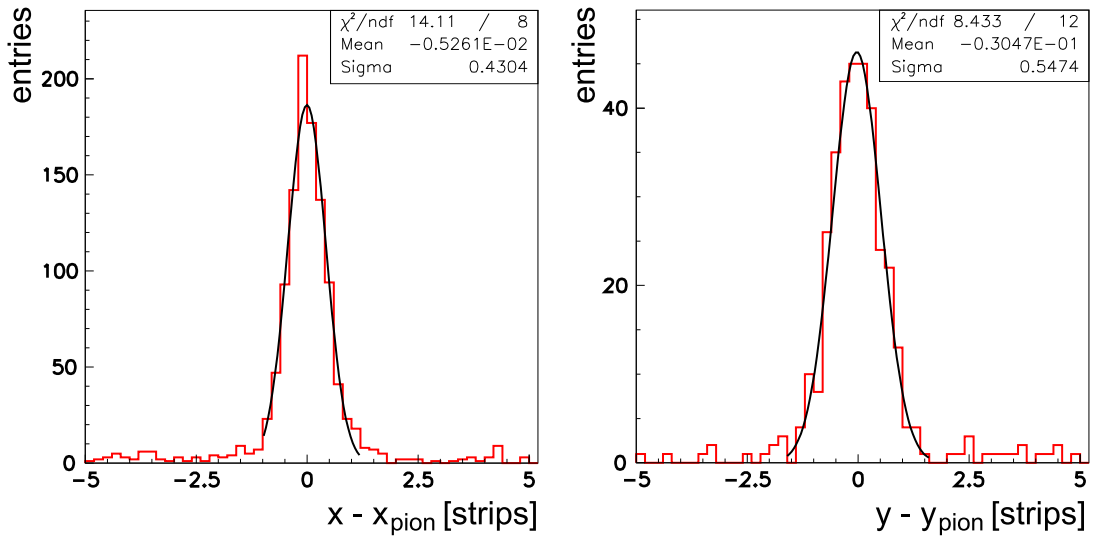

Figure 9.15: Difference between the measured and predicted track position. For the top strips a sigma of 0.43 and for the bottom strips (0.1 rad =5.71°) a sigma of 0.55 strips was obtained.

A charged particle traversing a medium is deflected by many small angle scatters. Most of the deflection is due to Coulomb scattering from nuclei. The scattering distribution is roughly Gaussian for small deflection angels. The angular distribution is given by

$$\Theta_0 = \frac{13.6\,\mathrm{MeV}}{\beta \mathrm{cp}}\, \mathrm{z}\sqrt{\mathrm{x}/\mathrm{X}_0}\ [1 + 0.038\ \ln(\mathrm{x}/\mathrm{X}_0)]\,. \tag{9.1}$$

Here p, βc, and z are the momentum velocity, and charge number of the incident particle, and x/X_0 the thickness of the scattering medium in radiation lengths [9].

The spatial resolution obtained in front of the Triple GEM detector was smeared out by multiple scattering in the six silicon sensors of the telescope. A radiation length of 9.36 cm for silicon and a thickness of $6 \times 300\,\mu$m results in a total radiation length of x/X_0=1.9%. Using formula 9.1 and the pion momentum of 9 GeV one obtains a scattering angle of $\Theta = 0.2$ mrad. After passing the distance between the silicon telescope and the Triple GEM detector ($\mathrm{d} \approx 0.70$ m) an uncertainty of the impact point of 140 μm is predicted.

This demonstrates that the measured residual distribution was dominated by multiple scattering. Therefore only an upper limit of 170 μm can be given. Other authors demonstrated, that a spatial resolutions of 40 μm can be reached with a Double GEM detector [18].

Chapter 10

Discharges in GEM detectors

It turned out that a general problem of all micro pattern gas detectors in a hadronic beam is the occurrence of local breakdown of the electric field, leading to dead time and pick-up noise in other electronic components. Sometimes a discharge can even destroy the detector.

10.1 Development of discharges

The process that leads to a discharge was studied most exactly in parallel plate chambers. If a free electron is created in the gap between the cathode and the anode of a parallel plate chamber, it will drift towards the anode. If the electric field is high enough, the electron will collide with gas molecules knocking off new electrons, which in turn accelerate and create what is known as an electron avalanche. Up to this point the electric field in the gap is assumed to be unaffected by the accumulations of both electrons and ions.

When the electron avalanche becomes "critical", i.e. the space charge accumulation is sufficient to distort the external field, a so called streamer begins to develop and the current rises abruptly. The electrodes will be discharged (breakdown) very fast, when the streamer reaches the electrodes. The discharge probability depends on the number of electrons n in the avalanche. This probability increases rapidly beyond a certain number n_{crit}. A number $n_{crit} = 10^8 - 10^9$ of electrons has to be created inside the diffusion radius to fulfill the breakdown condition. A detailed description on the conditions to form a streamer can be found in [48].

For a parallel plate chamber the breakdown voltage (air 760 Torr) can be predicted by the formula $V_b = 25.5d + 6.6\sqrt{d}$. Where V_b is the breakdown voltage in kV and d the gap length in cm [47].

10.2 Highly ionizing particles

For parallel plate counters, the simplest discharge model assumes that a discharge will occur whenever the total charge in an avalanche exceeds a given threshold, the Raether limit R. The total charge in an avalanche is the product of the primary charge N_p by the gain G. The discharge probability per incident particle is simply given by:

$$\mathrm{Prob}_{\,\mathrm{discharge}} = \int_{\mathrm{R/G}}^{\infty} \phi(\mathrm{q})\,\mathrm{dq}.$$

Figure 10.1 shows the measured primary charge density distributions per incident particle $\phi(\mathrm{q})$ in a Micromegas detector (which approximates to a parallel plate counter) for He and Ar with 10% isobutane mixtures. The curves through the data result from a parametrisation which was used to make predictions on the variation of the discharge probability per incident particle with the gain or equivalently with the total charge in the avalanche for a MIP. A single parameter the Raether limit, was adjusted for the comparison with the data shown in figure 10.2 to be $1.5 \cdot 10^8$. This good agreement with the data indicates that the origin of the discharges is due to highly ionizing particles (HIP). These HIP distributions cannot be the tail of the MIPs Landau distribution, these large charges can only result from secondary particles created in nuclear interactions of pions with the gas or the walls of the detector [43].

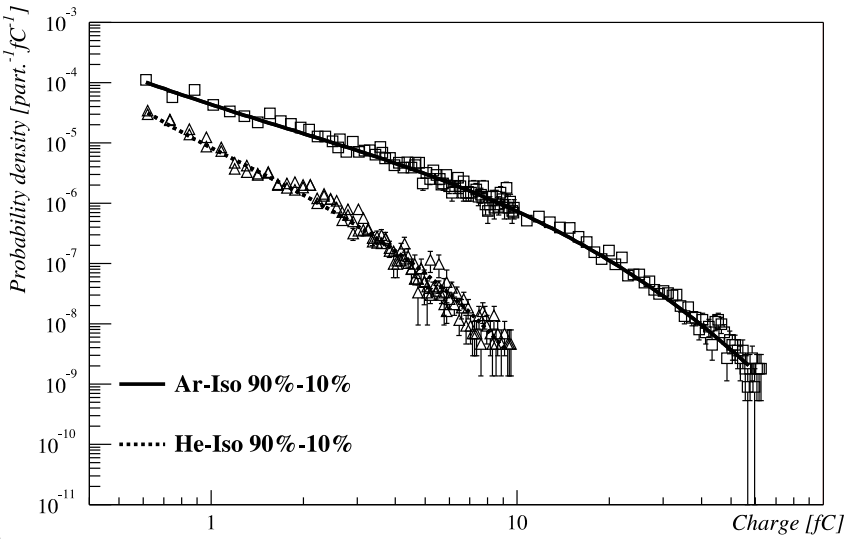

Figure 10.1: Measured probability density distributions per incident particle for the deposition of a charge between q and q + dq in the conversion gap as a function of the charge q. The data was obtained with a Micromegas detector in our PSI beam tests [43].

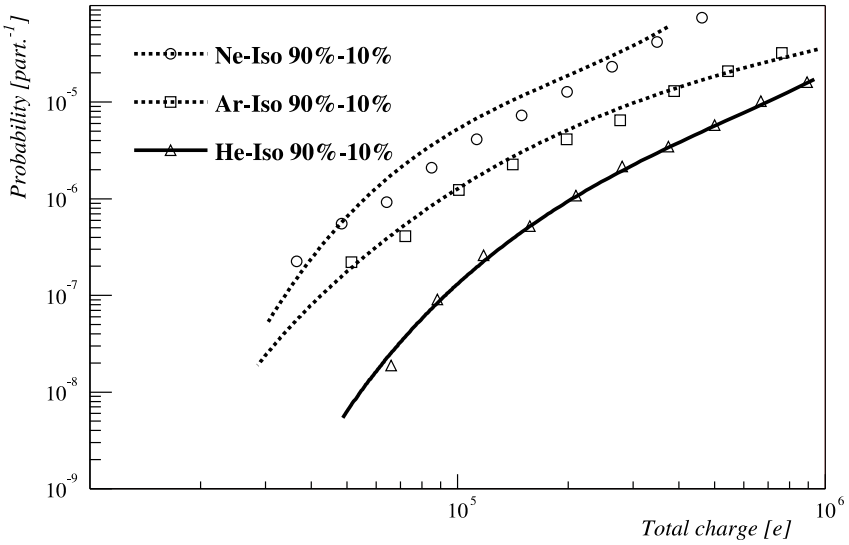

Figure 10.2: Measured discharge probability per incident pion as a function of the total charge in an avalanche induced by a MIP. The curves through the data are predictions based on a simple model on the the measurements shown in figure 10.1 [43].

For an efficient particle tracking the detector has to be sensitive to a few primary electrons and be unsusceptible to the occurrence of HIPs. This wide range of primary ionization from few electrons to several 10^6 is a general problem in all micro pattern gas detectors.

10.3 High voltage supplies

To run a Triple GEM detector seven high voltage channels were needed (2×3 GEM foils, 1 drift electrode). These voltages were provided by individual HV-supplies. The ISEG NHQ 226L [49] high voltage supplies (two channels per module) were controlled remotely by a PC running a LabView [50] software (see figure 10.3). With this HV-supplies it was also possible to read back the actual voltages and currents of the detector. In figure 10.4 (left) the voltages of the individual electrodes during the ramp up procedure are shown.

The ISEG NHQ 226L power supplies have different source impedances for supplying and sinking currents from the detector. Source currents up to 1 mA can be delivered but sink currents have to pass an internal 500 MΩ resistor which is connected to ground.

To observe the charging behaviour of the HV-supplies after a discharge in a GEM foil the potentials of the GEM sides were monitored. A 1 GΩ resistor was connected to one GEM side while the other side of the resistor was connected with a 1 MΩ active probe to an oscilloscope. In this way a 1000 : 1 ohmic voltage divider was realized.

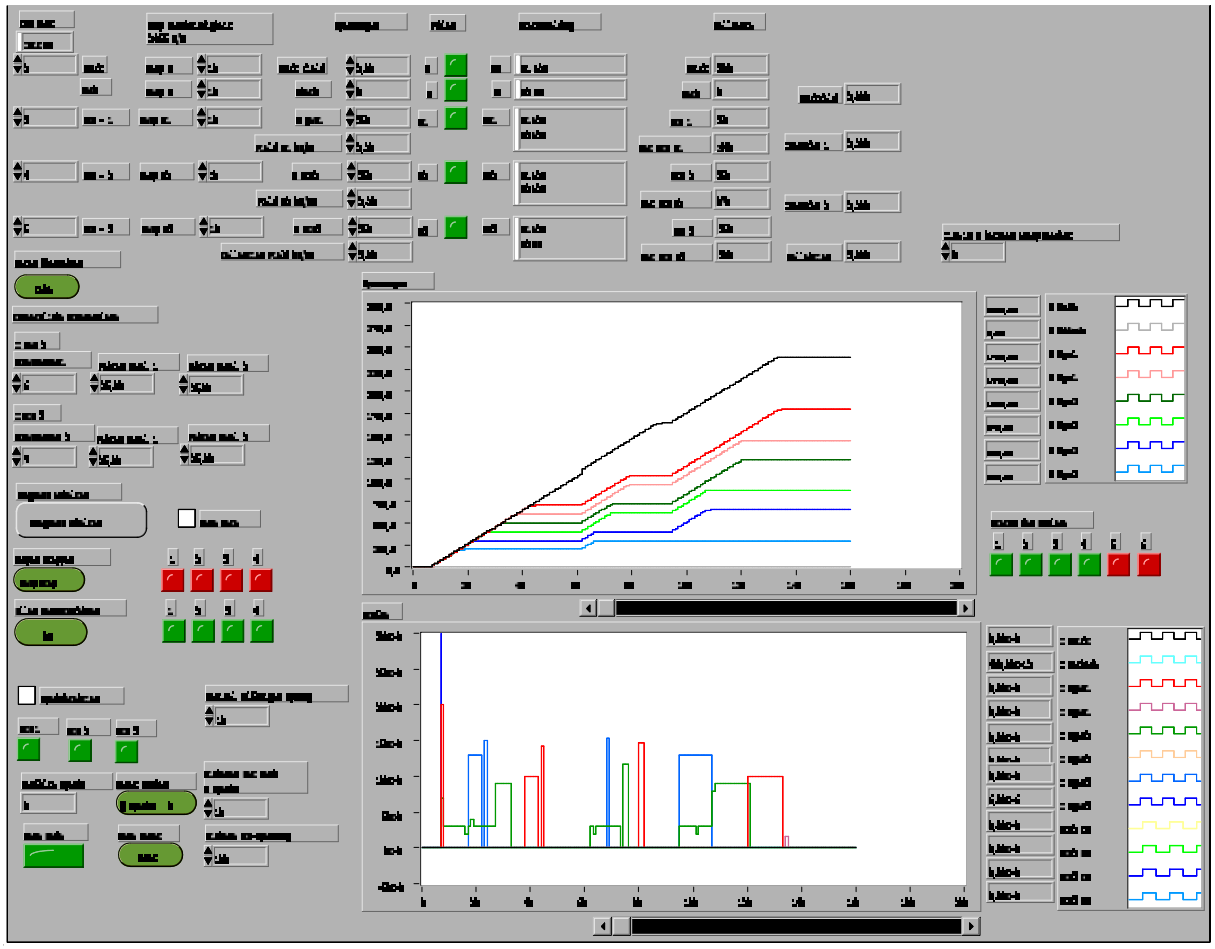

Figure 10.3: Panel of the high voltage control program. The value of the transfer fields and the GEM voltages can be entered. The program ramps all high voltage channels to the dedicated values. A discharge counter with a safety ramp down procedure was also implemented. In the two displays the actual voltages and currents are shown.

The voltage on a $10 \times 10\,\mathrm{cm}^2$ GEM foil was increased until discharging started. As this test was performed in air a GEM voltage of over 700 V was required to produce a discharge. After a discharge the capacitance of the GEM foil was almost completely discharged. This can be seen in figure 10.4 (right). The voltage difference between the top and bottom GEM side dropped to zero. To charge the GEM foil the HV-supply had to source a current to the upper GEM side and sink current from the lower GEM side. As the impedance were different for sourcing and sinking current, the voltage of the upper GEM side returned faster to the nominal voltage than the lower GEM side.

For the test beam experiment an external resistor of $10\,\mathrm{M}\Omega$ was connected directly from the output of the HV-supply to the ground to allow larger currents sinking from the GEM.

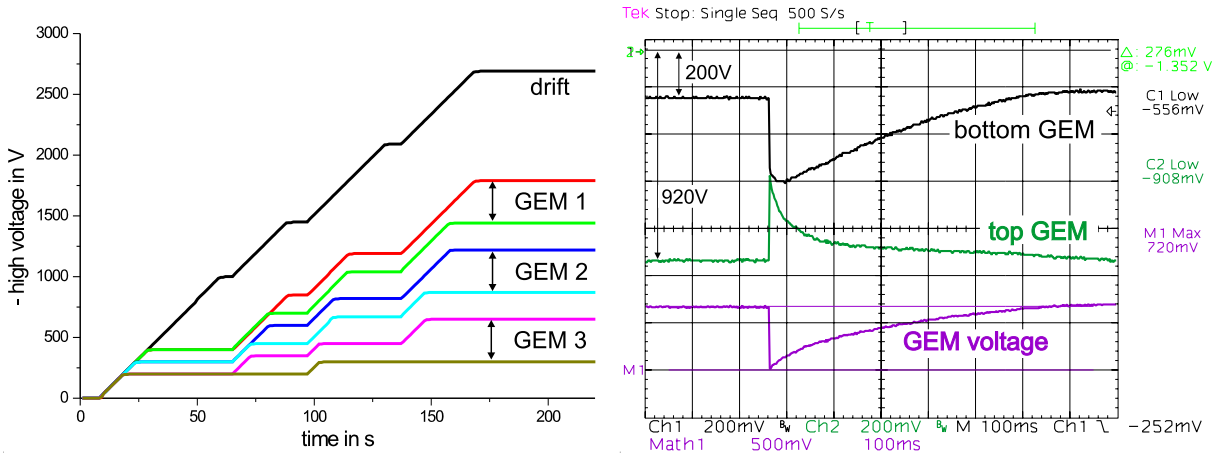

Figure 10.4: left: Ramp up procedure for a triple GEM detector. right: Charging behaviour of a GEM foil after a discharge. The arrows show the potentials of the top and bottom GEM side. Furthermore the voltage difference between the two channels (GEM voltage) is shown.

10.4 Detection of discharges

In the following section different methods are described to detect discharges. If a discharge in a GEM detector occurs, it typically takes place in one of the GEM holes. The two copper planes of the GEM foil represent a capacitance that is discharged by a spark. The simplest way to detect a discharge is to listen to the noise caused by the spark.

10.4.1 Reloading currents

A spark in a GEM foil discharges the GEM electrodes. Afterwards the power supplies will charge the GEM foil and an increased current can be measured (see figure 10.5). Depending on the current limit of the HV supply and the size of the GEM foil, this process takes between 0.1 s to 10 s.

If the detector is operated under high irradiation currents up to several μA are flowing on the GEM foils. Especially by using segmented GEM foils the reloading currents after a discharge can be too small to be distinguished from the total current induced from the irradiation. Here a different method for detecting the discharges has to be used.

10.4.2 Capacitive voltage divider

Discharges can also be detected by monitoring the voltage breakdown of the GEM electrodes. The following studies on discharges with GEM foils of $10 \times 10\,\mathrm{cm}^2$ size were performed in a gas tight aluminum box. The GEM foils were glued to frames which made it

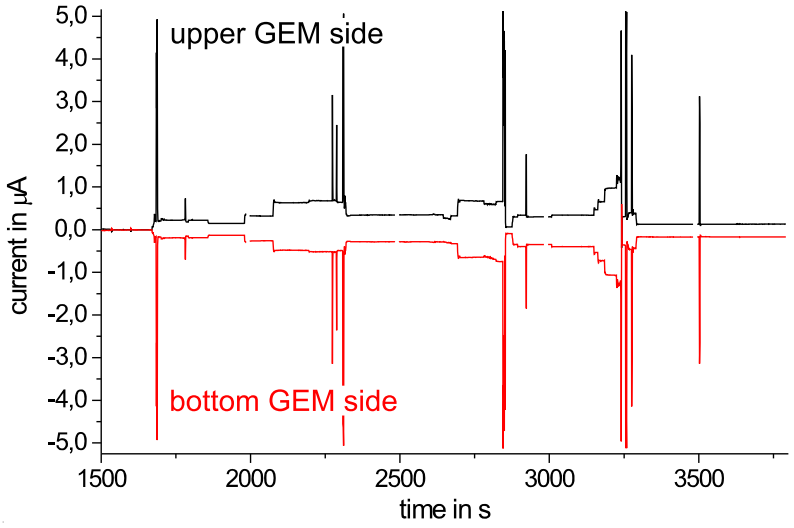

Figure 10.5: Currents on GEM foil in the first prototype (unsegmented GEM) during changes in the high voltage settings. Discharges are clearly visible by large spikes in the current.

possible to build up a Triple GEM detector by screwing three GEM foils on top of an anode structure. A picture of the aluminum box can be seen in figure 10.6 (left). Discharges were initialized either by an external α-source on top of the drift electrode (aluminized Mylar foil) or by increasing the GEM voltage until discharging started.

If a GEM voltage of 400 V was applied before a discharge, the discharge causes a jump of + 200 V (- 200 V) for the upper (lower) GEM side. This potential jumps were observed by using a capacitive voltage divider.

The capacitive voltage divider attenuates the jump and decouples the high voltage allowing to observe it with an oscilloscope. An attenuation of 100:1 was realized by connecting a capacitance of 47 pF directly to a GEM side followed by a capacitance of 4.7 nF connected to ground. In between the capacitances an oscilloscope was connected (see figure 10.6 right). The oscilloscope was internally terminated either with 1 MΩ which resulted in a time constant for the observed signals of $\tau = 4.7\,\text{pF} \times 1\,\text{M}\Omega \approx 5\,\text{ms}$ or with 50 Ω corresponding to a time constant of 250 ns (see figure 10.7).

The configuration with the long time constant showed a lower noise level allowing to detect smaller discharges (for example in segmented GEM foils). With the shorter time constant it was possible to monitor consecutive discharges in a time scale of μs.

The detection of discharges by a capacitive voltage divider has the advantage to obtain precise information on the potential drops in the detector. Furthermore it does not disturb the readout of anode signals. However the external capacitances add to the intrinsic capacitances between the GEM foils influencing the discharge size and probability as reported in [24].

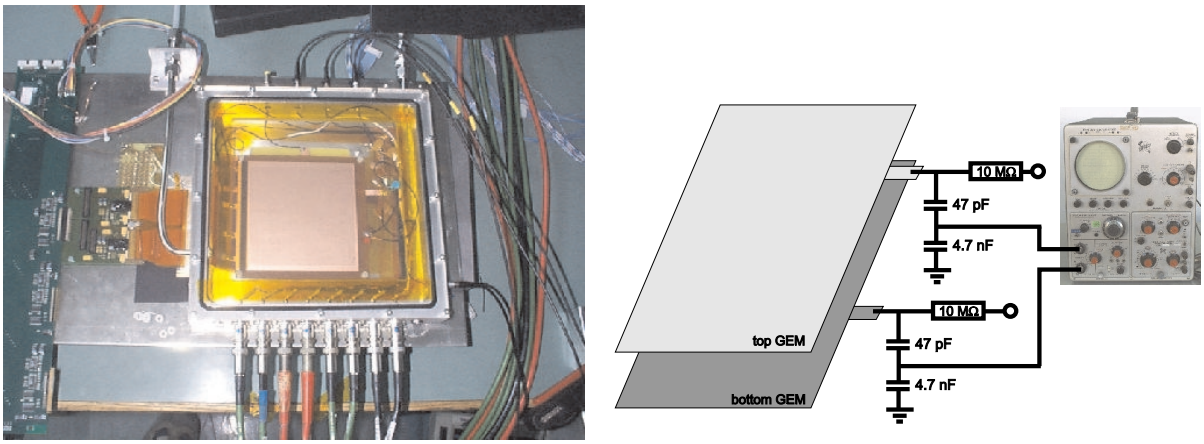

Figure 10.6: left: Gas tight aluminum box for studies on 10×10 cm GEM foils. The box was closed by a plexiglass plate. right: Schematic drawing of a capacitive voltage divider connected to a GEM foil.

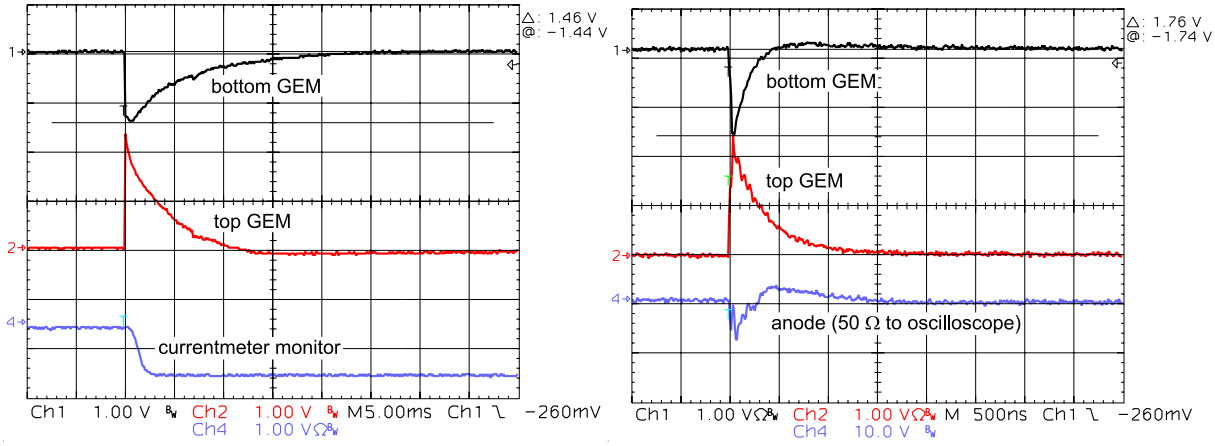

Figure 10.7: left: Discharge in a GEM foil monitored by a capacitive voltage divider. The pulseheight multiplied by 100 corresponds to the potential shift during the discharge. The oscilloscope was internally terminated with 1 MΩ (time scale 5 ms/div). Also shown the monitor output of an external current meter. A negative current of 100 nA was observed. right: Discharge in a GEM foil with the oscilloscope terminated with 50 Ω (time scale 500 ns/div). Also shown is the signal obtained from the anode with a 50 Ω termination.

10.4.3 Anode currents

For studying the discharge probability without external capacitors at the GEM foils the anode current was monitored. All anode strips were grouped and connected via a current meter to ground. Alternatively to the current meter the voltage was monitored on a external resistor from the anode to the ground. The resulting waveforms from both methods

are shown in figure 10.7. A GEM discharge releases additional electrons into the collection gap which are drifting towards the anode. An increased negative current was observed.

10.5 Propagating discharges

During a testbeam at the PSI (June 1998) with GEM-MSGC detectors for the HERA-B experiment a new phenomena was observed. After a discharge in the GEM foil an anode cathode short on the MSGC plate was observed. An inspection with a microscope showed intensive damage on the fragile structure which could not be explained by a simple anode cathode discharge. Further investigations showed that a special kind of discharge, a "propagating discharge", was responsible for this damage.

10.5.1 Detection of propagating discharges

The difference between a GEM discharge and a propagating discharge was observed with a capacitive voltage divider connected to the GEM foil. The oscilloscope was terminated with 50 Ω to observe consecutive discharges. A propagating discharge is induced by a conventional GEM discharge. This discharge is followed by a breakdown of a transfer or collection field (see figure 10.8 left). The time between the initial GEM discharge and the propagation to an adjacent electrode ranges from several 100 ns to few μs. The signal from a propagating discharge recorded with a capacitive voltage divider can be seen in figure 10.8 right.

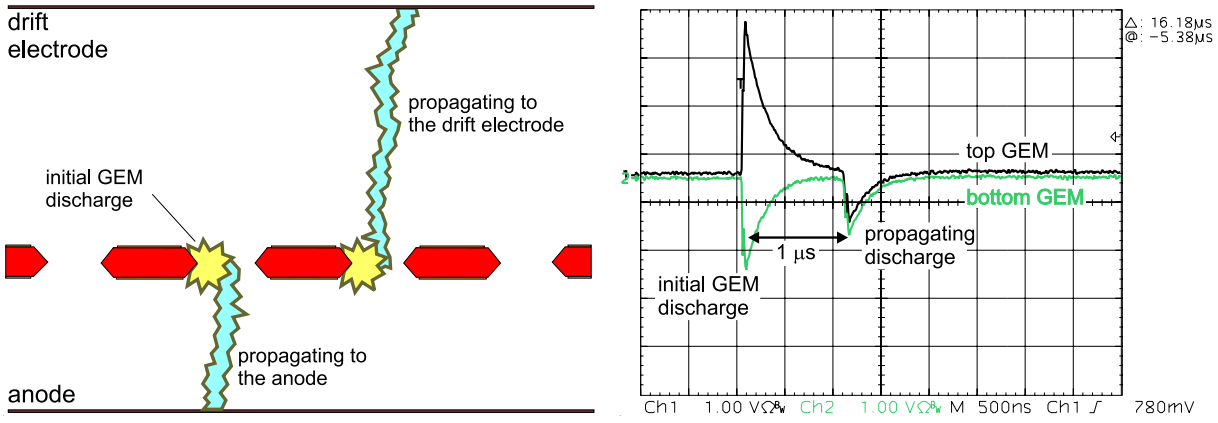

Figure 10.8: left: Schematic drawing of the sparks from a propagating discharge in a single GEM detector. right: Signal from a capacitive voltage divider. A GEM discharge is followed by a propagating discharge to the drift electrode.

Propagating discharges to the anodes were also observed with a current meter connected to the anode strips. The amount of charge reaching the anode is at least a factor of ten higher than from a conventional GEM discharge.

10.5.2 Field dependency

The mechanism which leads to the development of a propagating discharge is not understood so far. However certain parameters influence the probability that a GEM discharge is followed by a propagating discharge. A high field between the discharging GEM foil and the adjacent electrode increases the chance to produce a propagating discharge as demonstrated in figure 10.9 left.

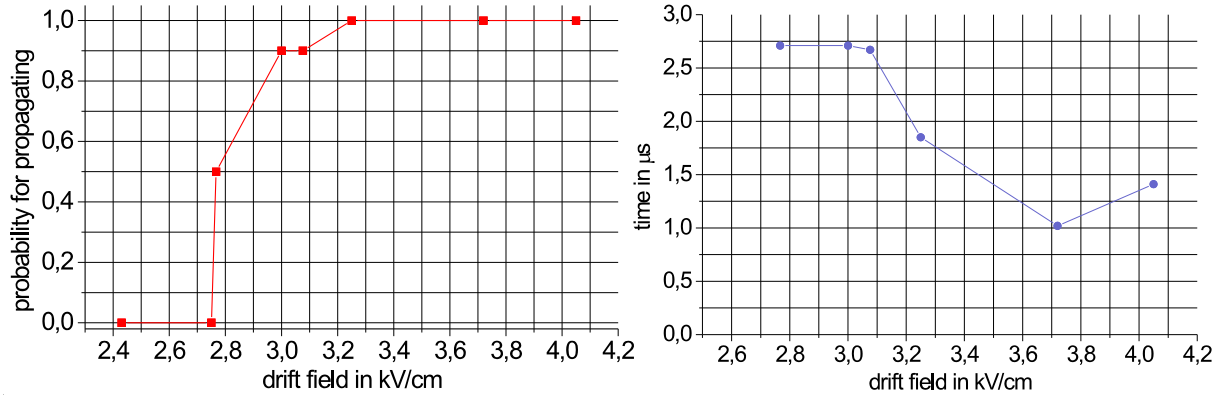

Figure 10.9: left: Probability for a GEM discharge to develop a propagating discharge to the drift electrode as function of the drift field. right: Time between the GEM discharge and the propagating discharge as function of the drift field.

The discharges on the $10 \times 10\,\mathrm{cm}^2$ GEM foils were produced by increasing the GEM voltage until discharging started ($\sim 540\,\mathrm{V}$). This voltage was significantly higher than the voltage needed for efficient particle detection ($\sim 370\,\mathrm{V}$). This measurement was only performed to investigate the general dependency on the increased field.

The breakdown of the GEM voltage increases the field between the GEM foil and the adjacent electrodes. For a GEM voltage of 400 V the field to the adjacent electrodes will be increased by about 200 V after a GEM discharge.

10.5.3 Further observations

An explanation for the mechanism which leads to the development of the propagating discharge could be, that the released electrons originating from the GEM discharge form a streamer to the neighboring electrode. The time that is needed by the electrons to drift

from the GEM foil to the anodes is in the rage of several 10 ns. This can not explain the long time between the GEM discharge and the propagation of several μs.

The drift velocity for ions in the gas is 1000 times smaller than for electrons. This drift time is too large to explain the observed time constant. However the time between the GEM discharge and the propagating discharge depends on the applied field between the GEM foil and the adjacent electrode as shown in figure 10.9 right. Most likely a combination of photon feedback and moving electrons or ions is responsible for the development of a propagating discharge.

Assuming a typical capacitance between the GEM foil and the adjacent electrode of 50 pF and a current limiting series resistor of 1 MΩ, any potential change of the GEM foil by the HV supply will have a time constant of at least 50 μs. The development of a propagating discharge between the GEM foil and the adjacent electrode takes a few μs. Therefore, the HV supply cannot be responsible for the observed effect.

The probability to evolve a propagating discharge depends strongly on the energy released by the initial GEM discharge. The discharge energy can be reduced by segmenting the GEM foil. A detailed study on this subject can be found in [24].

10.5.4 Electronic protection

The most dangerous case is a propagating discharge from the last GEM foil to the anodes. The readout structure needed for GEM detectors are more robust than a MSGC plate and damages after propagating discharges were not observed. However the connected readout electronics needs a protection to avoid failures.

The HELIX chip had standard CMOS protection diodes at the input pads. Furthermore the anodes were connected to the HELIX by a ceramic pitch adapter which had integrated 600 Ω protection resistors (see chapter 8.1). This was originally intended to prevent the HELIX chip from anode cathode discharges on the MSGC plate.

During the tests performed with different prototypes of Triple GEM detectors a large number of GEM discharges and propagating discharges occurred. It was never observed that a readout channel was lost. Sometimes the readout chip had to be restarted after a discharge. It turned out that the protection resistors provide a good protection on the cost of a increased noise level.

10.6 GEM shorts

The two copper planes of a GEM foil are separated by a 50 μm Kapton foil. With the GEM voltage applied the observed current between the copper planes is of the order of some nA. A permanent short between the two copper sides may remain after a GEM discharge. If this occurs with an unsegmented GEM foil the complete detector is not operational anymore.

10.6.1 Lifetime of GEM foils

By looking at a GEM foil while a discharge occurs a lightning in a small spot can be seen by eye. The electrical energy stored in a GEM foil is released on a small spot. Kapton or remaining dust on the GEM foil can be burned and a permanent short remains. Several of the tested detector prototypes suffered from such a short. This indicates that a GEM foil survives only a certain number of discharges, between a few and several thousands.

Discharges in GEM foils appear either due to defects on the GEM foil or under radiation in a particle beam. If the GEM discharges due to a defect (dust or fabrication failure) the discharge occurs always at the same place. Then the development of a GEM short is likely. Discharges resulting from breakdown induced by highly ionizing particles are spread over a larger region of the GEM foil and the chance to produce a permanent short is decreased.

10.6.2 Conditioning of GEM foils

When the detector was switched on for the first time the high voltage was steadily increased over some hours until the full operation voltage was reached. With this procedure higher operation voltages could be obtained than by increasing the voltage within some minutes. The origin of this effect is not understood so far, it is possible that polarization in the Kapton of the GEM foils is responsible for this.

If the detector will be operated in an intensive hadronic beam the GEM foils have to be "trained" first. Under full irradiation the high voltage was increased during one day until the operation voltage was reached. For most of the tested detectors the discharge probability was decreasing with the time the detector was operated in the beam.

10.6.3 Removing GEM shorts

GEM foils that suffered from a short could often be recovered by applying a high current flowing through the GEM foil. If the short was a low ohmic resistor the current through the GEM foil was limited by the protection resistor which then had to be removed. By

increasing the voltage on the GEM some shorts disappeared (like a burned fuse) and some remained constant or turned to a lower resistor.

10.6.4 Segmented GEM foils

After a permanent GEM short the complete detector is damaged. Therefore the second prototype had a ten-fold segmentation of one GEM side. All segments were of the same size. Then in the case of a GEM short only one tenth of the detector is lost. The segmentation was realized by etching a groove into the copper of one layer of the GEM foil (see figure 10.10).

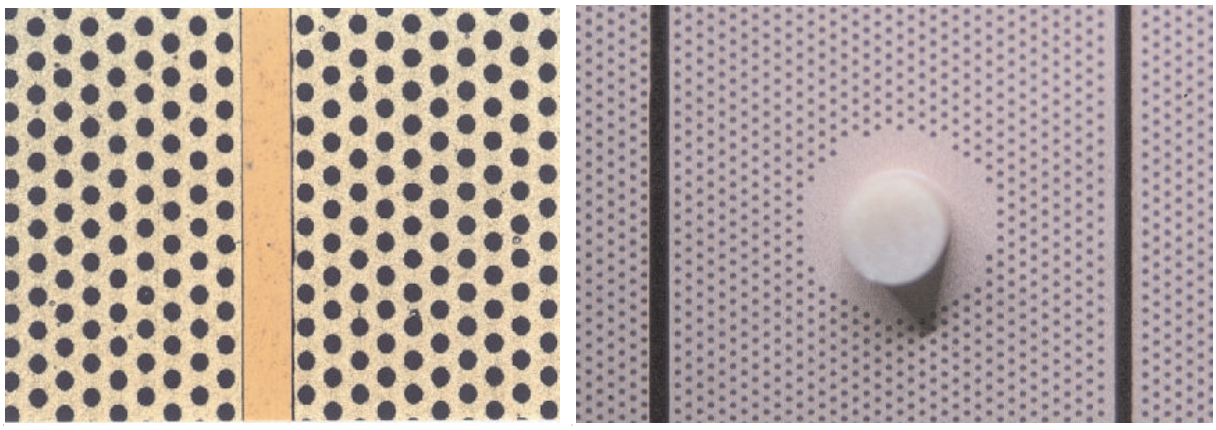

Figure 10.10: left: Removed copper on a 200 μm wide gap between segments on the second prototype. right: Segments of the third prototype where the width of one segment was 5 mm. Also a spacer on a copper spot can be seen.

A further advantage of the segmentation of the GEM foil is the reduced energy released in a discharge. For this reason a segmented GEM withstands more discharges. The segmentation of the GEM foil does not affect the discharge probability under hadronic irradiation (see chapter 10.8).

10.7 Fine segmented GEM foil

After the promising experience obtained with the ten-fold segmentation of the second prototype, an additional small $10 \times 10\,\mathrm{cm}^2$ triple GEM detector was built where the segment width of the GEM foils was reduced to 1 mm. It was expected that the charge stored in one segment is now too small to produce a streamer which can discharge the complete segment. Pictures of a fine segmented GEM foil are shown in figure 10.11.

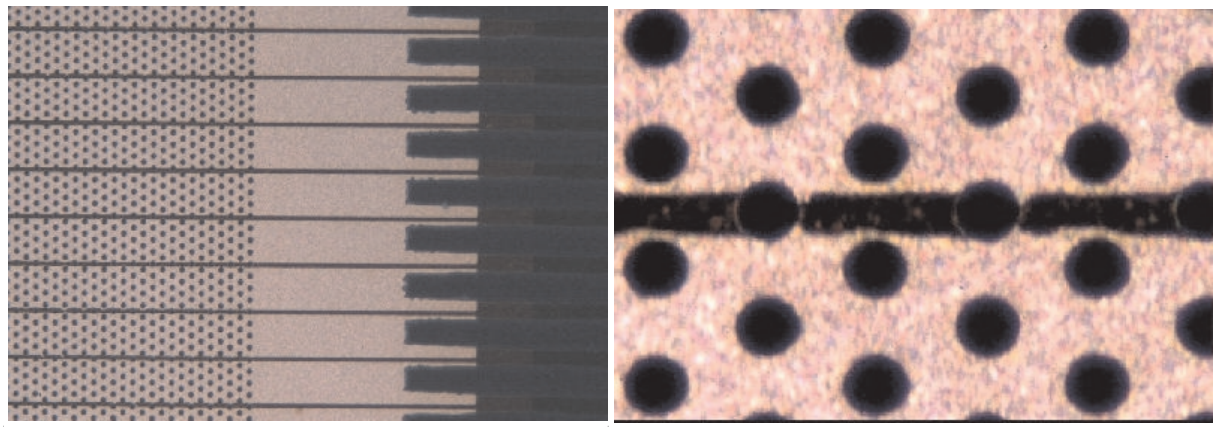

Figure 10.11: left: Foto of a fine segmented GEM foil. The protection resistors for the segments can be seen as black bars. right: Close up of the segment border. Remaining copper edges around the GEM holes from the etching of the segment borders can be seen.

The production of the GEM foils started from a standard unsegmented $10 \times 10\,\mathrm{cm}^2$ GEM foil. Narrow traces were etched into one side of the copper surface of the GEM foil. Unfortunately the segment borders cross the GEM holes as shown in figure 10.11. In contrast to the GEM foil of the second prototype place for the the segment borders had been reserved on the etching mask in order to avoid GEM holes on the segment borders.

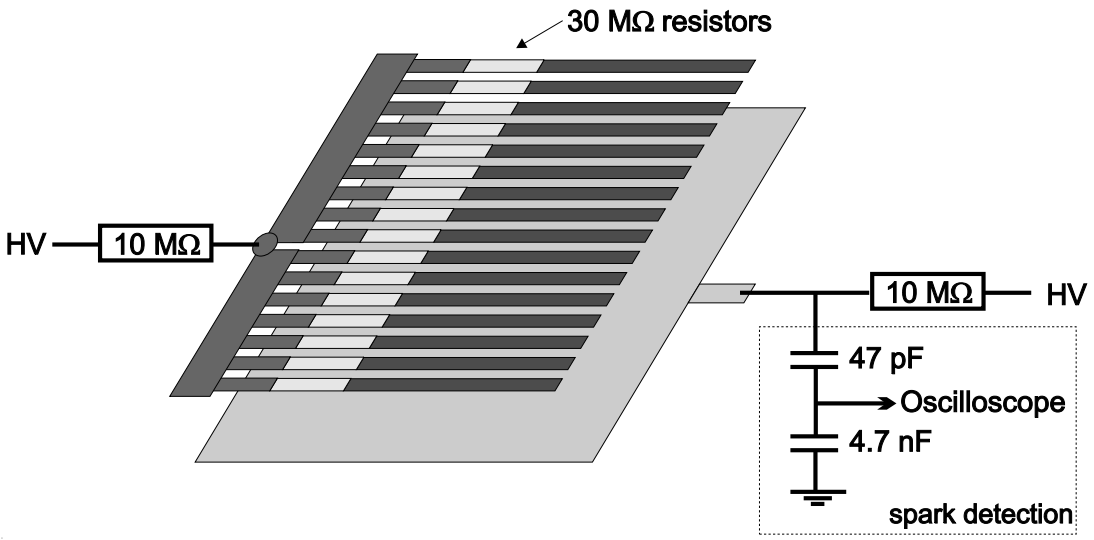

Figure 10.12: High voltage scheme together with a capacitive voltage divider for the detection of discharges (spark detection).

Every segment was equipped with an individual resistor of $30\,\mathrm{M}\Omega$. This resistor was

printed in a lithographic way on the GEM foil. The high voltage scheme together with the spark detection is shown in figure 10.12.

10.7.1 Discharge size

When a discharge in one GEM segment occurs the potential difference between the two GEM sides will drop from 500 V to 0 V. The capacitive coupling to the other segments tries to retain the potential of the unsegmented side. The discharged segment shows a potential drop of 500 V. The unsegmented side will show a voltage drop of 500 V / 100 = 5 V. A capacitive voltage divider (100:1) connected to this GEM side shows a 50 mV pulse.

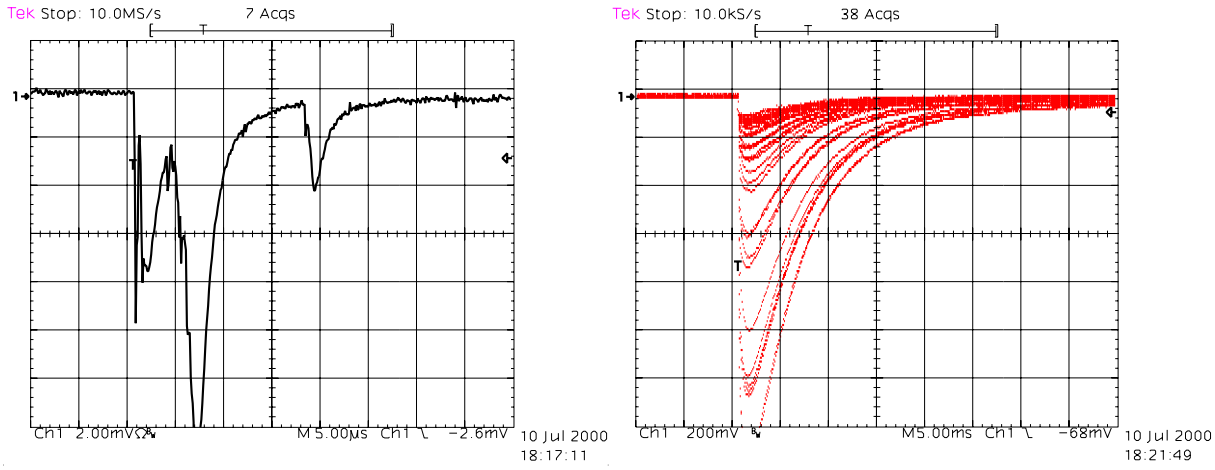

Figure 10.13: left: Signal obtained from a single discharge on a segmented GEM foil (1 mm segments) with a short integration time (5 μs/div, 2 mV/div). Several successive pulses are visible. right: Discharge with a longer integration time (5 ms/div, 200 mV/div). The response of several discharges was added up with the oscilloscope.

A typical discharge pulse in a fine segmented GEM foil can be seen in figure 10.13 (left). It consists of several small successive pulses from discharges. To determine the percentage of segments which have discharged the oscilloscope was terminated with 1 MΩ. The total voltage drop after all small discharges can be determined. Discharging all segments corresponds to a voltage drop of 2.5 V. Here pulse heights over 1 V were observed (see figure 10.13 right) indicating that a major part of the segments were discharged. Apparently after a discharge of one segment the adjacent segments discharged as well. In fact, when looking on a GEM foil while a discharge occurred small sparks between the segment borders could be observed. We have to conclude that the segment borders were too narrow to prevent the neighboring segment from discharging.

To test the stability of a fine segmented GEM foil, i.e. counting the number of discharges before the GEM foil shows a permanent short, the GEM voltage was increased to 550 V, where continuous discharging started. The capacitive voltage divider was connected to a scaler that counted the discharges. After 10 hours and about 150000 discharges still no short occurred.

10.7.2 Segment borders

After applying the operation voltage on a Triple GEM detector which consisted of fine segmented GEM foils, currents in the lower two GEM foils were visible. With an amplifier also small pulses at the anode were observed. After turning around the first GEM foil such that the unsegmented side was facing to the drift electrode the currents and the pulses disappeared almost completely.

It turned out that the currents originated from the segment borders where sharp copper edges remained from the etching close to the GEM holes (see figure 10.11). Close to the copper edges an increased electrical field exists that leads to the emission of electrons. These electrons were amplified by the three GEM foils and caused the observed currents.

Sharp edges close to the GEM holes have to be avoided. For this reason a small copper spacing between the segment borders and the GEM holes as shown in figure 10.10 is essential.

10.8 Operation stability

For an implementation of Triple GEM detectors in the LHCb Inner Tracker it is important that the detector can run for several years without major failures.

As described earlier all three different Triple GEM prototypes were tested in an intensive hadron beam at the PSI. Here the discharge probability was determined and the general performance in a intensive particle beam was studied.

For the determination of the discharge probability per incident particle, the total particle flux passing the detector had to be estimated (see chapter 9.1.2). The discharge probability was calculated using $p_{\text{discharge}} = \frac{\text{discharge rate}}{\text{particle rate}}$. The obtained discharge probability is shown in figure 10.14. The operation stability of the three prototypes can be summarized as follows:

First prototype: Two identically built detectors were operated in the PSI beam (April 1999). With the first detector signals from pions were recorded at a gain of 70'000 in a low intensity beam. A discharge rate of the order of 10 per hour could be observed. During two weeks of running time a total number of about 150 discharges were

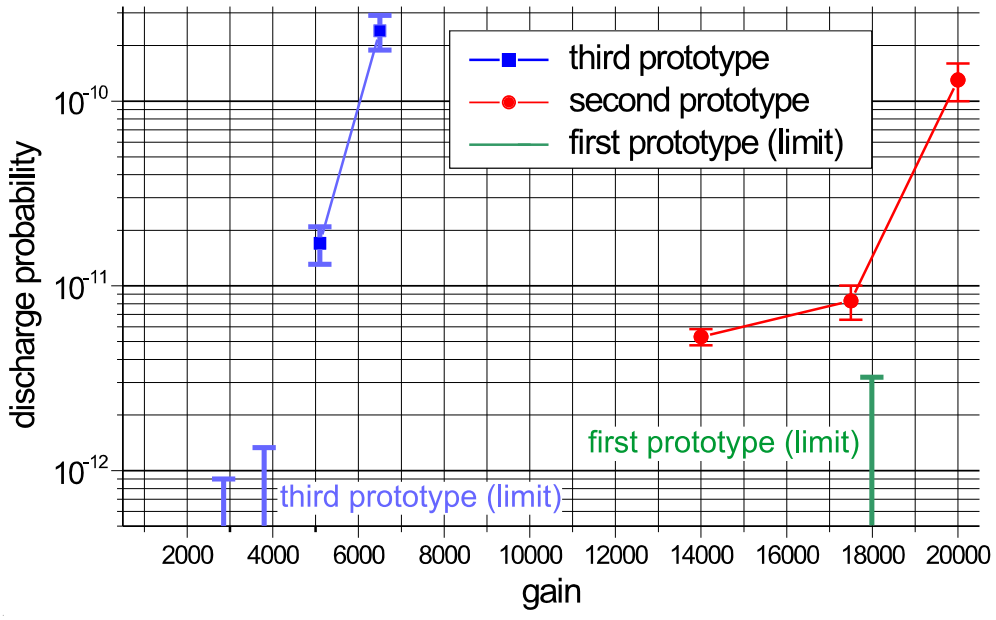

Figure 10.14: Discharge probability vs. detector gain for all three different Triple GEM prototype. If during a run no discharge was detected a limit for this gain was calculated.

accumulated. Unfortunately one discharge caused in one of the GEM foils a 10 MΩ short, causing permanent damage.

After 2 minutes of proton irradiation the second detector developed an electrical short (gas multiplication factor set to only 1000). This short could be removed by applying high electrical currents. This repaired detector was carefully conditioned by increasing the gain from 200 to 23'000 over a one day period during irradiation using high rate proton beam. This improved the stability significantly. The detector now survived an 8 hour run with a gain of 18'000 at a proton rate of 40 kHz/mm^2 without a single GEM discharge.

Second prototype: The GEM foils had a ten fold segmentation. One of the two detectors had the GEM segments facing to the drift electrode (see figure 6.9) and the other detector the segments facing towards the readout board. During a test beam at the PSI (December 1999) no significant difference (e.g. in sparking probability) between the two detectors was observed.

One of the detectors had a drift electrode which consisted of a thin 25 μm copper clad Kapton foil that was not stretched very well. An interruption in the gas flow lead to a contact between the drift electrode and the upper GEM side. This GEM foil developed shorts in 3 segments, where two shorts could be removed. After disconnecting the segment with the short from the high voltage the detector showed no change in the operation performance in the PSI beam.

Third prototype: Two detectors of the third prototype were assembled in Lausanne and one in Novosibirsk. The major problem was to ensure the flatness of the stretched GEM foils because the L-shape of the detector was mechanically not as stable as a rectangular shape. Because of this problem the first detector from Lausanne was not able to keep transfer fields above 2.0 kV/cm.

The flatness during manufacturing was improved for the second detector where the honeycomb plate for the drift electrode was fixed on a pumping table during the manufacturing process. This detector was able to keep transfer fields up to 5.0 kV/cm.

In a test beam at PSI (June 2001) at gains above 2500 discharging started while irradiation with the maximal pion rate achievable from the PSI beam. A possible explanation for the early occurrence of discharges is, that an accidental cut in one of the GEM foils during manufacturing caused this early breakdown. The detector that was glued in Novosibirsk was operated stable at high gains. After a defect in the PSI accelerator where several hours strong rate fluctuations occurred this detector showed also early discharging.

Since the GEM foils of the second and the third prototype had identical hole geometry the different discharge probabilities originates from tiny details on the construction. Unfortunately no definitive explanation of these observations can be given.

Chapter 11

Summary and conclusion

The LHCb experiment which will be built at the LHC accelerator at CERN is designed to measure CP violation in the decay of B-mesons. An important part of the LHCb experiment is the Inner Tracker which covers the innermost part around the beampipe where a particle flux up to 2×10^4 $mm^{-2}s^{-1}$ is expected. One possible solution for the detector technology is a micro pattern gas detector. Within the scope of this work several prototypes of a Triple GEM detector were built and tested under different conditions.

The first Triple GEM prototype consisted of GEM foils which were originally intended for the HERA-B experiment. All gaps between the electrodes of the detector were 3 mm. A printed circuit board with parallel anode strips was used as readout board. The detector was tested in a intensive hadronic beam at the PSI. At a gas gain of 18'000 a discharge rate below $3 \cdot 10^{-12}$ per incident particle was observed.

For the accurate investigation of the signal shape an amplifier with a short shaping time was developed. The formation of the anode signal for photon signals was understood and explained by the drift of the electron cloud from the last GEM foil towards the anode strips. For minimum ionizing particles the clustering of the primary ionisation charge has been observed. The time resolution for particles crossing the detector was measured to be 8 ns.

A second prototype was built with a sensitive area of 30 cm $\times$ 23 cm which included several further developments. The size of the transfer gaps was reduced from 3 mm to 1 mm which made spacers on the GEM foils necessary. The spacers were realized by gluing small cylinders on small copper spots on the GEM foil. To avoid the fail of a complete detector after an electrical short in a GEM foil, the GEM foils of the second prototype had a ten fold segmentation. A further testbeam at the PSI showed that these new features did not influence the discharge probability. Furthermore a two dimensional readout board was designed which allowed to combine zero and five degree readout strips within one detector. This readout board worked in principle but the capacitance of the 30 cm long anode strips of 100 pF induced large noise in the amplifiers.

A "zig-zag" geometry on the readout board was implemented to reduce this large anode capacitance for the third prototype. For 20 cm long anode strips the capacity was reduced below 20 pF (bottom strips 0.73 pF/cm; top strips 0.54 pF/cm). The outer shape of the third prototype was a L-shape which was the result of an optimization of the detector acceptance to cover the innermost area around the LHC beampipe. The active area was 45.0 cm $\times$ 41.5 cm. The GEM foils had a 100 fold segmentation. During a testbeam at the PSI the low discharge probability of the first and the second prototype could not be reproduced. The reason for this was not understood, but it is possible that defects of the GEM foil and glue accidentally dropped on the GEM foil caused early breakdowns.

Studies on the tracking performance of the detectors were done with the HELIX 128 chip. For the readout of the HELIX chip a data acquisition system was set up which included the off-detector electronics and the offline analysis software.

The observed cluster size was comparable with expectation from the transverse diffusion of the charge cloud. The FWHM diameter of the signal at the readout board of about 0.5 mm allows in principle very accurate position measurements with typical readout line pitches of 300 μm to 400 μm. During a testbeam at CERN an upper limit for the spatial resolution of 170 μm could be determined, where this value was dominated by multiple scattering in the beam telescope.

As a conclusion the Triple GEM detector is a very stable, robust, low X_0, fast and cheap detector for applications with intermediate size areas and very high, even hadronic particle densities, showing lowest sparking rates at very high gains compared to other technologies. Low angle tracks should be avoided. Significant safety factors for the gas gain should be used to compensate for inhomogenous signal size across the chamber. If analog readout is used a very high accuracy in track position measurement can be expected.

Bibliography

[1] T. Nakada, B Physics at LHC, Review talk given at the Fourth International conference on B physics and CP violation, Ise, Japan, February 2001.

[2] J. Christenson et al., PRL 13 (1964) 138.

[3] M. Kobayashi and K. Maskawa, Prog. Theor. Phys. 49 (1973) 652.

[4] L. Wolfenstein; PRL 51 (1983) 1945.

[5] LHCb Technical Proposal. CERN/LHCC 98-4 LHCC/P4.

[6] V. Talanov, Radiation environment at the LHCb Inner Tracker area, LHCb note 2000-013.

[7] G.F. Knoll, Radiation Detection and Measurement, John Wiley and Sons, Inc, 1979.

[8] K. Kleinknecht, Detektoren für Teilchenstrahlung, Teubner Studienbücher, 1984.

[9] Particle Data Group, Review of Particle Physics, The European Physics Journal C 15, 1-878 (2000).

[10] A. Sharma, R. Veenhof, Properties of some gas mixtures used in tracking detectors, http://consult.cern.ch/writeup/garfield/examples/gas/trans2000.html.

[11] P. Cwetanski, Untersuchungen an Detektor-Prototypen für das innere Spurkammersystem bei LHC, diploma theses, Heidelberg 1999.

[12] G. Charpak et al., Nucl. Instrum. Methods 62, 262 (1968).

[13] A. Oed, Nucl. Instrum. Methods A263, 351 (1988).

[14] M. Hildebrandt, Entwicklung und Bau der Detektoren für das Innere Spürkammersystem bei HERA-B, Dissertation, Heidelberg 1999.

[15] B. Schmidt, Nucl. Instrum. Methods A371(1998)230.

[16] F. Sauli, A. Sharma, Micro-Pattern Gaseous Detectors, CERN-EP/99-69.

[17] Fabio Sauli, The Gas Electron Multiplier (GEM), Nucl. Instrum. Methods A 386 (1997) 531-534.

[18] A. Bressan et al.,Beam tests of the Gas Electron Multiplier, CERN-EP/98-163.

[19] S. Bachmann et al., Charge Amplification and Transfer processes in the Gas Electron Multiplier, CERN-EP/99-48.

[20] Technology developed by a. Gandi and R. De Oliveira, CERN-ES-MT.

[21] Novaclad: http://www.sheldahl.com/Product/TMNovaClad.htm.

[22] M. Hoch, Development of Fast Trecking Detectors: Micro Strip Gas Chamber and GEM Gas Electron Multiplier, Technische Universitaet Wien, April 1998, Dissertation.

[23] C. Richter, Development of Micro pattern gas detectors for high rate experiments, Dissertation, Heidelberg 2000.

[24] S. Bachmann et al., Discharge studies and prevention in the Gas Electron Multiplier (GEM), CERN-EP/2000-151.

[25] VV61 amplifier, designed by the electronic engineer R. Rusnyak, Physikalisches Institut der Universität Heidelberg.

[26] Paul Scherrer Institut, CH-5232 Villigen PSI, www.psi.ch.

[27] B. Bochin at al., Signal observation from minimum ionizing particles and time resolution estimation in the Triple-GEM dtector, LHCb note 99-009 (public).

[28] Ortec amplifiers, http://www.ortec-online.com/

[29] B. R. Smith, Aging Test Analysis. CERN 1999,
http://brsmith.home.cern.ch/brsmith/AGEING/misc.html.

[30] Distributor for Epo-Tek epoxys: Polyscience AG, Postfach 5329, CH-6330 Cham.

[31] Gluing machine: Asymtek, Gesellschaft für Löttechnik mbH, D-75123 Pforzheim.

[32] D. Mörmann, Entwicklung eines hochauflösenden Spurdetektors mit zweidimensionaler Ortsbestimmung, diplom theses, Universität Karlsrude, 1999.

[33] A. Bressan et al., Two-dimensional readout in GEM detectors. Nucl. Instrum. and Meth. A425 (1999) 254.

[34] A. Bondar et al., Performanxe of the triple-GEM detector with optimized 2-D dead-out in High intensity hadron beam, sbmitted to Nucl. Instrum. Methods.

[35] Helix Manual http://wwwasic.kip.uni-heidelberg.de/∼feuersta/projects/Helix/.

[36] Beetle Reference Manual, v1.0 (LHCb 2001-046), 23.4.2001.

[37] Thin film ceramics, Siegert TFT, Hermsdorf, Thüringen Germany.

[38] Z-Bonding by Dr. U. Werthenbach, University of Siegen, Germany.

[39] ELATECH Klebstoff GmbH, Magdeburger Ring 32g, D-76344 Eggenstein-Leopoldshafen, Germany.

[40] Lattice Semiconductor Corporation, www.latticesemi.com.

[41] Wolfgang Gradel, The Readout System of the HERA-B Inner Tracker, Dissertation, University Heidelberg, 18. July 2001.

[42] S. Bachmann et al., Performance of GEM detectors in high intensity particle beams, CERN-EP/2000-116.

[43] J. P. Peroud et al., Study of sparking in Micromegas chambers, Preprint submitted to Elsevier Preprint 19. Dec 2000.

[44] B.Adeva et al, Performance of Micro Wire Detector at a PSI Test Beam, LHCb-99-021 (public).

[45] C. Bauer et al., Nucl Instruments and Methods A 418 (1998) 65-79.

[46] C. Bauer et al., Test Beam Results on Inner Tracker Silicon Prototype Sensors, LHCb Note 2001-135.

[47] G. E. Georghiou et al., Two-dimensional simulation of streamers using the FE-FCT algorithm, Appl. Phys. 33(2000)L27-L32.

[48] H. Raether, Electron avalanches and Breakdown in Gases, Butterworths Advanced Pysics Series, London 1964.

[49] ISEG Spezialelektronik GmbH, Bautzner Landstr. 45, D-01454 Rossendorf.

[50] National Instruments Corporation, www.labview.com.